Optical trapping and manipulation of chiral microspheres controlled by the photon helicity

Georgiy Tkachenko

université de BORDEAUX

THÈSE PRÉSENTÉE

POUR OBTENIR LE GRADE DE

DOCTEUR DE

L'UNIVERSITÉ DE BORDEAUX

ÉCOLE DOCTORALE DES SCIENCES PHYSIQUES DE L'INGÉNIEUR

SPÉCIALITÉ : Laser, Matière et Nanosciences

Par Georgiy TKACHENKO

OPTICAL TRAPPING AND MANIPULATION OF CHIRAL MICROSPHERES CONTROLLED BY THE PHOTON HELICITY

Sous la direction de : Etienne BRASSELET

Soutenue le 4 septembre 2014

Membres du jury :

M. POULIGNY Bernard	Centre de recherche Paul Pascal	Président
Mme GLEESON Helen	The University of Manchester	Rapporteur
M. BREVET Pierre-François	Université Claude Bernard Lyon 1	Rapporteur

Résumé en français

L'optomécanique, qui traite des effets mécaniques exercés par la lumière sur des objets matériels, est en premier lieu gouvernée par les lois de conservation telles que celles de l'impulsion, du moment angulaire et de l'énergie. Par exemple, lorsqu'un objet redirige ou absorbe la lumiére, la modification de l'impulsion du champ résultant de l'interaction lumière-matière se manifeste par l'apparition d'une force optique appliquée à cet objet, qui peut alors être déplacé. De manière analogue, un couple optique apparaît dés lors que l'interaction lumière-matière modifie le moment angulaire du champ, offrant la possibilité de mettre en rotation la matière par voie optique. De manière originale, cette thèse vise à établir la possibilité d'exploiter les degrés de liberté angulaire de la lumière afin de contrôler les degrés de liberté de translation d'un système matériel. Nous avons ainsi mis en évidence (à la fois expérimentalement et théoriquement), et exploité à des fins applicatives, le fait que le moment angulaire de spin associé à un champ lumineux peut être utilisé pour contrôler les forces optiques appliquées à un système matériel.

Pour cela, nous avons exploité une propriété fondamentale de la matière et de la lumière: la chiralité. Un système est dit chiral si son image dans un miroir n'est pas superposable à celui-ci via des translations ou rotations d'espace. Un exemple typique correspond à nos mains, droite et gauche, qui images dans un miroir mais ne sont pas superposables. En pratique, on associera à un milieu chiral droit ou gauche le paramètre χ, qui prend respectivement la valeur +1 ou −1 selon que le milieu est droit ou gauche. La lumière peut elle aussi être dotée de la propriété de chiralité. L'exemple qui nous intéresse est celui des ondes lumineuses polarisées circulairement gauche et droite, qui sont respectivement associées à une structuration spatiale en hélice gauche et droite du champ électrique à laquelle on réfère grâce au paramètre Λ, qui vaut respectivement +1 ou −1. Ce paramètre est appelé hélicité et trouve son origine dans la description corpusculaire de la lumière. En effet, Λ correspond (en unités de $\hbar$, la constante de Planck réduite) à la projection du moment angulaire du photon sur la direction associée à son impulsion.

Le résultat principal sur lequel repose l'ensemble des résultats de ce travail de thèse est que l'amplitude de la force optique exercée sur un objet chiral dépend de l'hélicité de la lumière. Autrement dit, la force appliquée sur objet chiral dépend du produit $\Lambda\chi$. Notre travail, à vocation expérimentale, a donc nécessité la mise en place d'un système lumière-matière permettant une mise en évidence

expérimentale quantitative de notre proposition fondamentale. Notre choix s'est tourné vers l'utilisation de gouttelettes sphériques d'un cristal liquide nématique chiral (i.e. un cristal liquide cholestérique) dont le diamètre typique est de l'ordre d'une dizaine de microns et qui sont immergées dans un fluide visqueux isotrope (en pratique un mélange eau/glycérol). L'intérêt de ces objets est qu'ils sont susceptibles de se déplacer sans entrave, qu'ils sont suffisamment petit donner facilement accés à l'observation quantitative d'un mouvement induit par la lumière, qu'ils peuvent être fabriqués aisément, et en fin qu'ils présentent dans certaines conditions une réponse optomécanique résonante. Ainsi, non seulement nous avons pu valider le concept de force optique contrôlée par le spin du photon mais aussi apporter des démonstrations de principe de différentes applications qui en découlent et qui nous ont permis de jeter les bases d'une "optomécanique chirale". En particulier, nous avons démontré le tri de la chiralité matérielle par voie optique et réalisé une pince optique capable de piéger sélectivement un objet chiral en fonction de sa chiralité. Le manuscrit se compose de quatre chapitres qui sont brièvement détaillés dans ce qui suit.

Le chapitre 1 introduit le matériau constituant le système d'étude, les cristaux liquides cholestériques, qui sont caractérisés par un arrangement hélicoïdal de l'orientation moyenne locale des molécules auquel est associée une distance caractéristique, le pas de l'hélice. Ces matériaux sont principalement connus pour le phénomène de la réflexion de Bragg circulaire. Ce phénomène correspond au fait que l'un des deux états de polarisation circulaire ne peut pas se propager dans le matériau pour une certaine gamme de longueur d'onde qui dépend du pas cholestérique, de la biréfringence du cristal liquide et de l'angle d'incidence. Ainsi, on peut se retrouver dans une situation où un champ lumineux de polarisation circulaire donné est totalement réfléchi alors que l'état de polarisation orthogonale est transmis. Ce phénomène de réflexion résonante peut se produire que lorsque la chiralité matérielle χ et l'hélicité de la lumière Λ sont de signes opposés, soit $\Lambda\chi = -1$. On parle alors de la réflexion dite de Bragg et par opposition, on parlera du cas où $\Lambda\chi = +1$ comme de la situation anti-Bragg. Dans notre cas, nous avons formé des gouttelettes sphériques de cristal liquide cholestérique dont le pas est ajusté pour correspondre à la réflexion de Bragg pour la longueur d'onde de travail (532 nm, la source utilisée étant un laser continu). De plus, nous avons choisi des conditions aux limites (l'interface sphérique entre la goutte et le fluide dans lequel elle est immergée) qui correspondent à une orientation moléculaire paralléle à la surface de la goutte. On obtient alors une goutte cholestérique dite radiale à la quelle est associée une distribution radiale pour l'axe de l'hélice cholestérique. Pour un faisceau incident centré sur la goutte, cela permet d'obtenir une réflexion de Bragg sur une fraction de l'hémisphère illuminée définie par l'intersection de la sphère avec un cone ayant pour sommet le centre de la goutte et caractérisé par un demi-angle noté θ_B. C'est ce paramètre qui va déterminer l'importance de la dépendance de la force optique

du spin du photon. En pratique, l'angle θ_B est déterminé expérimentalement par deux méthodes indépendantes, l'une spectrométrique, l'autre d'imagerie de transmission. Une fois le système matériel présenté et caractérisé, on introduit les différents types de champs lumineux qui seront utilisés par la suite, à savoir les champs Gaussiens et Laguerre-Gaussiens. Nous avons alors en main tous les éléments nécessaires à l'exposé du modèle qui permettra de décrire quantitativement toutes les observations effectuées. Le modèle proposé est basé sur une approche de type optique géométrique qui se justifie par les tailles de gouttes utilisées, qui sont typiquement au moins dix fois plus grande que la longueur d'onde. On suppose aussi que les champs lumineux sont paraxiaux, une hypothèse bien vérifiée en pratique. On évalue alors la force élémentaire exercée sur un élément de surface quelconque de la goutte et on intègre sur toute la surface de celle-ci. Le phénomène de Bragg est pris en compte en supposant que la zone qui correspond au cône de Bragg mentionné plus haut se comporte comme un miroir parfait et qu'en dehors de cette zone, la goutte se comporte comme un diélectrique isotrope ayant pour indice de réfraction l'indice moyen du cristal liquide. Enfin, nous montrons que l'absorption résiduelle du cristal liquide et du fluide environnant joue un rôle négligeable dans les effets optomécaniques mis en jeu.

Le chapitre 2 présente la validation expérimentale du concept clé de cette thèse qui peut se résumer de la façon suivante: une goutte cholestérique radiale subie une pression de radiation optique qui dépend fortement de l'hélicité du champ incident. En pratique nous avons choisi un faisceau laser Gaussien d'extension spatiale bien plus large que le diamètre des gouttes afin de pouvoir considérer le champ incident comme étant une onde plane. Dans ce cas, on obtient une formulation analytique des forces optiques exercées sur la goutte et des vitesses de déplacement qui en résultent. Dans notre cas, le mouvement des gouttes dans le cas Bragg est environ trois fois plus rapide que dans le cas anti-Bragg, et ce contraste de vitesse est indépendant de la taille de la goutte. Tout ceci est effectivement prédit par notre modèle et les vitesses obtenues sont en accord quantitatifs avec les simulations. Dans un deuxième temps nous avons cherché à optimiser ce contraste de vitesse entre les cas Bragg et anti-Bragg. Pour cela, nous avons proposé l'utilisation de deux faisceaux coaxiaux, contrapropageants, de diamètre et de puissance identiques et de polarisation circulaire. On obtient alors une compensation parfaite de la contribution anti-Bragg de chacun des deux faisceaux à l'extérieur de la zone de la goutte qui correspond à la réflexion de Bragg. Ainsi, en modifiant l'hélicité d'un des deux faisceaux, la goutte subie une force ou pas. On obtient ainsi une discrimination totale de la force optique appliquée sur la goutte, dont les dépendances en fonction de la puissance lumineuse et du rayon de la goutte ont été obtenues et validées théoriquement. Les deux chapitres suivants visent à exploiter cette sélectivité optomécanique dans le but de trier (chapitre 3) ou piéger (chapitre 4) des particules chirales selon leur chiralité.

Le chapitre 3 est consacré au tri passif de la chiralité matérielle par la lumière chirale dont les enjeux sont immenses en termes dès lors qu'on envisage d'étendre ce principe à l'échelle moléculaire, où les besoins industriels sont très importants (e.g. industries chimiques, pharmaceutiques, agroalimentaires). Dans le but de réaliser la première démonstration expérimentale de principe, nous avons choisi une situation où des gouttes sont advectées par un écoulement du fluide dans lequel elles sont plongées et dont la trajectoire est perpendiculaire à la direction de deux faisceaux Gaussien coaxiaux, contra-propageants, de diamètre et de puissance identiques et d'hélicité opposée. Une goutte non-chirale étant soumise à des forces optiques provenant des deux faisceaux qui s'annulent mutuellement, sa trajectoire rectiligne initiale n'est pas perturbée. Au contraire, la trajectoire d'une goutte chirale sera déviée vers la source du faisceau anti-Bragg, qui exerce sur celle-ci une force moindre que le faisceau Bragg. Le signe de la déviation de la trajectoire de la goutte dépend donc du signe du produit $\Lambda\chi$. La démonstration expérimentale utilise des gouttes cholestériques radiales droites ou gauches comme objets chiraux et des gouttes de fluide isotrope ou de cristal liquide non chiral pour le cas d'objets non chiraux. Une étude expérimentale paramétrique de l'amplitude de la déviation et de la forme de la trajectoire en fonction de la puissance lumineuse et de la vitesse initiale des gouttes est effectuée. Les résultats obtenus sont tous décrits quantitativement par notre modèle dont l'extension à deux faisceaux est effectuée. De plus, nous montrons que ce principe de tri optofluidique de la chiralité matérielle par de la lumière chirale fonctionne indépendamment du phénomène de Bragg. L'avantage de ce dernier est d'avoir une réponse optomécanique résonante et donc de faciliter les observations, cependant nous soulignons l'importance de s'en affranchir. En effet, cela permet d'envisager l'utilisation de la démarche proposée à un matériau chiral quelconque. Enfin, le chapitre se conclut par une discussion de la réalisation d'un trieur chiral optique passif basé sur l'utilisation d'une puce opto-microfluidique.

Le chapitre 4 décrit quant à lui l'utilisation de forces optiques qui dépendent de l'hélicité de la lumière pour le piégeage optique tridimensionnel sélectif en fonction de la chiralité de l'objet d'étude. A nouveau on utilise les gouttes cholestériques radiales et on met en place un système à deux faisceaux coaxiaux, contra-propageants, de diamètre et de puissance identiques, mais cette fois-ci avec une hélicité identique. L'utilisation de faisceaux modérément focalisés ayant des plans focaux distincts permet alors de piéger tri-dimensionnellement des gouttes sur l'axe des faisceaux. Ici, on a l'étude théorique à précéder les expériences, ce qui a permis de déterminer les paramètres géométriques pertinents du système lumière-matière. Nous avons ainsi montré le signe de $\Lambda\chi$, la taille des gouttes, la divergence des faisceaux et la distance interfocale sont autant de paramètre essentiels à prendre en considération. Des simulations numériques exhaustives, incluant le cas de faisceaux Gaussiens ou Laguerre-Gaussiens, ont permis de proposer différents designs expérimentaux. Les expériences ont été réalisées et les

différents comportements prévus théoriquement ont été retrouvés en pratique. De plus, nous avons mis en place un protocole de mesure du champ de force optique, ce qui a permis de valider quantitativement nos résultats de simulations.

Le manuscrit se termine par une conclusion résumant les principaux résultats obtenus et offrant un bref aperçu des perspectives du travail réalisé. En particulier, l'extension à l'échelle moléculaire du principe de tri de la chiralité matérielle par voie optique, démontré ici à l'échelle micrométrique, est un défi majeur méritant qu'on y prête attention.

Acknowledgements

I would like to express my deep gratitude to Etienne Brasselet, who initiated this work and has been a patient and encouraging supervisor during my study at the University of Bordeaux. I would like to thank the friendly and efficient staff of Laboratoire Ondes et Matière d'Aquitaine and the director, Jean-Pierre Delville, for accepting me to this scientific community.

It was a real pleasure for me to be a member of the team "Singular Optics and Liquid Crystals" led by Etienne. In particular, I wish to thank Charles for his invaluable help with both scientific and personal questions, as well as for the energy and time he spent while teaching me French language and culture. I am grateful to Mohamed for his calm practical explanations, which were extremely useful for me, especially at the beginning of the experimental studies. I wish to thank Maxim, Tetiana, Artur, Davit, Mushegh and Hernando, who readily shared with me their time, knowledge and equipment. I am sure this young enthusiastic team has a great future.

I would like to extend my thanks to Sandra, Eddie and Levi from the mechanical workshop for their professional assistance with various parts for my experimental set-ups. Also, I am grateful to the specialists from the IT service, Hassan and Alain, who were always ready to solve any technical problem I came to them with.

Finally, I wish to thank my parents for their support throughout my study. And special thanks to my wife, Natasha, who shared with me these intense years of work and to whom I dedicate this manuscript.

Contents

Introduction

Optical radiation forces have a huge area of application - from biochemistry and medicine to micromachining and laser cooling - wherever is a need for contactless manipulation of inert or living entities ranging from nano- to submillimeter scale [1]. Such forces are the mechanical manifestation of the transfer of linear momentum from light to matter, which basically occurs when light is absorbed, reflected, refracted or scattered in the course of its propagation (see the sketches in Fig. 1, where $\mathbf{p}_{\text{in}}$ and $\mathbf{p}_{\text{out}}$ stand for the input and output photon linear momenta). For instance, discontinuity of the refractive index at the interface between two transparent and homogeneous dielectric media leads to optical radiation pressure that enables the displacement of solids [2, 3] or the deformation of fluid interfaces [4].

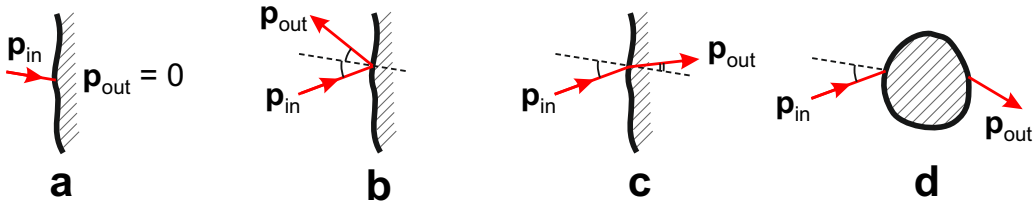

Figure 1: *Change of linear momentum of light due to (**a**) absorption, (**b**) reflection, (**c**) refraction or (**d**) scattering results in the optical radiation pressure on the illuminated interface. The photon linear momentum before and after the light-matter interaction is labeled as* $\mathbf{p}_{\text{in}}$ *and* $\mathbf{p}_{\text{out}}$*, respectively. Arrows indicate the direction of propagation for the corresponding photons.*

According to the first principle of mechanics, the light-induced force exerted on the illuminated material object is

$$\mathbf{F} = (\mathbf{p}_{\text{in}} - \mathbf{p}_{\text{out}}) \frac{dN}{dt}, \tag{1}$$

where dN is the number of photons hitting the object during the time dt. As one can see from this expression, the optical force can be controlled either by the photon linear momentum difference (for example, by tuning the incidence angle or refractive indices), or by the photon flux, which is the number of photons per unit area per unit time. The main question addressed in this thesis is following: is there an alternative way for optical manipulation of the linear momentum of matter besides "shaping" of the linear momentum of light?

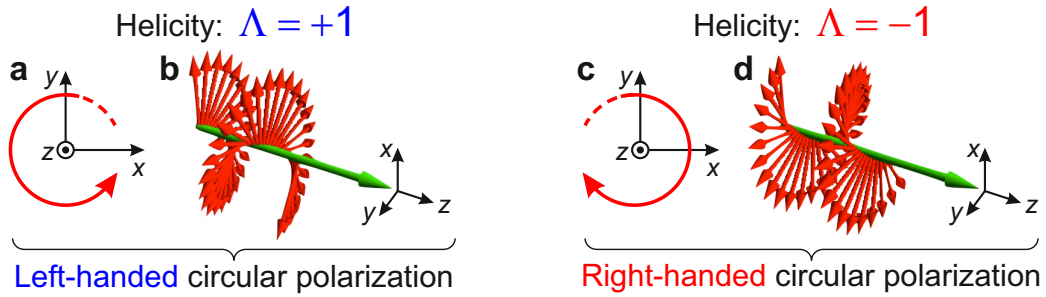

Figure 2: *A plane circularly polarized electromagnetic wave propagates along the z axis of the Cartesian coordinate system (x, y, z). (**a**, **b**) Left-handed circular polarization state corresponds to counter-clockwise (if the wave approaches the observer) rotation of the electric field vector tip in the plane z = const (**a**) and to the right-screwed instant image of the electric field vector (**b**). The photon spin projection on the z axis equals +1. (**c**, **d**) In contrast, the right-handed circular polarization state is characterized by the clockwise electric field rotation in the plane z = const (**c**), left-screwed instant image of the electric field vector (**d**) and z-projection of the photon spin equal to −1. The photon helicity Λ, which is the projection of the photon spin on its propagation direction, equals to ±1 for the left/right-handed circular polarization.*

Our answer is: yes, if another degree of freedom of a photon is involved, namely, its spin angular momentum. The photon spin refers to rotation of the electric field vector in an electromagnetic wave. If the vector length does not change in time, such a wave is said to be circularly polarized with right or left handedness depending on the sense of the rotation, as sketched in Fig 2 in accordance with the convention commonly used in electrodynamics [5]. In this study, when referring to photons in circularly polarized beams, we use the parameter Λ called "helicity" and defined as the projection of the spin angular momentum of an elementary particle on its propagation direction [6]. Helicity is expressed in the units of $\hbar$, which is the reduced Planck constant.

Circular polarization is a manifestation of the chirality of light. In general, chirality refers to the lack of mirror symmetry and plays a fundamental role in

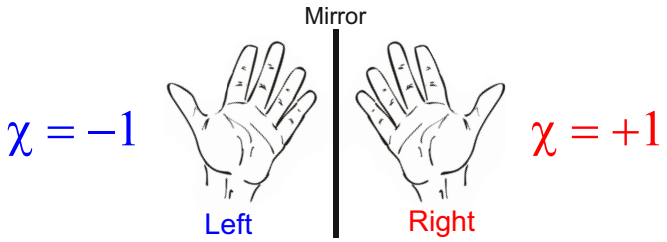

Figure 3: *Human hands as an example of mirror-imaged chiral entities.*

physics, chemistry and life sciences. A system whose mirror images cannot be superimposed by rotations and translations in space is said to be chiral. A basic example is our two hands (see Fig. 3), just like the Greek etymology ("kheir") recalls. Quite naturally, two mirror images of a chiral entity are referred to as right- and left-handed versions of it. Following the general convention (see for instance [7]), in this work we assign the chirality $\chi = \pm 1$ to the right/left-handed entities, as shown in Fig. 3.

Our proposal towards the control of optical radiation forces is based on the interplay between the chirality of light and chirality of matter. We aim at an unambiguous demonstration of the photon helicity's potential as a tool for enhanced optical manipulation of material chiral objects.

To this aim, we have performed quantitative experimental study organized in four coherent projects, each of them being dedicated to a single well-defined scientific problem. The material of this manuscript is organized into four chapters according to the following structure:

Chapter 1 - Materials, fields and methods
This chapter introduces the chiral light-matter system under study and describes our approach towards modeling of the dynamics of the chosen chiral object driven by the used chiral light field.

Chapter 2 - Helicity-controlled optical radiation force
In this chapter we demonstrate experimentally that light-induced displacement of chiral microparticles can be addressed via the photon helicity. The full control of the particle displacement is achieved by means of a scheme with two counter-propagating plane-wave-like fields, each of them corresponding to a pure photon helicity state.

Chapter 3 - Optofluidic sorting of material chirality by chiral light
This chapter sets forth an application of the helicity-controlled optical manipulation principle to passive optical separation, in a fluidic environment, of mirror-imaged chiral microparticles that differ only by opposite handedness, by using chiral light fields. The quantitative experimental study of light-induced trajectories of chiral microparticles is supported by the appropriate theoretical description. Importantly, the proposed optofluidic strategy does not require chiral-shaped microparticles and actually relies on the chirality of the medium, in contrast to previous experimental demonstrations of chiral sorting based on hydrodynamical effects.

Chapter 4 - Helicity-dependent 3D optical trapping of chiral microspheres
In this chapter we address the localization of chiral objects by chiral light fields.

The helicity-dependent optical trapping of chiral spherical microparticles is demonstrated, both experimentally and theoretically, using chiral light fields with either bell- or doughnut-shaped transverse intensity distribution. The reported results allow considering on-demand selective trapping of chiral particles whatever the photon helicity and the particle size, thereby circumventing the inherent limitations associated with the use of single-beam optical tweezers.

CHAPTER 1

Materials, fields and methods

In this chapter we present the working environment of the study. Namely, in section 1.1 we describe the investigated chiral object and the physical mechanism at the origin of the reported optomechanical effects mediated by the photon helicity. Then, section 1.2 introduces the chiral light field, which is applied for optical trapping and manipulation of the above chiral object. The model used to describe the optical radiation forces in the investigated light-matter system is set forth in section 1.3, where all key assumptions are identified and discussed.

1.1 Chiral object of study

In this work we investigate optical radiation forces that depend on the chirality of light and matter. Typical optical forces exerted on matter are generally of a small magnitude. Namely, if one considers the force F exerted on a perfect mirror by a light beam, one finds $F = 2P/c$, where P is the beam power and c the speed of light. This gives $F \sim 1$ nN for $P \sim 100$ mW. Such a modest force value implies to deal with small size objects if one aims at observing vivid optomechanical effects such as light-induced displacements. Consequently, in principle, the desired chiral object should:

- be free to move;
- be sufficiently small to give access to observable light-induced motion;
- exhibit strong helicity-dependent interaction with light;
- be easy to fabricate and align in the driving light field.

In practice we found that a radial microscopic droplet of cholesteric liquid crystal (i. e. a chiral nematic mesophase) perfectly meets all the above requirements. Indeed, such a droplet can be easily made by mechanical stirring of a small amount of cholesteric liquid crystal in water or whatever immiscible fluid that provides planar alignment of the liquid crystal orientation at the interface. Such a boundary condition may lead to formation of a liquid crystal droplet with radially symmetric bulk ordering responsible for resonant optomechanical effects that are highly sensitive to the chirality of the material. In addition, a droplet

is free to move in the fluid where it is immersed, and an overall radial symmetry formally saves us from the necessity to align such microscopic chiral objects in the optical system.

In what follows, we present the cholesteric liquid crystal material and its key optical properties on which is based the study reported in this manuscript. Then we focus on the particular case of radial cholesteric droplets that have been used all along our investigation.

1.1.1 Cholesteric liquid crystal

Cholesteric is an optically anisotropic dielectric medium obtained from a nematic liquid crystal mixed with a chiral dopant, as sketched in Fig. 1.1. The resultant mesophase is described by a director $\mathbf{n}$ (a unit vector directed along the average local molecular orientation, $\mathbf{n}$ and $-\mathbf{n}$ being equivalent) rotating by 2π around the axis of a supramolecular helix over a distance p called the cholesteric pitch. Such a chiral ordering can be left- or right-handed, which corresponds to the chirality $\chi = +1$ or $\chi = -1$, respectively.

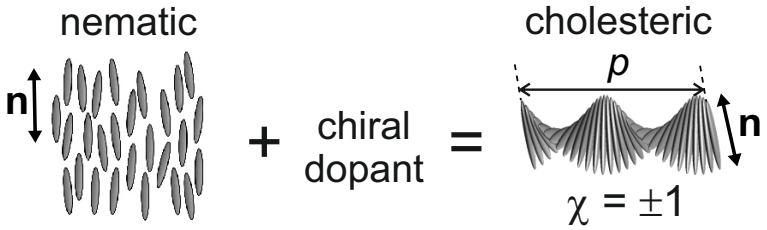

Figure 1.1: *Mixing a nematic liquid crystal (having parallel volumetric alignment of the director* $\mathbf{n}$*) with a chiral dopant results in the cholesteric mesophase, which is characterized by helical supramolecular ordering with a well-defined pitch* p*.*

Then, in order to present the applied in this work fundamental feature of cholesterics, let us consider a planar film of a cholesteric liquid crystal with chirality χ and planar alignment of the molecules at both sides of the film. In that case, axes of supramolecular helices are oriented perpendicularly to the plane of the film, as sketched in Fig. 1.2(a), where the helix axes are shown as thin solid lines. Then, let us assume that the film is illuminated by unpolarized (see "UNPOL" in panel (a)) light at normal incidence. In practice, the incident light can be described by two equally-intense circularly polarized fields with opposite photon helicities.

The field with helicity $\Lambda_{\mathrm{B}} = -\chi$ ("B" standing for "Bragg") can "read" the effective periodicity of the refractive index (schematically shown by the gradient gray-scale fill on the sketch), which appears in the film due to the helical distribution of the optical anisotropy (see for instance [8]). The constructive interference

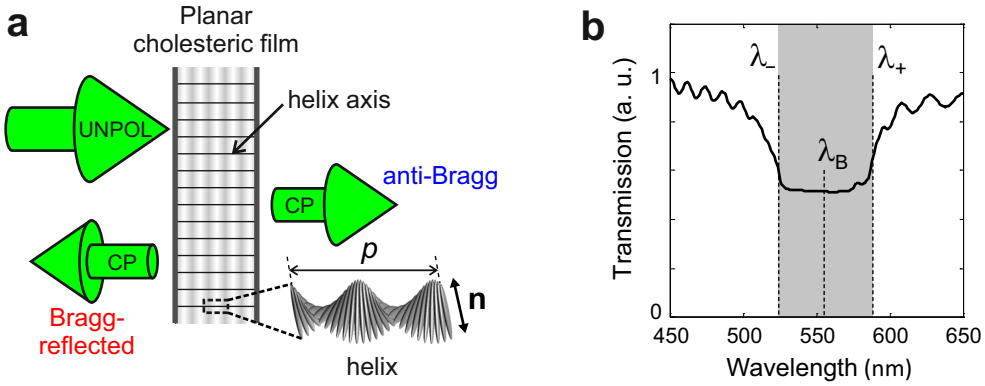

Figure 1.2: (**a**) *A planar film of cholesteric liquid crystal with pitch p, chirality* χ *and uniform alignment of helical axes (thin solid lines) along the normal to the film is illuminated by an unpolarized light at normal incidence (wavelength lays between* λ_- *and* λ_+*, see the text). The gradient gray-scale fill expresses the effective multilayer structure associated with the helical distribution of the optical anisotropy. Due to the circular Bragg phenomenon, the film strongly reflects the photons having* $\Lambda = -\chi$*, whereas photons with* $\Lambda = +\chi$ *are transmitted.* (**b**) *Unpolarized transmission spectrum of a* 10 μ*m thick film of the right-handed cholesteric mixture MDA-02-3211. The circular photonic bandgap associated with* 50% *transmission due to Bragg reflection of the right-handed circularly polarized part of the incident light is shown in gray color.*

of light reflected from this effective multilayer structure results in the well-known Bragg phenomenon [9], which expresses itself by the photonic bandgap appearing in the transmission spectrum of the structure, as shown by the gray area in Fig. 1.2(b).

On the other hand, the field component with helicity $\Lambda_{AB} = +\chi$ ("AB" standing for "anti-Bragg" in order to emphasize the absence of Bragg reflection) and is transmitted through the film. As a result, the unpolarized transmission spectrum of the film exhibits only 50 % of attenuation within the bandgap due to the selective resonant reflection of Bragg-polarized part of the incident light.

Quantitatively, the bandgap in the spectrum of a planar cholesteric film is described by the wavelength range

$$\Delta\lambda = \lambda_+ - \lambda_- = p(n_\parallel - n_\perp) = p\Delta n\,, \tag{1.1}$$

where $n_{\parallel,\perp}$ are the refractive indices parallel and perpendicular to the director **n** [8]. This range is centered on the wavelength

$$\lambda_B = \frac{\lambda_+ - \lambda_-}{2} = pn \tag{1.2}$$

with $n = (n_\parallel + n_\perp)/2$ the average refractive index of the liquid crystal. In this study we use the right-handed cholesteric mixture MDA-02-3211 (from Merck)

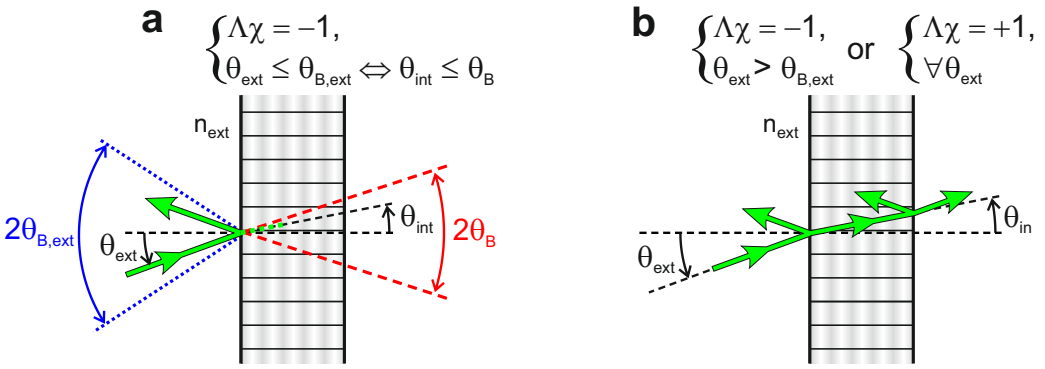

Figure 1.3: *(**a**) Bragg-polarized light is completely reflected if its incident angle falls within the cone having the half-apex angle* $\theta_{\mathrm{B,ext}}$. *(**b**) Circular Bragg reflection is absent either if the incidence angle exceeds* $\theta_{\mathrm{B,ext}}$ *and the light is Bragg-polarized, or for any incidence angle if the polarization is anti-Bragg.*

having pitch $p = 347$ nm and refractive indices $n_{\parallel} = 1.7013$ and $n_{\perp} = 1.5064$ (hence $n \approx 1.6$) at 589.3 nm wavelength and temperature 20°C [1]. As follows from the spectrum shown in Fig. 1.2b, circular Bragg reflection band of MDA-02-3211 is centered at $\lambda_{\mathrm{B}} \approx 555$ nm and ranges from $\lambda_{-} \approx 524$ nm to $\lambda_{+} \approx 588$ nm [2].

As we known from the theory of multilayer Bragg reflectors [9], resonant reflection occurs when the phase delay between light waves reflected from two successive layers is a multiple of π. In the case of oblique incidence, the phase delay is proportional to $\cos\theta_{\mathrm{int}}$ with θ_{int} the refraction angle counted from the normal to the cholesteric interface, as shown in Fig. 1.3. Consequently, at oblique incidence the circular Bragg reflection band experiences a blue-shift with respect to the spectrum at normal incidence. The shifted circular photonic bandgap will is centered at the wavelength

$$\lambda'_{\mathrm{B}} = \lambda_{\mathrm{B}} \cos\theta_{\mathrm{int}}. \tag{1.3}$$

At fixed incident wavelength λ_0, resonant reflection thus occurs for Bragg-polarized light over a range of refraction angles $0 \le \theta_{\mathrm{int}} \le \theta_{\mathrm{B}}$(Fig. 1.3a), where θ_{B} refers to the "intrinsic Bragg angle". In fact, θ_{B} corresponds to the situation when λ_0 exceeds the blue-shifted upper limit λ_{+}. Using Eqs. (1.1), (1.2) and Eq. (1.3) with $\theta_{\mathrm{int}} \equiv \theta_{\mathrm{B}}$, we get

$$\left(\lambda_{+} - \frac{p\Delta n}{2}\right)\cos\theta_{\mathrm{B}} = \lambda_0 - \frac{p\Delta n}{2}. \tag{1.4}$$

[1] Within the visible range, if the wavelength varies by a few tens of nanometers, refractive indices of a liquid crystal can change due to the chromatic dispersion typically within 1% [10], which we neglect here.

[2] The edges are defined as the global minimum and maximum of the differentiated transmission spectrum.

Accounting for $p\Delta n/2 \ll \lambda_{0,+}$, this gives

$$\theta_B = \arccos(\lambda_0/\lambda_+)\,. \tag{1.5}$$

In accordance with the Snell-Descartes law, the "extrinsic" Bragg angle $\theta_{B,ext}$ corresponding to $\theta_{int} \equiv \theta_B$, equals

$$\theta_{B,ext} = \arcsin[(n/n_{ext})\sin\theta_B]\,, \tag{1.6}$$

where n_{ext} is the refractive index of the surrounding medium.

On the other hand, light with anti-Bragg circular polarization state ($\Lambda\chi = +1$) is scattered by the cholesteric film as if it was a usual dielectric slab of refractive index n (Fig. 1.3b) for all incidence angles $0 \le \theta_{ext} \le \pi/2$. Propagation of light in this case follows the Fresnel's equations [11]. The same behavior occurs for the Bragg-polarized light impinging at $\theta_{B,ext} < \theta_{ext} \le \pi/2$.

1.1.2 Radial cholesteric droplets

Radial cholesteric droplets of typical radius $R \sim 10\,\mu m \gg p$ by mechanical stirring of MDA-02-3211 in an aqueous solution of glycerol. Such a mixture is chosen for immersion of cholesteric droplets since (i) its density can be easily tuned via the glycerol fraction and (ii) it provides planar alignment of liquid crystal molecules at the interface. Different types of the structure are obtained depending on the ratio between the droplet radius R and pitch p [12]. In the particular case of $R \gg p$, one gets onion-like droplets that behave as omnidirectional circular Bragg reflectors. Such a radial cholesteric droplet is sketched in Fig. 1.4.

As we discussed above, the circular Bragg effect occurs in cholesteric films within the Bragg cone having the apex angle $2\theta_B$. In the case of spherical droplets, radial arrangement of the helix axes makes the incident light tilted to the local supramolecular structure, unless the incidence is normal to the droplet surface. If a radial cholesteric droplet of chirality χ is illuminated by a beam with a planar wavefront, wavelength $\lambda_- < \lambda_0 < \lambda_+$ and helicity $\Lambda = -\chi$, the droplet completely reflects the photons impinging on the spherical interface at

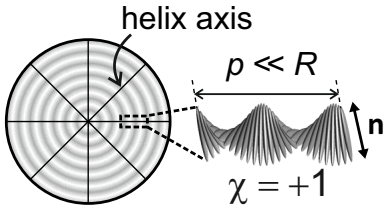

Figure 1.4: *A radial cholesteric droplet represents an onion-like effective multilayer structure with the pitch p. Thin solid lines indicate orientation of axes of supramolecular helices.*

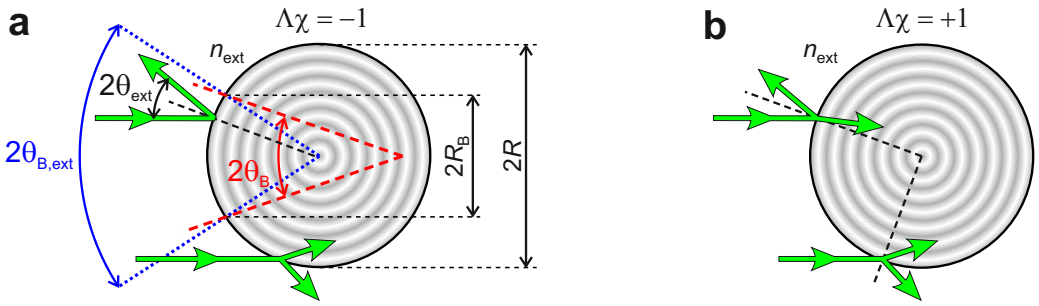

Figure 1.5: *A radial cholesteric droplet illuminated by a plane wave-like beam. (**a**) The Bragg-polarized light is completely reflected if impinging the droplet interface at the angle* $0 \le \theta_{\mathrm{ext}} \le \theta_{\mathrm{B,ext}}$. *(**b**) Circular Bragg reflection is absent for the opposite polarization handedness, regardless of* θ_{ext}.

angles $0 \le \theta_{\mathrm{ext}} \le \theta_{\mathrm{B,ext}}$, whereas the other photons are scattered without Bragg reflection as shown in Fig. 1.5a (thin lines represent helix axes). Intersection of the Bragg cone with the droplet surface is a circle of radius

$$R_{\mathrm{B}} = R \sin \theta_{\mathrm{B,ext}} \,. \tag{1.7}$$

In the case of anti-Bragg polarization state ($\Lambda = +\chi$, see Fig. 1.5b), the incident photons are scattered as if the droplet was a uniform dielectric sphere, for all incidence angles, similar to the situation sketched in Fig. 1.3b.

The above statements are confirmed by the microscopic analysis of a radial droplet of MDA-02-3211 (radius $R = 25$ μm, in a 26 wt. % aqueous glycerol solution) over the visible range of light, namely, under red (633 nm), green (532 nm), blue (488 nm) and white light illumination (colored light was provided by appropriate interference filters). Fig. 1.6 compiles the transmission images obtained by the means of a microscope objective (Nikon M Plan ELWD, magnification ×40, numerical aperture NA = 0.5) and a complementary metal-oxide-semiconductor (CMOS) camera (DCC1645C from Thorlabs). The snapshots are taken under unpolarized ("UNPOL"), left- and right-handed circular polarized ("LHCP" and "RHCP", respectively) illumination, and between crossed linear polarizers ("XPOL").

The fourfold intensity patterns in the "XPOL" panels indicate the radially symmetric optical anisotropy of supramolecular organization within the cholesteric droplet [12]. The dark radial line seen in most of the snapshots (for instance, it is indicated by the white arrow in panel "LHCP" for wight light), it is the radial defect, which is typical for cholesteric droplets with planar alignment of the director at the spherical surface and radius $R \gg p$ [13, 14] [3]. The circular Bragg

[3] According to the hairy ball theorem of algebraic topology [15], the director field at the spherical interface must contain at least one point with homeotropic alignment. The radial

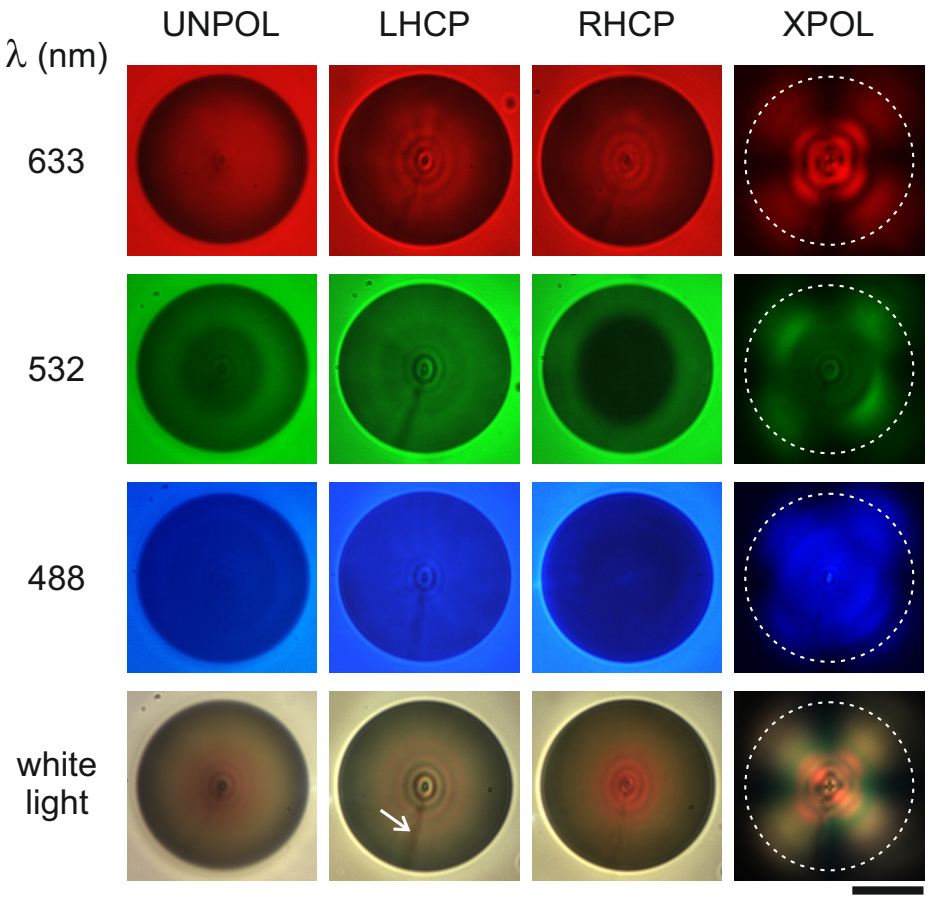

Figure 1.6: *Transmission of a radial droplet of MDA-02-3211 under illumination at various wavelength and polarization conditions. The droplet is immersed in a 26 wt. % aqueous glycerol solution within a glass capillary having* 1×1 *mm square cross-section. Glycerol fraction for the best density matching has been selected experimentally from direct observations of the droplet motion at rest. Unpolarized white light from a halogen source OSL1-EC (Thorlabs, Inc.) is directed at the sample through a convex lens with 35 mm focal length. Colored illumination is obtained via interference filters introduced before the lens. A linear polarizer and a wide-band quarter-wave plate provide the two circular polarization states. Dashed circles in the XPOL panels indicate the droplet contour, white arrow shows the radial defect (only on one panel, as an example). Scale bar is* 20 μm.

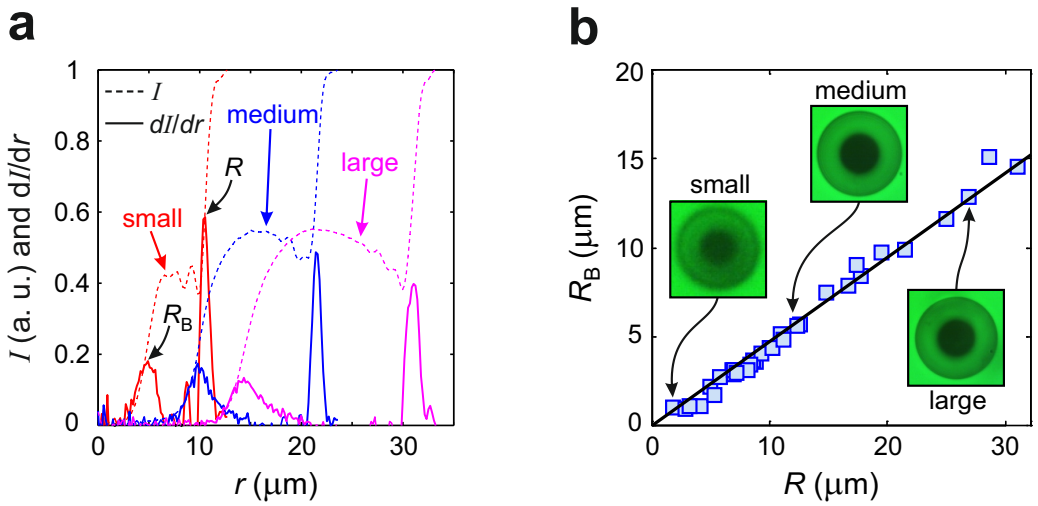

Figure 1.7: *In situ characterization of the Bragg cone angle of radial droplets of MDA-02-3211.* (**a**) *Analysis of the intensity distribution in the transmission images of radial cholesteric droplets in glycerol observed under uniform illumination at* $\lambda_0 = 532$ *nm and Bragg incident circular polarization state (three typical droplets of different sizes are presented). The intensity at every pixel captured by the used 8-bit CMOS camera ranges from* 0 *to* 255. (**b**) *Data show the radius* R_B *of the zero-transmission area as a function of the droplet radius* R. *Solid line is the best linear fit.*

reflection expresses itself by the dark disk mostly visible under green RHCP illumination. In the case of white light, the reddish zone around the droplet center in the RHCP snapshot confirms the complete reflection in the green spectral region.

In the reported experimental studies of the helicity-dependent optomechanical effects, we use a diode-pumped solid state laser Millennia Xs (from Spectra-Physics, Inc.) which emits monochromatic light at $\lambda_0 = 532$ nm wavelength with optical power grater than 5 W in the continuous wave regime. High power facilitates observation of the optomechanical effects, while the wavelength is close enough to λ_- (the lower limit of the Bragg range of the chosen cholesteric liquid crystal) for providing a larger Bragg cone angle, which is facilitating our experimental demonstrations. Using Eq. (1.5), we estimate the intrinsic Bragg angle of MDA-02-3211 as $\theta_B = 25.1°$.

The dark disk of radius R_B (Fig. 1.5a) visible under the Bragg-polarized transmission (Fig. 1.6, green under RHCP) gives access to the Bragg angle of the radial cholesteric droplets in situ. In order to estimate the Bragg angle, we have measured R and R_B for various spherical droplets of MDA-02-3211 dispersed in

defect of the supramolecular structure starts at this point and is inevitably present in every cholesteric droplet.

pure glycerol. The droplets were imaged by means of the Olympus IX71 inverted microscope through the objective Thorlabs LMH-20X-532 (magnification ×20, numerical aperture NA = 0.4) and captured via a CMOS camera. The droplet radius R and the Bragg cone radius R_{B} are measured via numerical analysis of the recorded image. The intensity at every pixel captured by this 8-bit digital camera ranges from 0 to 255.

The analysis protocol consists in azimuthal averaging of the image intensity distribution by fixing the origin at the center of the droplet and differentiating the obtained intensity profile. Then, the radii are easily and precisely determined by locating the corresponding maxima of the differentiated intensity profile. Fig. 1.7a shows the results of data analysis for three different droplets (relatively small, medium and large), I being the normalized azimuthally averaged intensity distribution, dI/dr - its first derivative by the radial coordinate r.

The measured radii for the analyzed collection of droplets are presented in Fig. 1.7b, where the solid line is the best linear fit of R_{B} as a function of R. As follows from Eq. (1.7), the slope of the fit equals $\sin\theta_{\mathrm{B,ext}}$, from which, using Eq. (1.6), we derive the intrinsic Bragg angle $\theta_{\mathrm{B}} = 25.8°$ - in a good agreement with the spectroscopic characterization presented above.

1.2 Chiral light fields

Chirality of the optical fields applied in this study is expressed by the photon helicity $\Lambda = \pm 1$, which corresponds to left- and right-handed circular polarization states. For the purpose of optical trapping and manipulation of chiral microspheres we use laser beams having axially-symmetric spatial intensity distributions described by the Laguerre-Gaussian modes $\mathrm{LG}_{0,\ell}$ with ℓ the azimuthal index. These modes are solutions of the wave equation for electromagnetic fields under the paraxial approximation, which considers the transverse dimensions of the beam being much smaller than its typical longitudinal dimension [16].

Electric field amplitude in the $\mathrm{LG}_{0,\ell}$ mode is commonly presented in the cylindrical coordinate system (r, φ - radial and azimuthal coordinates, z indicates the beam propagation direction) as follows

$$\begin{aligned} E(r,\varphi,z) &= \mathrm{C}\frac{w_0}{w(z)}\left(\frac{r\sqrt{2}}{w(z)}\right)^{|\ell|}\exp\left(-\frac{r^2}{w^2(z)}\right) \\ &\times \exp\left(-\frac{ikr^2z}{2(z^2+z_{\mathrm{R}}^2)}\right)\exp\left(i(|\ell|+1)\tan^{-1}\frac{z}{z_{\mathrm{R}}}\right)\exp(i\ell\varphi)\,, \end{aligned} \tag{1.8}$$

where the parameters are: normalization constant C, beam waist w_0, beam radius $w(z) = w_0\sqrt{1+(z/z_R)^2}$, Rayleigh range $z_{\mathrm{R}} = \pi w_0^2/\lambda$ (with λ the wavelength) and Gouy phase shift $\tan^{-1}\frac{z}{z_{\mathrm{R}}}$.

The case $\ell = 0$ corresponds to the Gaussian mode - the fundamental transverse mode TEM_{00} of laser resonators. Gaussian beams have bell-shaped transverse intensity profiles and are widely used in optical tweezers, where gradient of intensity gives rise to restoring optical forces allowing to trap absorbing or scattering high-index (with respect to the environment) microparticles by light around the beam waist ($z = 0$). Besides the ease of generation, these beams have the axially symmetrical intensity distribution, which facilitates modeling and realization of the optical manipulation schemes.

Due to the $\exp(i\ell\varphi)$ factor, phase of the $LG_{0,\ell}$ field varies by $2\pi\ell$ along the closed loop around the axis of the beam in the transverse plane. Consequently, the Poynting vector describing the radiation energy propagation is spiraling around the beam axis, forming so-called optical vortex of topological charge ℓ [17]. A spiraling phase front in a vortex beam implies on-axis phase singularity (i. e. local indefiniteness), which forbids the field existence on the beam axis. Hence, the transverse intensity distribution of a $LG_{0,\ell}$ has a doughnut-shaped profile. Vortex beams have been successfully applied for optical trapping of low-index particles around the beam axis [18].

Let us express the normalization constant from Eq. (1.8) as a function of radiation power P, which can be measured experimentally for the given laser beam, and thus gives access to the beam intensity at every point. In a medium of refractive index n_0, an electromagnetic wave with the electric field amplitude $E(r, \varphi, z)$ has the time-averaged intensity

$$I(r,\varphi,z) = \frac{cn_0\epsilon_0}{2}|E(r,\varphi,z)|^2 = C^2\frac{cn_0\epsilon_0 w_0^2}{2w(z)^2}\left(\frac{r\sqrt{2}}{w(z)}\right)^{2|\ell|}\exp\left(-\frac{2r^2}{w^2(z)}\right), \qquad (1.9)$$

where c is the speed of light in vacuum, ϵ_0 is the vacuum permittivity. Noticeably, the local intensity is independent of the azimuthal coordinate φ, hence such beams have axially symmetric spatial intensity distribution $I(r, z)$. By definition, the intensity at (r, φ, z) equals the radiation power transmitted trough the elementary surface $dS(r, \varphi, z)$ normal to the local wavevector [9]. Under the plane-wave approximation (valid if the beam divergence $\theta_0 = \lambda/(\pi w_0) \ll 1$), the wavevector at (r, φ, z) can be considered perpendicular to the beam cross-section at z, and in view of $dS(r, \varphi, z) = rdrd\varphi$ the radiation power of the beam is

$$\begin{aligned} P &= \int\int_S I dS = \int_0^{2\pi}\int_0^{\infty} I r dr d\varphi \\ &= C^2\frac{2^{|\ell|}\pi c n_0\epsilon_0 w_0^2}{w(z)^{2|\ell|+2}}\int_0^{\infty} r^{2|\ell|+1}\exp\left(-\frac{2r^2}{w^2(z)}\right)dr, \end{aligned} \qquad (1.10)$$

which gives

$$C^2 = \frac{4P}{\pi c n_0\epsilon_0 w_0^2 \ell!}. \qquad (1.11)$$

Substituting Eq. (1.11) into (1.9), we get the following expression linking the local intensity $I(r,z)$ with the power P of the $\mathrm{LG}_{0,\ell}$ beam:

$$I(r,z) = \frac{2^{|\ell|+1}P}{\pi \ell! w^2(z)} \left(\frac{r}{w(z)}\right)^{2|\ell|} \exp\left(-\frac{2r^2}{w^2(z)}\right). \tag{1.12}$$

1.3 Modeling optomechanics of Bragg cholesteric droplets

Rigorous treatment of light propagation in cholesteric films is not an easy task, though literature is available on this topic since a long time [19]. Nevertheless, in principle, this can be done numerically [20]. It becomes even trickier when considering curved cholesteric structures including droplets. In particular, scattering of light by a chiral particle is an issue that has started to be addressed only recently [21, 22]. Moreover, Maxwell stress tensor formalism for inhomogeneous, chiral and anisotropic optical media should be included as well as possible light-induced deformation of the shape of the droplet [23]. However, a simple but accurate physical picture of the problem can be handled from the following assumptions.

1.3.1 Main assumptions

(i) The working wavelength $\lambda_0 = 532$ nm is much smaller than the droplet radius $R \sim 10$ μm. Therefore, we describe light scattering in a ray-optics approach.

(ii) Within ray-optics description, the net force exerted on the cholesteric droplet is evaluated by calculating the net change of linear momentum of the light field as it interacts with the droplet. For this purpose, we attribute the Minkowski linear momentum $\hbar k$ per photon pointing along each geometrical ray, where k is the wavenumber in the considered medium. Such a procedure has indeed been validated experimentally [24, 25] and demonstrated theoretically [26] for the problem of optical radiation pressure exerted on a mirror immersed in a dielectric fluid.

(iii) Since the circular polarization photonic bandgap has relatively sharp edges (see the spectrum in Fig. 1.2b and the zero-transmission disks in Fig. 1.7), a radial cholesteric droplet is considered as a perfectly reflecting mirror for incident angles $\theta_{\mathrm{ext}} \leq \theta_{\mathrm{B,ext}}$ [4] in the Bragg case and as a usual dielectric sphere of refractive index

[4] The incident angle $0 \leq \theta_{\mathrm{ext}} \leq \pi/2$ counts from the perpendicular to the droplet surface at the hitting point for the geometrical ray.

$n = (n_\parallel + n_\perp)/2$ otherwise (i.e. when $\theta_{\mathrm{B,ext}} < \theta_{\mathrm{ext}} \leq \pi/2$ in the Bragg case and $0 \leq \theta_{\mathrm{ext}} \leq \pi/2$ in the anti-Bragg case).

(iv) Since the optical radiation pressure (Π_R) is much smaller than the Laplace pressure (Π_L), we neglect droplet deformation. Indeed, $\Pi_\mathrm{R} \sim P/(w_0^2 c) \sim 10^{-2}$ Pa $\ll \Pi_\mathrm{L} \sim \gamma/R \sim 10^3$ Pa, with γ the surface tension of the interface between cholesteric and host fluid, and typical droplet radius $R \sim 10$ μm.

(v) We neglect the light absorption by cholesteric droplets, as well as by the host fluid (see subsection 1.3.3 for details).

1.3.2 Elementary optical force

Let us consider a spherical particle of radius R surrounded by a uniform medium of refractive index n_{ext} and illuminated by a beam with intensity distribution I. Interaction of the particle with a single incident ray impinging on the surface element dS at the incidence angle θ_i is sketched in Fig. 1.8.

According to the first principle of mechanics, the light-induced elementary force exerted on dS equals

$$d\mathbf{F}(\theta_i) = \left(\mathbf{p}_{\mathrm{in}} - \mathbf{p}_{\mathrm{out}}^{\mathrm{eff}}\right) \frac{dN}{dt}\,, \tag{1.13}$$

where $\mathbf{p}_{\mathrm{in}}$ is the incident photon linear momentum, whereas $\mathbf{p}_{\mathrm{out}}^{\mathrm{eff}}$ is the corresponding average linear momentum per photon after interaction with the particle, dN is the number of photons hitting dS during dt. Following the definition of the radiation intensity, we rewrite the elementary force as

$$d\mathbf{F}(\theta_i) = \left(\mathbf{p}_{\mathrm{in}} - \mathbf{p}_{\mathrm{out}}^{\mathrm{eff}}\right) \frac{I\cos\theta_i\, dS}{\hbar\omega} = \mathbf{f}(\theta_i)\frac{n_{\mathrm{ext}}}{\mathrm{c}} I\cos\theta_i\, dS \tag{1.14}$$

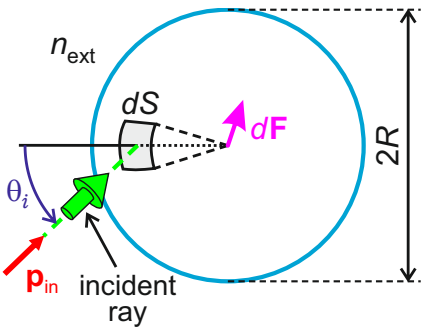

Figure 1.8: *A spherical particle illuminated by a geometrical ray. The light falling on the surface element dS at the incidence angle θ_i exerts on the particle the elementary optical force $d\mathbf{F}$.*

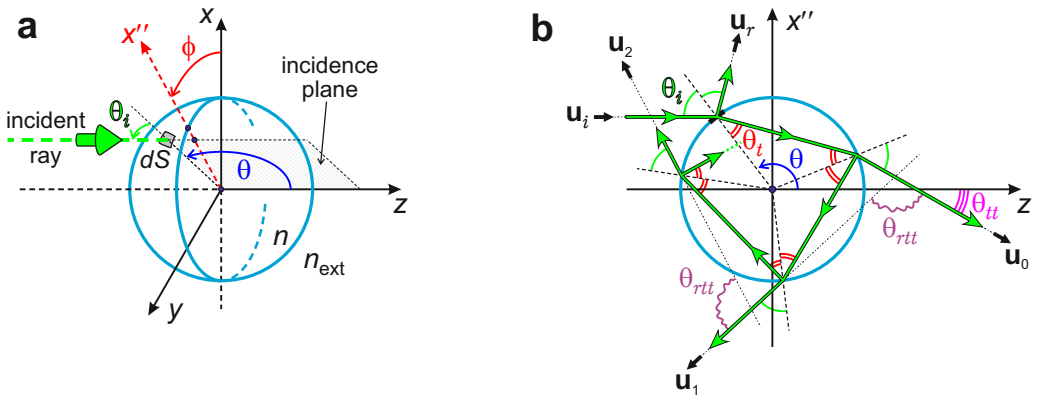

Figure 1.9: (**a**) *Coordinate systems introduced for the analysis of an incident ray after impinging a surface element dS of a spherical particle.* (**b**) *Ray-tracing in the incidence plane.*

with ω the angular frequency of light, $\mathbf{f}(\theta_i) = (\mathbf{p}_{\text{in}} - \mathbf{p}_{\text{out}})/|\mathbf{p}_{\text{in}}|$ the dimensionless vector expressing the relative change of the photon linear momentum due to interaction with the particle, which leads to the redistribution of the incident light into the reflected and scattered parts.

Aiming for a detailed consideration of the mechanical effect caused by reflection and scattering from the particle, we introduce the orthonormal Cartesian coordinate system (x, y, z) originating at the particle center and having the axis z parallel to the incident ray, and the spherical coordinate system with the same origin as (x, y, z) and the polar and azimuthal angles θ and ϕ, as shown in Fig. 1.9a. Since θ is defined from the axis z, the incidence angle θ_i in Fig. 1.8 and Fig. 1.9a corresponds to $\theta_i = \pi - \theta$, hence $\cos\theta_i = -\cos\theta$. Since the surface element equals $dS = R^2 \sin\theta d\theta d\phi$, the elementary force (Eq. (1.14)) is eventually written as

$$d\mathbf{F}(\theta,\phi) = -\mathbf{f}(\theta)\frac{n_{\text{ext}}R^2}{\text{c}} I(\theta,\phi)\cos\theta\,\sin\theta\,d\theta d\phi\,. \tag{1.15}$$

According to the law of conservation of energy, once the ray impinges on the particle, its effective radiation power $P_i = |I(\theta,\phi)\cos\theta\,dS(\theta,\phi)|$ becomes apportioned between the reflected ray of power $\mathcal{R}_i P_i$ and an infinite series of scattered rays of power $\mathcal{T}_i\mathcal{T}_0 P_i$, $\mathcal{T}_i\mathcal{R}_1\mathcal{T}_1 P_i$, $\mathcal{T}_i\mathcal{R}_1\mathcal{R}_2\mathcal{T}_2 P_i$, ... , where $\mathcal{R}_i$ and $\mathcal{T}_i = 1-\mathcal{R}_i$ are the reflectance and transmittance of the droplet interface at the point of the ray incidence, $\mathcal{T}_{\alpha=0,1,2,\ldots}$ are the interface transmittances for the ray leaving the droplet after α internal reflections, $\mathcal{R}_{1,2,\ldots}$ are the reflectances for the successive internal reflections. Using the notations introduced in Fig. 1.9b, we express the vector $\mathbf{f}$ as follows

$$\mathbf{f}(\theta) = \mathbf{u}_i(\theta) - \mathcal{R}_i(\theta)\mathbf{u}_r(\theta) - \mathcal{T}_i(\theta)\sum_{\alpha=0}^{\infty}\mathcal{T}_\alpha(\theta)\prod_{\beta=0}^{\alpha}\mathcal{R}_\beta(\theta)\,\mathbf{u}_\alpha(\theta)\,, \tag{1.16}$$

where $\mathbf{u}_i$, $\mathbf{u}_r$, $\mathbf{u}_0$ and $\mathbf{u}_\alpha$ are the unit vectors pointing along the incident (index "i"), reflected ("r") and the successive scattered rays, respectively, with $\mathcal{R}_{\beta=0} = 1$ by construction.

In this thesis we are dealing with circularly polarized light, for which, according to Fresnel's formulae [11], the reflectance associated with the incident hitting point is

$$\mathcal{R}_i(\theta) = \left[\mathcal{R}_{i,\parallel}(\theta) + \mathcal{R}_{i,\perp}(\theta)\right]/2\,, \tag{1.17}$$

where

$$\mathcal{R}_{i,\parallel}(\theta) = \left[\frac{\tan(\theta-\theta_t)}{\tan(\theta+\theta_t)}\right]^2 \quad \text{and} \quad \mathcal{R}_{i,\perp}(\theta) = \left[\frac{\sin(\theta-\theta_t)}{\sin(\theta+\theta_t)}\right]^2 \tag{1.18}$$

are reflectances for the plane waves polarized parallel and perpendicular to the incidence plane, $\theta_t = \mathrm{sgn}(\cos(\theta))\,\arcsin[(n_{\mathrm{ext}}/n)\sin\theta]$ is the angle of refraction with "sgn" the sign function. In general, the reflectances $\mathcal{R}_\beta$ differ from $\mathcal{R}_i$, since the polarization of light changes every time it meets the interface. However, this difference is usually neglected [5] when modeling optical radiation forces on transparent scattering spheres [27, 28, 29].

From these considerations, Eq. (1.16) reduces to

$$\mathbf{f}(\theta) = \mathbf{u}_i(\theta) - \mathcal{R}_i(\theta)\mathbf{u}_r(\theta) - \left[\mathcal{T}_i(\theta)\right]^2 \sum_{\alpha=0}^{\infty} \left[\mathcal{R}_i(\theta)\right]^\alpha \mathbf{u}_\alpha(\theta)\,. \tag{1.19}$$

Accounting for

$$\mathbf{f}(\theta) = f_\perp(\theta)\,\mathbf{x}'' + f_\parallel(\theta)\,\mathbf{z} \tag{1.20}$$

with

$$\mathbf{x}'' = \cos\phi\,\mathbf{x} + \sin\phi\,\mathbf{y} \tag{1.21}$$

and following the ray-tracing sketched in Fig. 1.9b, we write the axial (i. e. parallel to $\mathbf{z}$ and denoted by $f_\parallel$) and transverse (i. e. parallel to $\mathbf{x}''$ and denoted by $f_\perp$) components of $\mathbf{f}(\theta)$ as follows:

$$f_\parallel(\theta) = 1 + \mathcal{R}_i(\theta)\cos 2\theta - \left[\mathcal{T}_i(\theta)\right]^2 \sum_{\alpha=0}^{\infty} \left[\mathcal{R}_i(\theta)\right]^\alpha \cos(\theta_{tt} + \alpha\theta_{rtt})\,, \tag{1.22}$$

$$f_\perp(\theta) = \mathcal{R}_i(\theta)\sin 2\theta - \left[\mathcal{T}_i(\theta)\right]^2 \sum_{\alpha=0}^{\infty} \left[\mathcal{R}_i(\theta)\right]^\alpha \sin(\theta_{tt} + \alpha\theta_{rtt})\,, \tag{1.23}$$

where the angles $\theta_{tt} = 2(\pi - \theta - \theta_t)$ and $\theta_{rtt} = \pi - 2\theta_t$ indicate the ray propagation directions after interaction with the droplet interface (see Fig. 1.9b).

[5] In the context of this work, accounting for the projection of the incident polarization state to the local incidence frame would be an irrelevant refinement recalling the crude approximation that a cholesteric droplet in the non-Bragg regime is considered as an optically isotropic dielectric sphere of refractive index n (assumption (iii)).

G. Roosen and C. Imbert [27] have shown that the sums of the mixed series in Eqs. (1.22), (1.23) can be simplified by means of the Euler's formula $\exp(iq) = \cos q + i \sin q$ valid for any real q. Application of this method to our framework gives

$$f_{\parallel}(\theta) = 1 + \mathcal{R}_i(\theta)\cos 2\theta - \left[\mathcal{T}_i(\theta)\right]^2 \frac{\cos(2\theta - 2\theta_t) + \mathcal{R}_i(\theta)\cos 2\theta}{1 + \left[\mathcal{R}_i(\theta)\right]^2 + 2\mathcal{R}_i(\theta)\cos 2\theta_t}, \tag{1.24}$$

$$f_{\perp}(\theta) = \mathcal{R}_i(\theta)\sin 2\theta - \left[\mathcal{T}_i(\theta)\right]^2 \frac{\sin(2\theta - 2\theta_t) + \mathcal{R}_i(\theta)\sin 2\theta}{1 + \left[\mathcal{R}_i(\theta)\right]^2 + 2\mathcal{R}_i(\theta)\cos 2\theta_t}. \tag{1.25}$$

We eventually rewrite Eq. (1.15) for the elementary optical radiation force as follows

$$d\mathbf{F}(\theta,\phi) = -\frac{n_{\text{ext}}R^2}{2\text{c}} I(\theta,\phi)\Big[f_{\perp}(\theta)(\cos\phi\,\mathbf{x} + \sin\phi\,\mathbf{y}) + f_{\parallel}(\theta)\,\mathbf{z}\Big]\sin 2\theta\, d\theta d\phi\,. \tag{1.26}$$

If the conditions required for the circular Bragg reflection are met (see the assumption (iii)), then $\mathcal{R}_i(\theta) = 1$ and the above expression simplifies to

$$\begin{aligned} d\mathbf{F}^{\text{Bragg ray}}(\theta,\phi) &= \frac{n_{\text{ext}}R^2}{2\text{c}} I(\theta,\phi) \\ &\times \Big[\sin 2\theta(\cos\phi\,\mathbf{x} + \sin\phi\,\mathbf{y}) + (1 + \cos 2\theta)\,\mathbf{z}\Big]\sin 2\theta\, d\theta d\phi\,. \end{aligned} \tag{1.27}$$

In the next chapters the net optical radiation force is obtained by integrating the elementary force over the illuminated area of the droplet, accounting for the ray-tracing regime (namely, we use Eq. (1.27) in the Bragg case, and Eq. (1.26) otherwise) and the appropriate intensity distribution.

1.3.3 Absorption issue

As could be seen from Fig. 1.9b, the incident ray covers the distance $2R\cos\theta_t$ inside the particle till the first internal reflection. If now we take the absorption into account, the transmitted power should be reduced by the factor $A = \exp(-2aR\cos\theta_t)$ with a the absorption coefficient of the particle material. Since the particle is spherical, the output light experiencing $\alpha = 0, 1, 2, \ldots$ internal reflections is attenuated by a factor $A^{\alpha+1}$. Implementing the absorption induced attenuation into Eq. (1.19), we get in presence of absorption:

$$\mathbf{f}_{\text{a}}(\theta) = \mathbf{u}_i(\theta) - \mathcal{R}_i(\theta)\mathbf{u}_r(\theta) - \left[\mathcal{T}_i(\theta)\right]^2 A \sum_{\alpha=0}^{\infty} \left[\mathcal{R}_i(\theta)\,A\right]^{\alpha} \mathbf{u}_{\alpha}(\theta)\,. \tag{1.28}$$

The previously applied method for the series simplification gives the following expressions for the axial and transverse components of $\mathbf{f}_{\text{a}}(\theta)$:

$$f_{\parallel,\text{a}}(\theta) = 1 + \mathcal{R}_i(\theta)\cos 2\theta - \left[\mathcal{T}_i(\theta)\right]^2 A \frac{\cos(2\theta - 2\theta_t) + \mathcal{R}_i(\theta)\,A\cos 2\theta}{1 + \left[\mathcal{R}_i(\theta)\,A\right]^2 + 2\mathcal{R}_i(\theta)\,A\cos 2\theta_t}, \tag{1.29}$$

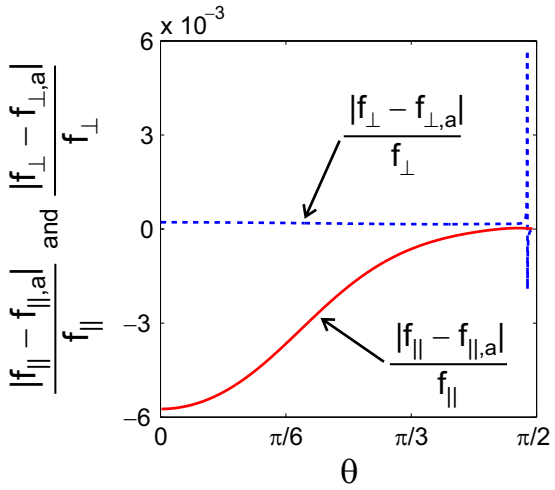

Figure 1.10: *Calculated relative contributions of absorption into the photon linear momentum changes for axial and transverse components of* $\mathbf{f}(\theta)$.

$$f_{\perp,\mathrm{a}}(\theta) = \mathcal{R}_i(\theta)\sin 2\theta - \left[\mathcal{T}_i(\theta)\right]^2 A\,\frac{\sin(2\theta - 2\theta_t) + \mathcal{R}_i(\theta)\,A\sin 2\theta}{1 + \left[\mathcal{R}_i(\theta)\,A\right]^2 + 2\mathcal{R}_i(\theta)\,A\cos 2\theta_t}\,. \qquad (1.30)$$

The cholesteric material under study has typical absorption coefficient $a \lesssim 10\ \mathrm{m}^{-1}$ [30]. With the typical parameters of the light-matter system (namely, $R = 10\,\mu$m, $n = 1.6$ and $n_{\mathrm{ext}} = 1.367$ for a host fluid represented by 27 wt. % aqueous glycerol solution [31]), calculated relative contributions of absorption into the linear momentum changes, $|f_\parallel - f_{\parallel,\mathrm{a}}|/f_\parallel$ and $|f_\perp - f_{\perp,\mathrm{a}}|/f_\perp$ (using Eqs. (1.24), (1.25), (1.29), (1.30)), do not exceed 0.6 % for all θ (see Fig. 1.10), and thus are safely neglected in this work.

Another important issue is the absorption of light by the host fluid. As shown in section 1.2.1 of [32], the absorption-induced bulk flow has a typical velocity $v_{\mathrm{fluid}} \sim a_{\mathrm{fluid}}P/(\eta c)$, where a_{fluid} and η are the absorption coefficient and the dynamic viscosity of the host fluid, respectively. In our case the host fluid is a aqueous glycerol solution, which has the absorption coefficient between that of pure water ($a_{\mathrm{water}} \approx 0.035\ \mathrm{m}^{-1}$ at 25°C and 532 nm wavelength [33]) and pure glycerol (roughly 35 % larger than a_{water} [34]), therefore $v_{\mathrm{fluid}} \sim 0.1\ \mu\mathrm{m\ s}^{-1}\ \mathrm{W}^{-1}$. When the light-driven velocity of cholesteric droplets (see next subsection) is sufficiently larger than v_{fluid}, the absorption-induced bulk flows can therefore be neglected. Noticeably, two-beam schemes applied in the projects reported in the next three chapters are formally free from bulk flow, since the effects of the counterpropagating coaxial beams of equal power on the host fluid are mutually compensated.

1.3.4 Light-induced velocity

Optical radiation force **F** exerted by a laser beam on a cholesteric droplet sets it into a motion with respect to the surrounding viscous fluid assumed to be initially at rest. In general, such a viscous dynamics is described by the Navier-Stokes equations [35]. Since we deal with a spherical droplet of radius $R \sim 10\,\mu$m and viscosity $\eta_d \sim 30$ mPa s at room temperature [36, 37, 38] moving at the light-induced velocity $v \lesssim 1$ mm s^{-1} in the host fluid of viscosity $\eta = 2$ mPa s [39] and density $\rho = 1.065\,\mathrm{g\,cm^{-3}}$ equal to that of the droplet, the Reynolds number that characterizes the flow around the droplet is

$$\mathrm{Re} = \frac{2R\rho v}{\eta} \lesssim 10^{-2} \ll 1\,. \tag{1.31}$$

This means that viscous forces acting on the droplet are much more important than inertial forces in the investigated system, and thus the relationship between the viscous force F_{visc} exerted on the droplet and the corresponding speed of motion v is given by the Stokes' law [40]

$$\mathbf{F}_{\mathrm{visc}} = \frac{2 + 3\eta_d/\eta}{1 + \eta_d/\eta}\, 2\pi\eta R\mathbf{v}\,. \tag{1.32}$$

In our case, we thus get to a good approximation

$$\mathbf{F}_{\mathrm{visc}} \simeq 6\pi\eta R\mathbf{v}\,. \tag{1.33}$$

Considering an isodense solution (which is used in the next chapters, except for the last one, where gravity is at work) the third principle of mechanics implies that the optical radiation force on a droplet, **F**, is balanced by the viscous force, $\mathbf{F}_{\mathrm{visc}}$. Therefore, the light-induced linear velocity of the droplet equals

$$\mathbf{v} = \frac{1}{6\pi\eta R}\,\mathbf{F}\,. \tag{1.34}$$

Since optical forces are typically in order of piconewtons, Eq. (1.34) gives an expected velocity of the order of $10\,\mu$m s^{-1}, the Reynolds number associated with the optically displaced droplet thus fully justifies the use of the Stokes' law.

CHAPTER 2

Helicity-controlled optical radiation force

In this chapter we report on helicity-dependent optical force exerted on chiral particles. The phenomenon is quantitatively retrieved experimentally and successfully compared with simulations performed by means of our model. First, general features of the experimental approach and some basic qualitative predictions are presented in section 2.1. The details of the optical set-up and the experimental proof-of-principle using laser-driven radial cholesteric droplets are then given in section 2.2. Next, in section 2.3 we derive the theoretical expressions for the light-induced velocities of the droplets. These results are then used for a quantitative description of the measurements, which allows for the in situ estimation of a key material parameter – the Bragg angle. Section 2.4 then presents a method to achieve the full helicity control of the light-induced displacement of a chiral particle, whereas its quantitative study is set forth in section 2.5.

2.1 Principle of the study

Our approach to the control of optical radiation forces via the photon helicity is outlined in Fig. 2.1. Let us consider a particle with chirality $\chi = \pm 1$ illuminated by a circularly polarized plane wave with helicity $+\Lambda$ or $-\Lambda$, as respectively sketched in panels (a) and (b). Recent theoretical studies have predicted that optomechanical properties of chiral matter depend on helicity of the incident light [41, 21, 22]. Therefore, in general, the optical radiation forces exerted on the considered chiral particle by light with $+\Lambda$ or $-\Lambda$ are expected to be unequal, i. e. $\mathbf{F}_{+\Lambda} \neq \mathbf{F}_{-\Lambda}$. This formally allows one to change the light-driven velocity of the particle between $\mathbf{v}_{+\Lambda} \sim \mathbf{F}_{+\Lambda}$ and $\mathbf{v}_{-\Lambda} \sim \mathbf{F}_{-\Lambda}$ by controlling the photon helicity.

The experimental framework to implement the above ideas is presented in Fig. 2.1(c). A radial cholesteric droplet of radius R is immersed in a fluid with refractive index n_{ext} and located on the axis of a circularly polarized Gaussian beam having waist radius $w_0 \gg R$ (in practice, our experiments have been carried out in the range $10 < w_0/R < 80$) and wavevector $\mathbf{k}$ that defines z the axis. From Eq. (1.12) with $\ell = 0$ and accounting for $w(z) = w_0$ (since the Rayleigh range $z_{\text{R}} = \pi w_0^2/\lambda_0 \gg R$), the light intensity on the droplet could be considered as a

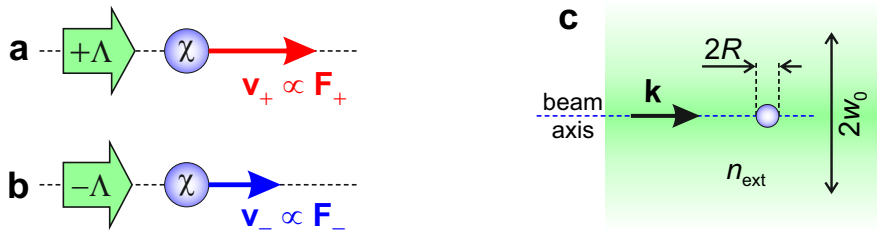

Figure 2.1: (**a**, **b**) *The concept of helicity-controlled optical force. A plane wave with helicity* $\pm\Lambda$ *exerts on a particle with chirality* χ *the force* $\mathbf{F}_{\pm\Lambda}$*. In general, the forces for opposite helicities are unequal, as well as the corresponding light-induced velocities of the particle.* (**c**) *Scheme of the experimental situation where* $w_0 \gg R$*.*

constant that corresponds to the maximum intensity I_0 of the Gaussian beam. Namely,

$$I_0 = \frac{2P}{\pi w_0^2}\,. \tag{2.1}$$

The above approximation is used in this chapter when comparing experimental data to the predictions of our model. The assumed axial symmetry of the "beam + droplet" system implies the absence of transverse optical forces on the droplet. Therefore we expect the illuminated droplet to move along the z axis at a constant linear velocity. Since the elementary force scales as $R^2 I/\mathrm{c}$, see Eqs. (1.26), (1.27), whereas the drag force is proportional to $\eta R v$ (see Eq. (1.33)), the velocity scales (up to a dimensionless constant that will be determined in section 2.5) as

$$\mathbf{v}_\pm \propto \frac{PR}{\mathrm{c}\eta w_0^2}\,\mathbf{z}\,. \tag{2.2}$$

2.2 Experimental demonstration

The experimental the experimental set-up is outlined in Fig 2.2. A collimated circularly-polarized Gaussian-like laser beam with waist radius $w_0 = 505$ μm, vacuum wavelength $\lambda_0 = 532$ nm and helicity $\pm\Lambda$ propagates at normal incidence through a rectangular quartz cell (from Hellma Analytics), as sketched in panel (a). The cell contains radial droplets of the cholesteric liquid crystal MDA-02-3211 (see sections 1.1, 1.1.2 for details) immersed in a host fluid chosen as a ≈ 25.2 wt. % aqueous glycerol solution with refractive index $n_{\mathrm{ext}} \approx 1.365$ and dynamic viscosity $\eta \approx 2$ mPa s. A cholesteric droplet with radius $R \ll w_0$ is centered on the beam axis z by displacing the cell using a translational stage. Geometry of the experimental sample is shown schematically in panels (b, c). White light (labeled as "WL" on panel (a) from a halogen source OSL1-EC (Thorlabs,

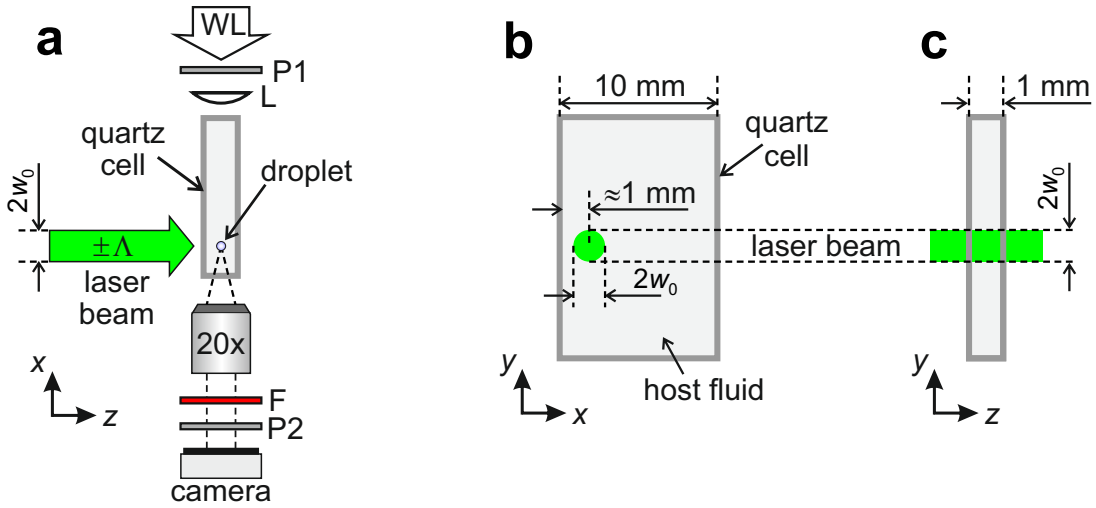

Figure 2.2: *(**a**) Sketch of the experimental setup. Bragg- or anti-Bragg polarized laser beam illuminates a radial cholesteric droplet immersed in a host fluid inside a quartz cell. Elements of the imaging system: white light (WL) source, convex lens (L), microscope objective, CMOS camera, red filter (F) and (optional) crossed linear polarizers (P1, P2). (**b**, **c**) Schematic side views of the sample.*

Inc.) illuminates the droplet through a convex lens L with 35 mm focal length. Imaging of the droplet motion is performed by means of a microscope objective (Olympus SLMPLN, magnification ×20, numerical aperture NA = 0.25) and a CMOS camera (DCC1645C from Thorlabs) through a red filter F, which absorbs the green laser illumination scattered by the sample towards the camera. The crossed linear polarizers P1 and P2 are used when checking the radial symmetry of the droplet supramolecular organization.

A typical experimental result for the scheme described above is summarized in Fig. 2.3. Without laser illumination, the droplet is at rest. When the laser is turned on, the droplet almost immediately starts moving along the beam propagation direction at a constant velocity. When the laser is turned off, the droplet motion almost instantly stops since viscous forces overcome the inertial ones (see subsection 1.3.4). The droplet velocities corresponding to the Bragg and anti-Bragg polarization states of the laser beam are respectively labeled as v_{B} and v_{AB}. As can be seen from panel (a), the Bragg droplet velocity is a few times larger than the anti-Bragg one. This demonstrates experimentally the proposed concept of the helicity-controlled optical radiation force. Using this approach, one can switch the velocity of a chiral droplet between two different values, thus achieving a partial control of the light-induced motion.

Noteworthy, the radial structure of the droplet is unaltered during its displacement, as demonstrated by the optical transmission image sequences at the early, intermediate and final stages of its laser-induced motion in the Bragg case,

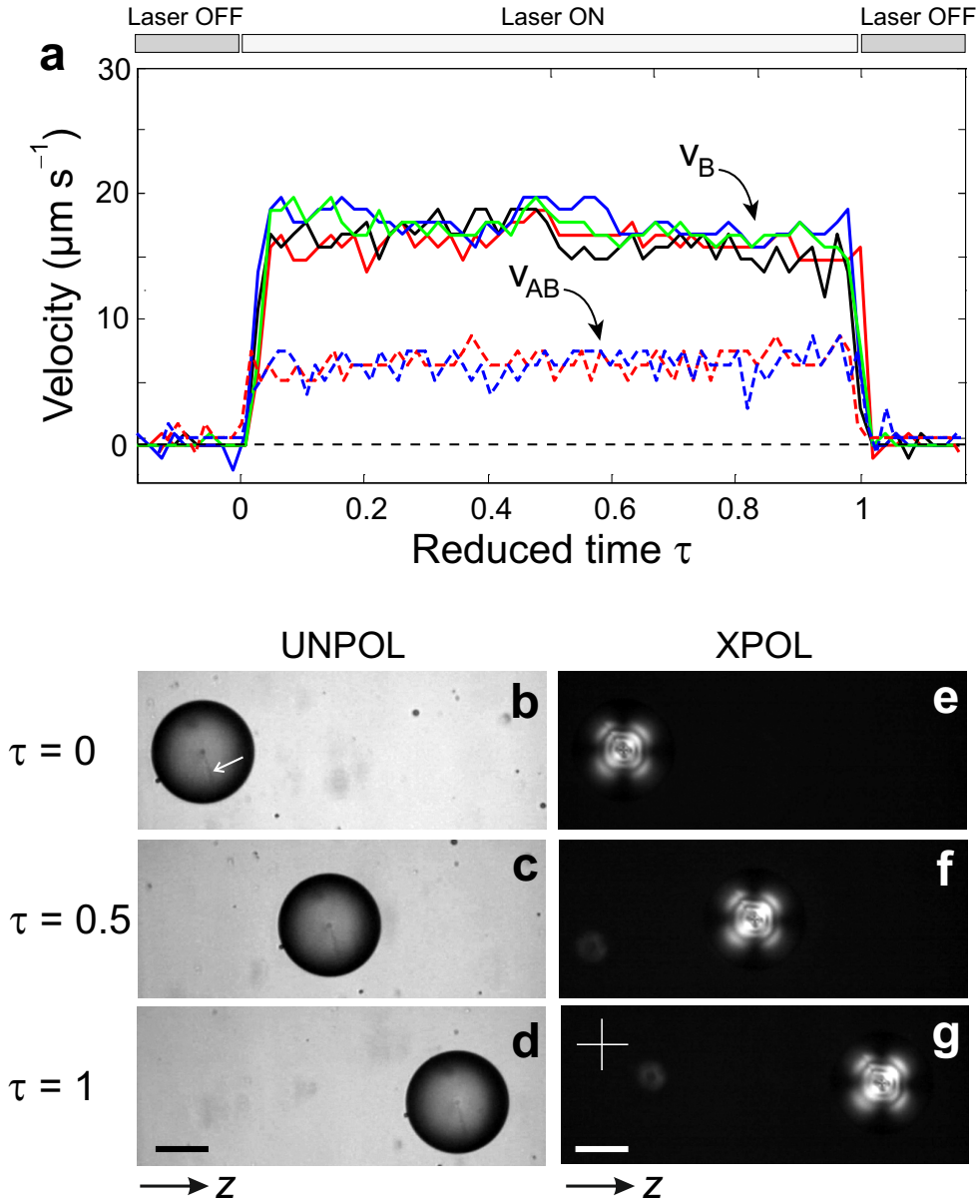

Figure 2.3: (**a**) *Droplet velocity as a function of reduced time* $\tau = (t - t_{on})/(t_{off} - t_{on})$ *for Bragg* (v_B, *solid curves) and anti-Bragg* (v_{AB}, *dashed curves) laser beam illumination conditions, where* t_{on} *and* t_{off} *refer to switch on and off times of the laser beam, respectively. Different curves refer to independent experiments performed at power* $P = 0.97$ *W, waist* $w_0 = 505$ μ*m and the droplet radius* $R \approx 28$ μ*m.* (**b**-**d**) *Direct transmission snapshots of the droplet at* $\tau = 0, 0.5, 1$ *for the Bragg case. White arrow on panel* (**b**) *indicates the characteristic radial defect of the droplet.* (**e**-**g**) *Transmission images (captured at the time set* $\tau = 0, 0.5, 1$) *of the droplet viewed between crossed linear polarizers, whose orientation is indicated on panel* (**g**). *Scale bar is 30* μ*m.*

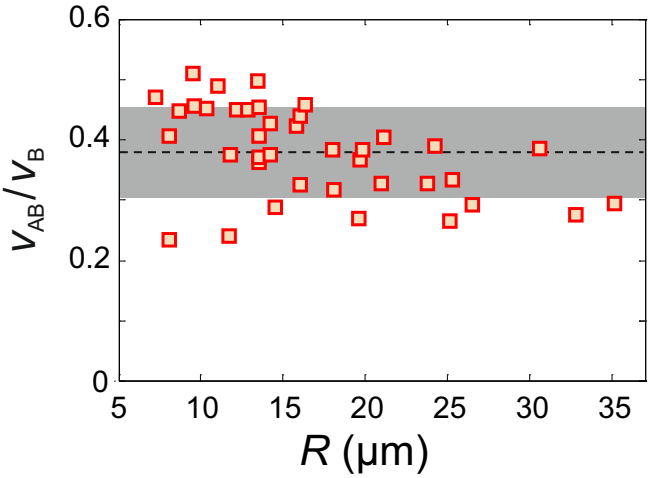

Figure 2.4: *The markers represent the measured droplet velocity ratio* v_{AB}/v_B *as a function of droplet radius* R*. Power of the beam is* $P = 0.78$ *W. Horizontal dashed line refers to the mean value equal to* 0.38*, whereas gray area shows the standard deviation range of* ±0.075.

see Figs. 2.3(b–d) (direct images) and Figs. 2.3(e–g) (taken between crossed polarizers). The radial defect is observed in the former case, see white arrow in Fig. 2.3(b), whereas the unchanged dark cross pattern confirms preservation of radial symmetry within the droplet.

As follows from Eq. (2.2), both velocities v_{AB} and v_B are expected to be proportional to the droplet radius R. Therefore, the ratio v_{AB}/v_B is expected to be independent on the size of the droplet. In order to verify this statement, we have measured the velocity ratio v_{AB}/v_B for 38 distinct droplets with radii ranging from 7 to 35 μm (this is the typical size range obtained with the stirring technique). The obtained dataset is summarized in Fig. 2.4, where the markers show the measured velocity ratio as a function of the droplet radius R. The average value of the experimental points is indicated by the horizontal dashed line, whereas the standard deviation range is shown by the gray area.

2.3 Light-induced forces and velocities

Towards a quantitative analysis of the obtained experimental statistics regarding the velocity ratio v_{AB}/v_B, we model optical radiation forces exerted on a Bragg cholesteric droplet under plane-wave-like illumination using the approach presented in section 1.3. We apply the coordinate systems introduced in Fig. 1.9, assuming every incident ray parallel to the z axis, hence θ ranging from $\pi/2$ to π.

In the Bragg case, a ray impinging on the droplet surface within the Bragg cone (i. e. at $0 \leq \pi - \theta \leq \theta_{B,ext}$) exerts the elementary force given by Eq. (1.27).

Since the light intensity is considered to be a constant (see Eq. (2.1)), the elementary optical radiation force becomes

$$\begin{aligned} d\mathbf{F}^{\text{Bragg ray}}(\theta,\phi) &= -\frac{n_{\text{ext}}PR^2}{\pi c w_0^2} \\ &\times \Big[\sin 2\theta(\cos\phi\,\mathbf{x}+\sin\phi\,\mathbf{y})+(1+\cos 2\theta)\,\mathbf{z}\Big]\sin 2\theta\, d\theta d\phi\,. \end{aligned} \quad (2.3)$$

On the other hand, the elementary force associated with a non-Bragg ray, namely for an incident angle $\theta_{\text{B,ext}} < \pi - \theta \leq \pi/2$ in the Bragg case ($\Lambda\chi = -1$) and any incident angle in the anti-Bragg case ($\Lambda\chi = +1$), is written as

$$\begin{aligned} d\mathbf{F}^{\text{non-Bragg ray}}(\theta,\phi) &= -\frac{n_{\text{ext}}PR^2}{\pi c w_0^2} \\ &\times \Big[f_\perp(\theta)(\cos\phi\,\mathbf{x}+\sin\phi\,\mathbf{y})+f_\parallel(\theta)\,\mathbf{z}\Big]\sin 2\theta\, d\theta d\phi\,. \end{aligned} \quad (2.4)$$

The net force exerted on the droplet is then obtained by integrating the elementary force over the illuminated surface of the droplet. Noteworthy, the transverse (i. e. perpendicular to the z axis) components of the net optical force vanishes due to the axial symmetry of the light-matter system, which formally comes from the fact that $\int_0^{2\pi}\sin\phi\,d\phi = \int_0^{2\pi}\cos\phi\,d\phi = 0$. For the Bragg case (labeled as "B"), the axial component of the net optical force is written as

$$F_z^{\text{B}} = \int_{\pi/2}^{\pi-\theta_{\text{B,ext}}} \mathbf{z}\cdot d\mathbf{F}^{\text{non-Bragg ray}} + \int_{\pi-\theta_{\text{B,ext}}}^{\pi} \mathbf{z} d\mathbf{F}^{\text{Bragg ray}}\,, \quad (2.5)$$

whereas for the anti-Bragg case (labeled as "AB") one has

$$F_z^{\text{AB}} = \int_{\pi/2}^{\pi} \mathbf{z}\cdot d\mathbf{F}^{\text{non-Bragg ray}}\,. \quad (2.6)$$

After calculations one gets

$$F_{\text{B}} = \frac{2n_{\text{ext}}PR^2}{c w_0^2}\left[1-\cos^4\theta_{\text{B,ext}} - \int_{\pi/2}^{\pi-\theta_{\text{B,ext}}} \sin 2\theta f_\parallel(\theta) d\theta\right], \quad (2.7)$$

$$F_{\text{AB}} = -\frac{2n_{\text{ext}}PR^2}{c w_0^2}\int_{\pi/2}^{\pi} \sin 2\theta f_\parallel(\theta) d\theta\,. \quad (2.8)$$

Substituting F_{B} and F_{AB} into Eq. (1.34),v_{B} and v_{AB} can be obtained, from which we get the velocity ratio

$$\frac{v_{\text{AB}}}{v_{\text{B}}} = \frac{F_{\text{AB}}}{F_{\text{B}}} = \frac{-\int_{\pi/2}^{\pi}\sin 2\theta f_\parallel(\theta)d\theta}{1-\cos^4\theta_{\text{B,ext}} - \int_{\pi/2}^{\pi-\theta_{\text{B,ext}}}\sin 2\theta f_\parallel(\theta)d\theta}\,. \quad (2.9)$$

This quantity is independent of the droplet size, but depends on the material parameters, namely, refractive index of the host fluid (n_{ext}), average refractive index

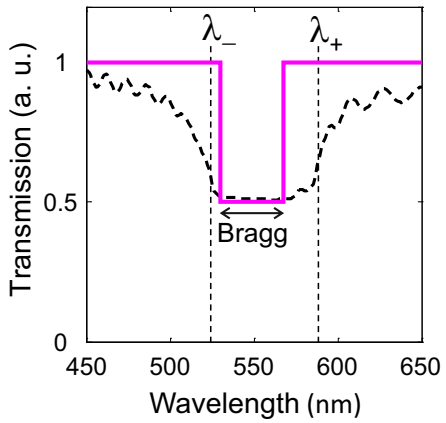

Figure 2.5: *Dashed curve shows the measured unpolarized transmission spectrum of a planar film of the applied cholesteric MDA-02-3211 (same plot as in Fig. 1.2(b)). Solid line represents our theoretical approach to the Bragg and non-Bragg behavior of this material.*

of the cholesteric (n) and its intrinsic Bragg cone angle (θ_B), which appear in Eqs. (1.6), (1.24). Using the known refractive indices and the measured average velocity ratio (see the caption of Fig. 2.4), and taking the intrinsic Bragg angle as the only adjustable parameter, we find $\theta_B = 15.3°(+3.1°/-2.3°)$. This value is smaller than the ones obtained from the spectroscopic and direct microscopic measurements reported in section 1.1.2. However, this is actually expected recalling that our model assumes an ideal rectangular bandgap, which is illustrated in Fig. 2.5, where the modeled transmission spectrum is depicted.

We thus conclude to a fair theoretical description of our observations, thereby validating that: (1) the physical picture is properly grasped and (2) the unavoidable scattering of light by the droplet prevents the full control of the optical radiation pressure by the photon helicity.

2.4 Full control by helicity: two-beam strategy

Aiming to the full control of the light-induced velocity of a Bragg cholesteric droplet, one has to get rid of the unwanted non-Bragg rays. To this purpose, we implement the scheme presented in Fig. 2.6(a,b). The idea is to use two coaxial, collimated, circularly polarized and counterpropagating beams with equal power and waist, one being either Bragg- or anti-Bragg-polarized (helicity Λ_B or Λ_{AB}), whereas the other is anti-Bragg polarized (helicity Λ_{AB}).

When both beams are anti-Bragg (see Fig. 2.6(a)), their individual contribu-

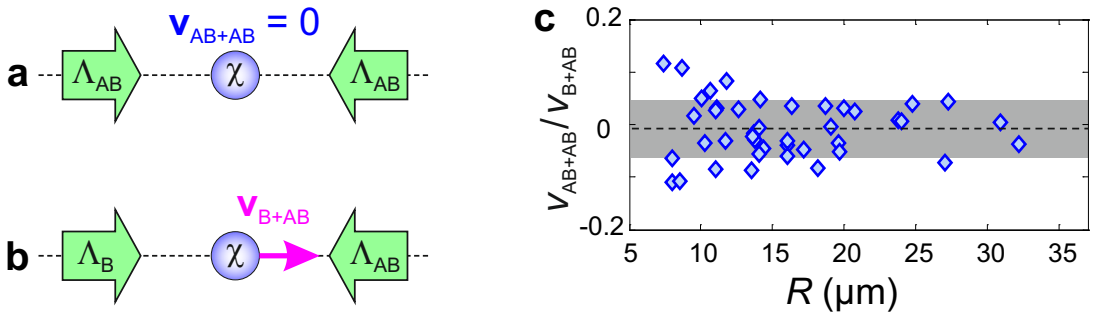

Figure 2.6: *Full control of the light-induced droplet velocity shall be achieved by means of two counterpropagating beams with identical intensity profiles and independently switchable helicities. As in Fig. 2.1(a,b), here* $\Lambda_B\chi = -1$ *and* $\Lambda_{AB}\chi = +1$. *(**a**) If both beams are anti-Bragg, optical forces are mutually compensated and the droplet stays at rest, i. e. the light induced velocity* $v_{AB+AB} = 0$. *(**b**) When one of the beams is Bragg-polarized, the optical force it exerts wins and thus the droplet gains a generally non-zero velocity* v_{B+AB}. *(**c**) Measured velocity ratio* v_{AB+AB}/v_{B+AB} *as a function of droplet radius* R *in the two-beam experiment. Power of each beam is* $P = 0.78$ *W. Dashed line and gray area refer to the mean value and the standard deviation range.*

tions to the net optical force perfectly cancel each other. Indeed, in that case

$$F_{AB+AB} = -\frac{2n_{ext}PR^2}{cw_0^2}\left[\int_{\pi/2}^{\pi}\sin 2\theta f_{\parallel}(\theta)d\theta + \int_0^{\pi/2}\sin 2\theta f_{\parallel}(\theta)d\theta\right] = 0\,. \qquad (2.10)$$

On the other hand, when one beam is Bragg-polarized (see Fig. 2.6(b)), one gets

$$\begin{aligned} F_{B+AB} &= \frac{2n_{ext}PR^2}{cw_0^2}\left[1-\cos^4\theta_{B,ext} - \int_{\pi/2}^{\pi-\theta_{B,ext}}\sin 2\theta f_{\parallel}(\theta)d\theta - \int_0^{\pi/2}\sin 2\theta f_{\parallel}(\theta)d\theta\right] \\ &= \frac{2n_{ext}PR^2}{cw_0^2}\left[1-\cos^4\theta_{B,ext} - \int_0^{\theta_{B,ext}}\sin 2\theta f_{\parallel}(\theta)d\theta\right], \qquad (2.11) \end{aligned}$$

which is non-zero if $\theta_{B,ext} \neq 0$.

The proposed two-beam strategy is experimentally implemented by using the same setup as in Fig. 2.2, but adding a second beam. The two counterpropagating beams are aligned by means of a pair of pin-holes. Equality of the beam waists is ensured by identical beam paths, provided by a couple of mirrors. Circular polarization state of one beam is controlled by using two preset quarter-wave plates placed on flip mounts.

The experimental results obtained for 41 distinct droplets are presented in Fig. 2.6(c), where the markers show the measured velocity ratio as a function of the droplet radius R. The dashed line indicates the mean velocity ratio equal

to -0.008 ± 0.055, the standard deviation range being colored in gray. This successfully demonstrates the availability of the full control of optical radiation forces by the photon helicity.

2.5 Quantitative analysis under the two-beam strategy

Let us consider the light-induced velocity $v_{\mathrm{B+AB}}$ in more details. The net optical force given by Eq. (2.11) contains two terms, namely:

- $-\frac{2n_{\mathrm{ext}}PR^2}{cw_0^2}\left[\int_0^{\theta_{\mathrm{B,ext}}} \sin 2\theta f_{\parallel}(\theta)d\theta\right]$, caused by non-Bragg rays falling into the angular range $0 \le \theta < \theta_{\mathrm{B,ext}}$;
- $\frac{2n_{\mathrm{ext}}PR^2}{cw_0^2}\left[1-\cos^4\theta_{\mathrm{B,ext}}\right]$, which refers to the contribution of Bragg rays.

The ratio between these two terms expresses as

$$\epsilon = \frac{\int_0^{\theta_{\mathrm{B,ext}}} \sin 2\theta f_{\parallel}(\theta)d\theta}{1-\cos^4\theta_{\mathrm{B,ext}}} \tag{2.12}$$

and depends on n, n_{ext} and $\theta_{\mathrm{B,ext}}$. Using the actual values for the refractive indices, ϵ is calculated for $0 < \theta_{\mathrm{B,ext}} < \pi/2$, see Fig. 2.7. As one can see from this plot, the fact that $\theta_{\mathrm{B,ext}} < 30^\circ$ in practice allows to neglect, within an error less than 2 %, the contribution of the non-Bragg rays to the net optical force exerted on a Bragg cholesteric droplet in the two-beam scheme.

Hence, Eq. (2.11) can be simplified to

$$F_{\mathrm{B+AB}} \simeq \frac{2n_{\mathrm{ext}}PR^2\left(1-\cos^4\theta_{\mathrm{B,ext}}\right)}{cw_0^2}\,, \tag{2.13}$$

that gives

$$v_{\mathrm{B+AB}} \simeq \frac{n_{\mathrm{ext}}PR\left(1-\cos^4\theta_{\mathrm{B,ext}}\right)}{3\pi\eta cw_0^2}\,. \tag{2.14}$$

In order to verify this theoretical prediction, we have measured the light-induced velocities of five droplets with radii 10.6, 15.0, 17.7, 28.7 and 35.8 μm in the two-beam scheme with the power up to 1.4 W in each beam. The results are summarized in Fig. 2.8, where the markers show the measured droplet velocity $v_{\mathrm{B+AB}}$ divided by the corresponding radius R. The quantity $v_{\mathrm{B+AB}}/R$ is measured in s^{-1} and thus can be interpreted as the inverse characteristic time associated with the droplet motion.

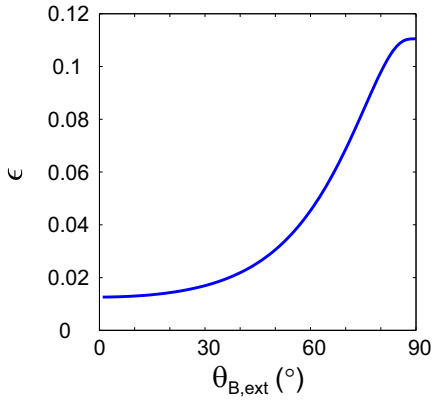

Figure 2.7: *Calculated ratio between the contributions of non-Bragg and Bragg rays to the net optical force exerted on a Bragg cholesteric droplet in the two-beam scheme, versus the extrinsic Bragg cone angle of the cholesteric material. The values used for the refractive indices n and n_{ext} are these of the experiment.*

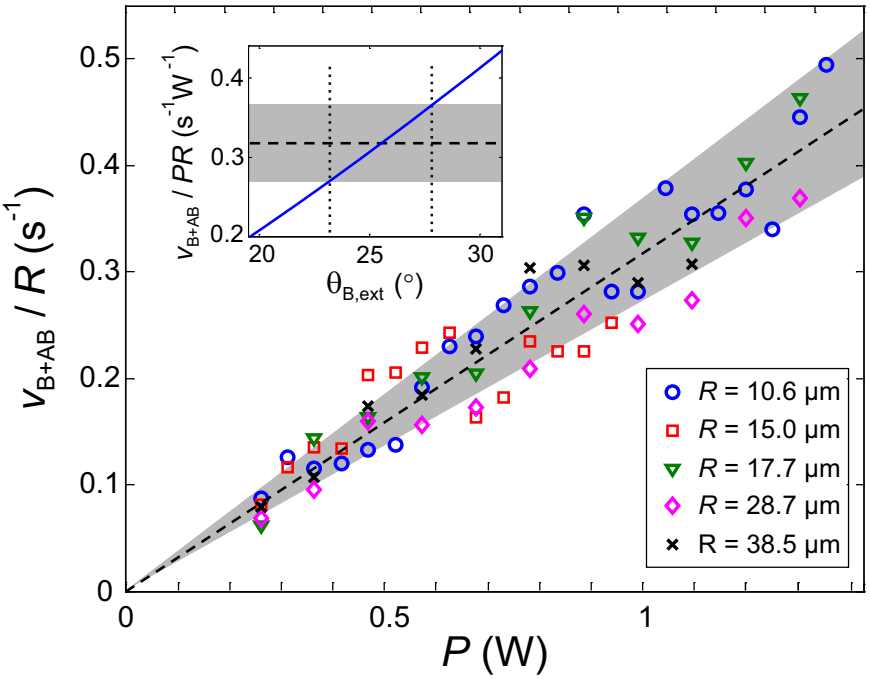

Figure 2.8: *The ratio $v_{\text{B+AB}}/R$ is plotted as a function of total beam power P of one beam for various values of the droplet radius R. Dashed curve refers to the best linear fit. Inset: solid line is the theoretical ratio $v_{\text{B+AB}}/(PR)$ vs. $\theta_{\text{B,ext}}$ whereas dashed line and gray area refer to the mean value and the standard deviation range of the experimental dataset $v_{\text{B+AB}}/(PR)$, respectively. This allows the experimental determination of the precision of θ_{B}, see vertical dotted lines.*

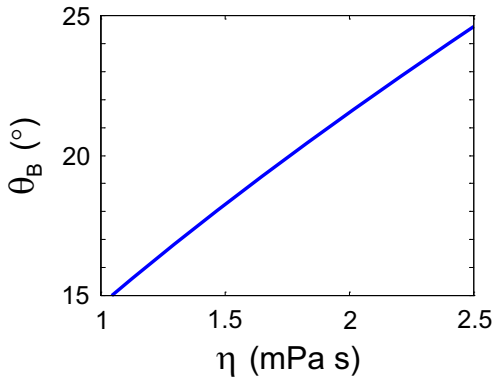

Figure 2.9: *Calculated Bragg angle θ_B obtained by fitting of experimental data shown in Fig. 2.8 using Eq. (2.14) as a function of the dynamical viscosity η of the host fluid, $\theta_{B,ext}$ being the only adjustable parameter.*

As expected from Eq. (2.14), the experimental data lie along a straight line, whose slope is predicted to be $n_{ext}\,(1-\cos^4\theta_{B,ext})\,/\,(3\pi\eta c w_0^2)$. The best linear fit using $\theta_{B,ext}$ as the only adjustable parameter gives $\theta_B = 21.5° \pm 1.9°$, and the result is shown in Fig. 2.8 by the dashed line. The standard deviation range for the experimental data is represented by the gray area determined from the standard deviation range of the dataset for $v_{B+AB}/(PR)$, see inset of Fig. 2.8. The solid curve in this inset figure is the result of simulations with various $\theta_{B,ext}$. The precision of $\theta_{B,ext}$ is given by the range of intersection between the simulated curve and the experimental standard deviation range (see the vertical dotted lines in the inset). The precision for θ_B is derived using Eq. (1.6).

We notice that, regarding the estimation of θ_B, the one-beam scheme (see Eq. (2.9) and Fig. 2.4) is expected to be more precise than the two-beam approach. Indeed, the fitting procedure in the latter case involves additional parameters, namely η and w_0, as follows from Eq. (2.14). The beam waist is measured directly (by means of a CCD Camera Beam Profiler BC106-VIS from Thorlabs, Inc.) whereas the viscosity is taken from tabulated data without measuring it for our actual aqueous glycerol solution and temperature. As shown in Fig. 2.9, in the two-beam experiment, the Bragg angle θ_B calculated from the experimental data exhibits a non-negligible dependence on η. This could explain the difference of 6° between the θ_B values obtained from one-beam and two-beam experiments. We nevertheless conclude that our model gives an overall satisfying description of observations in all explored situations presented in this chapter.

2.6 Outlook

A straightforward anticipated application of the reported helicity-controlled optical radiation forces is the development of chiral optical sorting, which would bring

enhanced functionality to optical chromatography [42] by enabling the photon helicity as a tool for separation of material chirality. This allows us to envision applications for the pharmaceutical industry related to the ability to sort materials with different chiralities. Nanoactuation driven by optical radiation forces [43] is another topic that may benefit from such a polarization control, as discussed in the few dedicated theoretical studies reported so far [21, 41]. Finally, at a larger spatial scale, our findings emphasize the spin angular momentum of light as a possible control parameter for driving solar sails [44].

CHAPTER 3

Optofluidic sorting of material chirality by chiral light

Harnessing material handedness is a topical challenge for many industries since it is a basic requirement towards the synthesis of drugs, additives, or pesticides, to name a few. This implies the development of chiral sorting strategies that correspond to the ability to separate two entities that only differ by their handedness. Established chiral separation techniques at molecular scale are mostly based on the recognition of material chirality by another material that is designed to distinguish between the left- and right-handed versions of the entity to be sorted [45, 46]. Instead, passive approaches free from such chiral recognition may also be considered, for instance by relying on transport phenomena, as discussed in the early 70s [47]. More recently, several options based on the coupling between translational and rotational mechanical degrees of freedom in fluid flows have been proposed [48, 49, 50, 51, 52, 53, 54] and realized down to the micron scale by using various kinds of chiral-shaped microparticles made of non-chiral media [55, 56, 57]. In addition, hydrodynamic propeller effects driven by rotating electric fields have also been considered theoretically [58, 59]. This principle has been demonstrated only recently by using screw-shaped micrometer-sized particles made of non-chiral medium subjected to the action of a rotating magnetic field [60]. Merging microfluidic and field-induced options into an optofluidic chiral sorting scheme may offer new possibilities for a technology that arouses interest regarding present achievements and promising developments (see Ref. [61] and corresponding Focus Issue). Despite a few theoretical proposals of photoinduced chiral separations [62, 63, 64, 65, 66, 67], the realization of an optical chiral sorter is however missing so far.

In this chapter, we experimentally demonstrate the passive optical separation, in a fluidic environment, of mirror-imaged spherical chiral microparticles that differ only by opposite handedness by using chiral light fields. Importantly, the proposed optofluidic strategy does not require chiral-shaped microparticles and actually relies on the chirality of the medium, in contrast to previous experimental demonstration of chiral sorting based on hydrodynamical effects [55, 56, 57, 60]. Indeed, our method enables to sort material chirality by exploiting the dependence of optical radiation forces on the intrinsic handedness of matter and light.

The chapter is organized as follows. First, we present the principle of the

proposed sorting strategy (section 3.1) and the set-up used for the experimental demonstration (section 3.2). Then, in section 3.3, we unambiguously demonstrate the proposed chiral sorting technique using spherical cholesteric droplets exhibiting circular Bragg reflection. This demonstration is further generalized to the case of non-resonant chiral microspheres. Modeling part is presented in section 3.4, then the derived theoretical predictions are compared with our observations (section 3.5). Finally, we discuss in section 3.6 the outcome of our approach and describe a proposed optofluidic sorter enabling the separation of nanometer-sized or molecular-scale entities of chiral or non-chiral nature.

3.1 Principle of optical chiral sorting

The proposed concept is demonstrated in Fig. 3.1. It relies on the use of two counterpropagating circularly polarized collimated beams with opposite helicity $\Lambda = \pm 1$ but equal power and waist. In this figure the shaded area represents the spatial distribution of the optical field intensity and we consider spherical microparticles flowing at a velocity V_0 perpendicularly to the beam axes, say along the x axis. For a non-chiral material ($\chi = 0$), the net optical force component exerted on the object along the propagation direction of the beams, say the z axis, is zero by virtue of cancellation of the individual contributions of the two beams. In the absence of additional external forces exerted on the particle, its trajectory is thus straight. On the other hand, if the material is chiral ($\chi = \pm 1$),

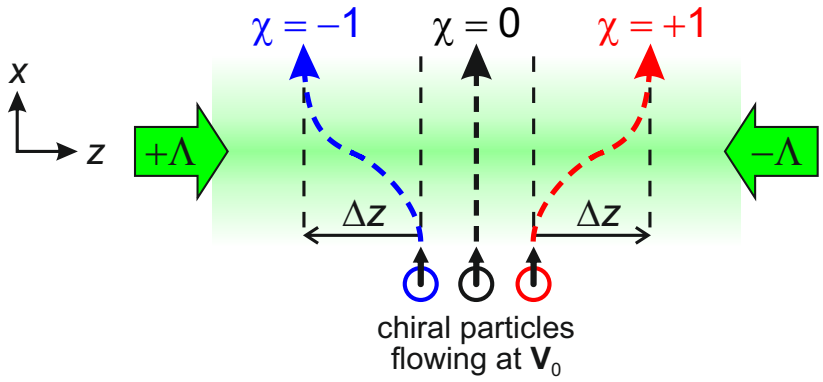

Figure 3.1: *Principle of the optical chiral sorting by chiral light: spherical particles, which differ only by their material chirality χ, travel with a velocity $\mathbf{V}_0$ across a chiral light field consisting of two counterpropagating coaxial collimated beams of identical intensity distribution, represented by the shaded area. The beams are circularly polarized with opposite helicities $\pm\Lambda$. Dashed lines show trajectories of the particles, which are spatially separated by the chiral field depending on their chirality.*

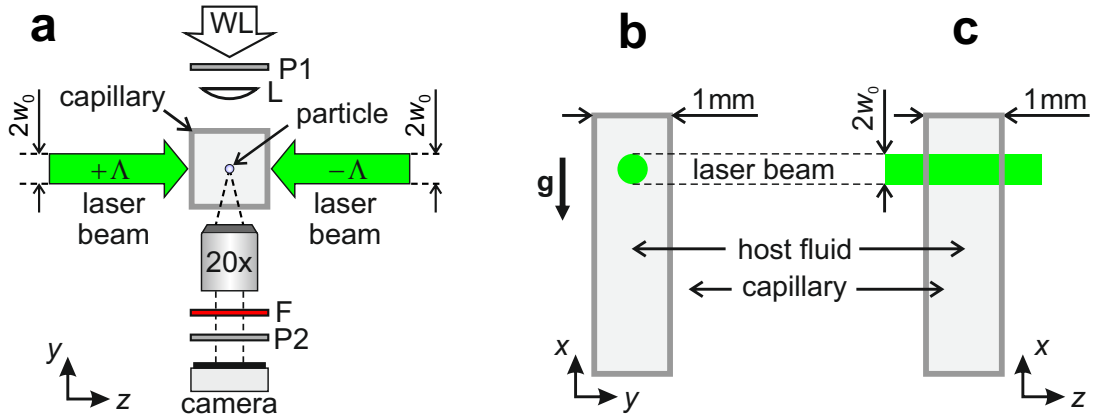

Figure 3.2: *A transparent spherical droplet is immersed in a uniform host fluid within a glass capillary. (***a***) Top view. (***b***) Side view on the sample, where* **g** *refers to gravitational acceleration. The sample can be moved vertically (along the x axis) so that the droplet crosses two circularly polarized coaxial collimated counterpropagating Gaussian-like laser beams with opposite helicities ($+\Lambda$ and $-\Lambda$), equal power, waist and wavelength. The imaging system is the same as described in section 2.2.*

the force balance does not hold anymore and a non-zero net force, which either originates from circular birefringence or circular dichroism, is now exerted on the particle. This consequently leads to a curved trajectory in the (x, z) plane. As it passes through the beams, the particle with $\chi = \pm 1$ is optically displaced along z by Δz, as depicted in Fig. 3.1. Noteworthy, the sign of Δz is expected to be reversed by changing the sign of either Λ or χ.

3.2 Experimental set-up

In practice we built the set-up sketched in Fig. 3.2. The sorting optical field is provided by two circularly polarized coaxial collimated counterpropagating Gaussian laser beams with opposite helicities ($+\Lambda$ and $-\Lambda$), equal power $P \sim 10 - 100$ mW, waist $w_0 \approx 50$ μm and vacuum wavelength $\lambda_0 = 532$ nm. The experimental sample consists of a glass capillary filled with an isotropic host fluid (aqueous glycerol solution with refractive index n_{ext} and dynamic viscosity η), in which spherical microscopic droplets are immersed. If densities of the droplet and the host fluid perfectly match, the motion of the droplet depends only on the controlled displacement of the sample, light-induced forces and ensuing viscous forces. The sample is displaced at a uniform velocity V_0 along the x axis in the (x, z) plane across the laser beams by means of a linear translation stage driven by a direct current micromotor. Both trajectories and velocities of the sorted

droplets are quantitatively retrieved by direct imaging procedure, as previously described in section 2.2.

For the purpose of thorough demonstration of the proposed concept we have used different types of chiral and non-chiral spherical droplets. The corresponding experimental studies are detailed in the following section.

3.3 Experimental proof-of-principle

3.3.1 Optomechanically resonant chiral sorting

Following the accomplishments of chapter 2, here we use radial optomechanically resonant cholesteric droplets of MDA-02-3211 (see section 1.1.2 for details) in order to experimentally demonstrate the proposed concept of chiral sorting concept. Such droplet is sketched in Fig. 3.3(a), where radial lines refer to the axes of supramolecular helices, **n** being the liquid crystal director. Panels (b–d) represent transmission images of a radial droplet of MDA-02-3211 immersed in a host fluid (≈ 25 wt% aqueous glycerol solution) viewed under various polarization conditions at λ_0 = 532 nm wavelength illumination. The overall radial ordering of the droplet is verified by the characteristic fourfold pattern viewed between crossed linear polarizers (XPOL). Images obtained under left- and right-handed circular polarized illumination (LHCP and RHCP) are shown in panels (c, d). Circular Bragg reflection from this right-handed (i. e. $\chi = +1$) cholesteric manifests itself by the dark disk of diameter $2R_B$ clearly seen in the RHCP case.

As demonstrated in section 2.5, radial droplets of MDA-02-3211 in the two-beam scheme are strongly pushed along the wavevector of the Bragg-polarized beam. Since the direction of this light-induced deviation of the droplet trajectory is defined by the product $\Lambda\chi$, both directions can be obtained with the same material by changing the sign of the helicity of the two beams. We realize this experimentally by using two preset quarter-wave plates on flip mounts.

The experimental demonstration of optical chiral sorting is performed using an immersed MDA-02-3211 droplet of radius $R \approx 7\,\mu$m, being displaced together with the capillary at the velocity $V_0 \approx 12$ μm s^{-1} along the x axis through the chiral optical field formed by the two laser beams with power P = 170 mW. Fig. 3.3(e,f), compile snapshots of the droplet dynamics for $\Lambda\chi = -1$ and $\Lambda\chi = +1$, respectively, which leads to the droplet deviation with the opposite sign. Due to the bounded nature of the light beams, a chiral droplet experiences a finite displacement along z, namely $\Delta z = z_{+\infty} - z_{-\infty}$, where $z_{\pm\infty}$ refers to the z coordinate of the droplet center of mass at time $t = t_{\pm\infty}$, with $t = 0$ when the droplet crosses the beam axis at $x = 0$. The fact that $\Delta z \propto \Lambda\chi$ demonstrates the ability to sort objects with different chirality by chiral light.

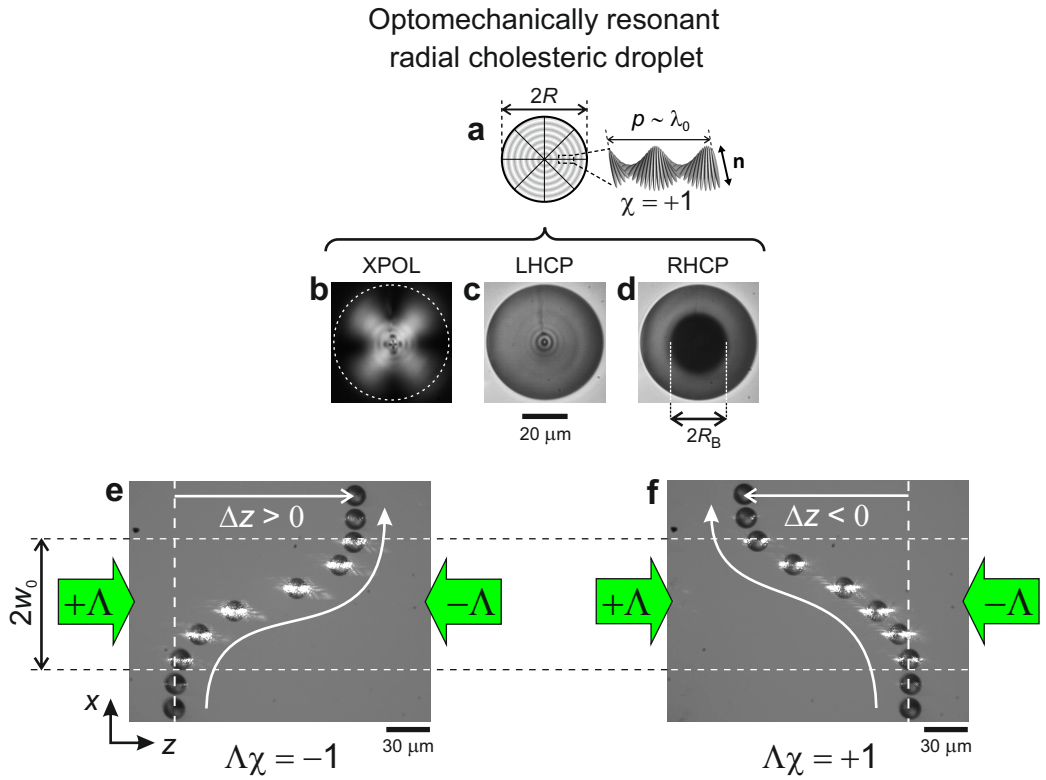

Figure 3.3: *Experimental demonstration of chiral optical sorting concept by means of optomechanically resonant radial cholesteric droplets.* (**a**) *Sketch of the used droplet, where radial lines refer to the axes of supramolecular helices and* **n** *is the liquid crystal director.* (**b**) *Image of the droplet between crossed linear polarizers (XPOL) at* $\lambda_0 = 532$ *nm wavelength. The dashed circle refers to the contour of the droplet.* (**c**, **d**) *Transmission images under left- and right-handed circularly polarized illumination at* λ_0 *confirming the presence of helicity dependent circular Bragg reflection (see section 1.1.2 for details)* (**e**, **f**) *A Bragg cholesteric droplet is displaced by external means at a constant velocity* V_0 *along the* x *axis through the laser beams having opposite helicities* ($+\Lambda$ *and* $-\Lambda$). *Owing to the circular Bragg reflection, the droplet experiences a non-zero deviation* $\Delta z \propto \Lambda\chi$ *along the direction of propagation of the beam having a helicity that satisfies* $\Lambda\chi = -1$. *The pictures are obtained by superimposing snapshots taken at a discrete set of time. Parameters: power of one beam is* $P = 170$ *mW, beam waist is* $w_0 \approx 50$ μ*m, droplet radius is* $R \approx 7$ μ*m, driving velocity is* $V_0 \approx 12$ $\mu m\, s^{-1}$, *host fluid is a* ≈ 25 *wt% aqueous glycerol solution.*

3.3.2 Generalization of chiral optical sorting

Importantly, the proposed optical chiral sorting strategy is not restricted to optomechanically resonant chiral interaction as is the case for Bragg chiral droplets. In fact, our method is expected to work for non-resonant chiral spheres as well. In order to prove it, we have tested radial cholesteric droplets prepared by mixing a (non-chiral) nematic liquid crystal E7 (from Merck) with ≈ 5 wt.% of chiral dopant S811 or R811 (both from Merck), which respectively gives the left-handed or right-handed supramolecular helices with a pitch $p \approx 2$ μm - roughly 6 times larger than the pitch of MDA-02-3211. According to the tabular dataset, E7 has the average refractive index $n \approx 1.6$ and anisotropy $\Delta n \approx 0.2$. Using Eqs. (1.1), (1.2), we estimate the Bragg wavelength for the above E7-based cholesteric materials as $pn \approx 3.2\,\mu$m, while the circular Bragg reflection bandwidth is expected to be $p\Delta n \approx 400$ nm wide. Therefore, these materials are considered as non-Bragg at the used wavelength $\lambda_0 = 532$ nm.

Radially ordered droplets are obtained via mechanical stirring of the cholesteric material in the host fluid, which in this case is a ≈ 15 wt% aqueous glycerol solution (the right percentage has been determined in situ by observing the droplet motion inside the capillary in the absence of laser illumination). Radial droplets of right-handed (E7 doped with R811) and left-handed (with S811) are sketched in Fig. 3.4(a,b), respectively. The investigated cholesteric droplets viewed between crossed linear polarizers (panels (c, f)) demonstrate a signature of the four-fold pattern, which confirms the overall radial ordering. Chirality of the droplets reveals itself as spiraling texture clearly visible in panels (c–h). The absence of the circular Bragg reflection at λ_0 is seen from the almost identical transmission images of the droplets obtained under left-handed (panels (d, g)) and right-handed (panels (e, h)) circularly polarized illumination. It is interesting to note that Λ-sensitivity of light scattering is seen from these images. Also we see the inversion when changing the sign of χ.

The chirality-dependent optomechanical effect is demonstrated by the snapshots compilations in Figs. 3.4(i,j). However, the light-induced deviation of the droplet is typically 20 times smaller than the one obtained in the Bragg case when considering identical optical power, driving velocity and droplet radius. This impressive difference results from the fact that the helicity-dependent scattering of light by non-Bragg chiral microspheres is not a resonant process, in contrast to circular Bragg reflection, which was at work in the experiments reported in subsection 3.3.1.

We notice that the helicity-dependent optomechanical effect (i. e. the light-induced axial deviation Δz) obtained in the non-Bragg case is opposite to the one reported in Fig. 3.3 for the Bragg case. This is explained recalling that optical force exerted on a chiral microsphere does not depend solely on the handedness of the material, but also on its chirality "strength", which characterizes

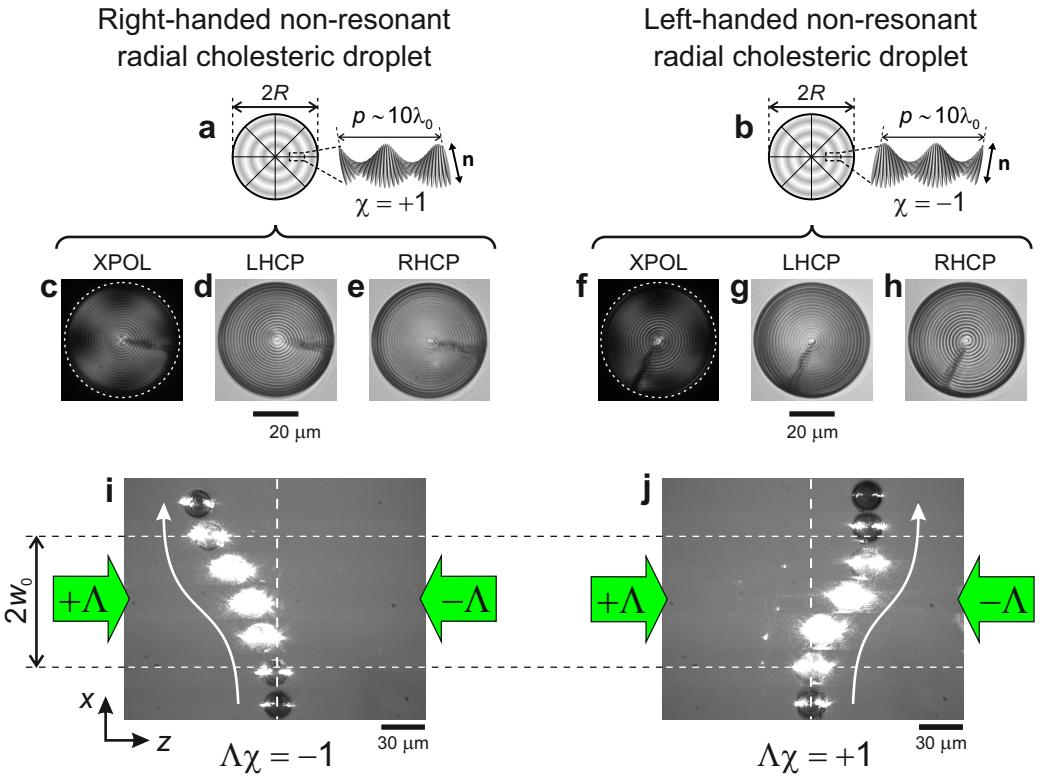

Figure 3.4: *Sorting chiral radial cholesteric droplets by chiral light without relying on circular Bragg reflection phenomenon. Upper panels: sketches of right-handed (***a***) and left-handed (***b***) radial cholesteric droplets obtained by mixing the nematic E7 with ≈ 5 wt.% of chiral dopant R811 or S811, respectively. Notations are the same as in Fig. 3.3. (***c***, ***f***) XPOL images demonstrate the signature of radial ordering in such long-pitch ($p \approx 2$ μm) cholesteric droplets. The transmission images under LHCP (***d***, ***g***) and RHCP (***e***, ***h***) illumination at $\lambda_0 = 532$ nm show no sign of circular Bragg reflection. Bottom panels: optical sorting experiment for right-handed (***i***) and left-handed (***j***) droplets. The sign of the optically induced deviation along the z axis depends on the material chirality at fixed optical field, thereby extending the proposed optofluidic chiral sorting scheme to non-Bragg chiral microspheres. Parameters: $P = 540$ mW, $w_0 \approx 50$ μm, $R \approx 9\,\mu m$, $V_0 \approx 12$ $\mu m\ s^{-1}$.*

the cross-coupling between the magnetic and electric field in chiral media (see for instance [68]). For example, as shown by theoretical curves in Fig. 4 of [69], the difference of optical radiation forces exerted on a chiral sphere by RHCP and LHCP Gaussian beams can be positive as well as negative, even if the material chirality does not change sign. Therefore, the reversed light-induced displacement observed for non-Bragg droplets emphasizes the role of the chirality strength when dealing with optomechanics of chiral media.

Put together, all the observations reported in subsections 3.3.1, 3.3.2 demonstrate the generality of the proposed optical sorting technique, that may be extended into a microfluidic environment. Indeed, as shown in Fig. 3.3, one easily gets $\Delta z \gg R$ within a few seconds and with 100% efficiency. Typically, we have $\Delta z \sim R$ in one second using $P \sim 10$ mW and $V_0 \sim 10$ μm s^{-1}.

Moreover, the obtained dependencies of Δz on (i) optical chirality at fixed material chirality (see Fig. 3.3) and (ii) material chirality at fixed optical chirality (see Fig. 3.4) fully demonstrate an optofluidic chiral sorting basically associated with light-induced separation that scales as $\Delta z \propto \Lambda\chi$.

3.3.3 "Null" experiment: the non-chiral case

3.3.3.1 Optically isotropic non-chiral microspheres

A "null" experimental test has been performed in order to verify that trajectories of non-chiral particles are unaffected by the chiral field in the considered sorting scheme, as depicted in Fig. 3.1 by the straight line corresponding to $\chi = 0$. For this purpose, we have initially used isotropic spherical droplets of PDMS (polydimethylsiloxane fluid, from Clearco Products Co., Inc.). Spherical droplets of have been produced by mechanical stirring of PDMS in pure water, which serves as a host fluid in this case.

In practice, the test was realized with a PDMS droplet having $R \approx 9\,\mu$m. The compilation of snapshots of the chosen droplet taken at a discrete set of time is presented in Fig. 3.5. As expected, in contrast to the chiral microspheres, the isotropic droplet's trajectory is a straight line along x, regardless of the helicities of the laser beams.

3.3.3.2 Optically anisotropic non-chiral microspheres

The case of non-chiral optically anisotropic particles has also been tested in order to unambiguously demonstrate that it is the material chirality and not its anisotropy that is responsible for the chiral optical separation. For this purpose, we have chosen the nematic E7, whose refractive indices are very close to those of MDA-02-3211.

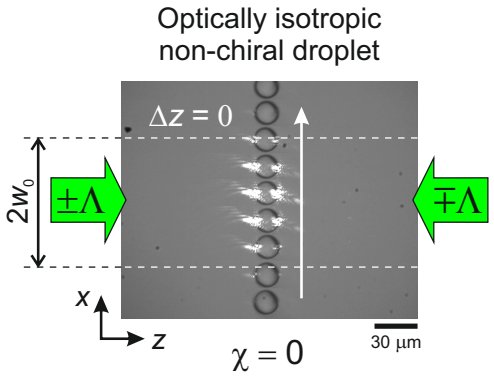

Figure 3.5: *A spherical isotropic droplet of PDMS moves along the x axis and passes perpendicularly through the beams of opposite helicities $\pm\Lambda$. The trajectory is unperturbed by the chiral light field, as is indicated by the straight trajectory. Parameters: $P = 170$ mW, $w_0 \approx 50$ μm, $R \approx 9\,\mu$m, $V_0 \approx 12$ μm s^{-1}.*

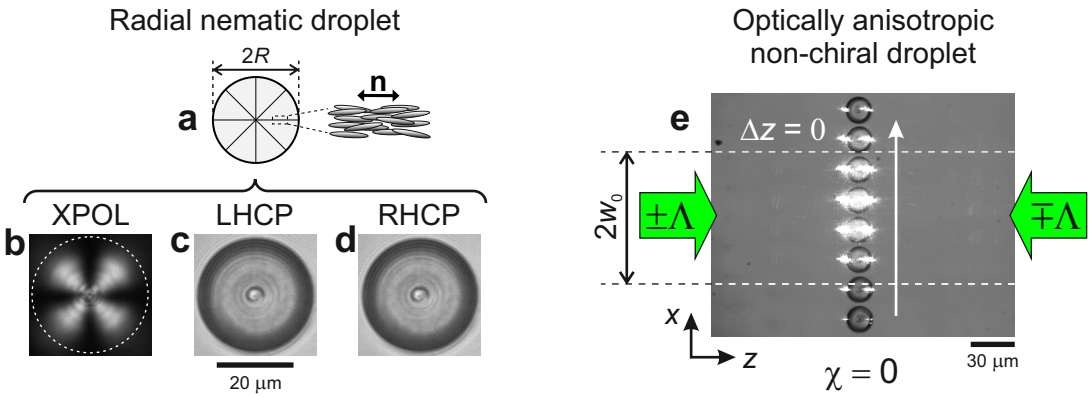

Figure 3.6: *"Null" sorting experiment with a non-chiral optically anisotropic radially ordered nematic liquid crystal droplet. (**a**) Sketch of the director field, where radial lines refer to the director orientation. (**b**) Image of the droplet viewed between crossed linear polarizers, where the dashed circle refers to the contour of the droplet. (**c**,**d**) Images of the droplet under left- and right-handed circularly polarized illumination. The imaging is performed at 532 nm wavelength. (**e**) Compilation of the snapshots demonstrating the straight trajectory of a radial nematic droplet across the chiral field. Parameters: $P = 170$ mW, $w_0 \approx 50$ μm, $R \approx 7.5\,\mu$m, $V_0 \approx 12$ μm s^{-1}.*

Radial nematic droplets were obtained by dispersing E7 in a quasi-isodense aqueous glycerol solution[1] with a small fraction (0.2 g/L) of surfactant CTAB (cetyltrimethylammonium bromide, from Sigma-Aldrich) that promotes a perpendicular alignment of the director $\mathbf{n}$ at the droplet interface and subsequent radial director ordering in the bulk, as sketched in Fig. 3.6(a).

The radial symmetry of the director field is identified by a four-fold intensity pattern when observing a radial nematic droplet between crossed linear polarizers (see Fig. 3.6(b)). As shown in the images under LHCP and RHCP illumination (panels (c) and (d) in Fig. 3.6, respectively), optical properties of a radial nematic droplet do not depend on the photon helicity of the incident light. The panel (e) compiles successive snapshots (taken at a discrete set of time) of the radial nematic droplet with radius $R \approx 7.5\,\mu$m driven through the chiral light field at the velocity $V_0 \approx 12\ \mu\text{m s}^{-1}$ along x axis. The resultant trajectory is straight, regardless of the helicities of the beams, which concludes our demonstration.

3.4 Model

Optomechanics of a Bragg [2] radial cholesteric droplet illuminated by the applied two-beam chiral field is modeled within the ray-optics approach, as described in section 1.3. The key difference between the sorting environment and the light-matter system considered in section 2.4 consists in axial symmetry breaking of the system in the sorting case once the droplet does not lie on the beam axis. Therefore, in general, there are non-zero transverse components of the net optical force exerted on the droplet. Moreover, gradient of the field intensity over the beam cross-section implies the dependance of light-induced forces and velocities on the droplet location.

3.4.1 Optical forces

The laboratory coordinate system with unit vectors $\mathbf{x}$, $\mathbf{y}$ and $\mathbf{z}$ has been introduced in section 3.2. The Cartesian basis (x', y', z') is obtained by the parallel translation of the laboratory basis to the droplet center located at $(x, 0, z)$, as shown in Fig. 3.7. A spherical coordinate system with polar and azimuthal angles θ and ϕ originates at the droplet center and serves for deriving the elementary optical force $d\mathbf{F}(x, \theta, \phi)$ exerted on the droplet by a single ray impinging on a surface element $dS(\theta, \phi) = R^2 \sin\theta d\theta d\phi$ (see subsection 1.3.2). Note that in the considered light-matter system the elementary force does not depend of the axial

[1] Density of the nematic E7 at room temperature is about 1.03 g cm^{-3} [70]. Thus isodense conditions correspond to ≈13 wt% aqueous glycerol solution [31]

[2] We do not report here neither modeling nor experimental statistics for non-Bragg droplets. If one would consider the latter case, the helicity-dependent chiral scattering issue has to be taken into account (see for instance [69]).

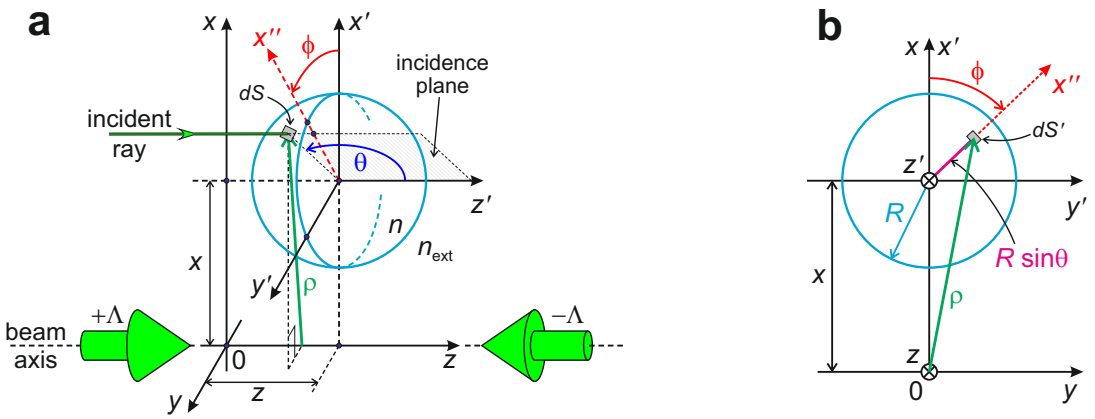

Figure 3.7: (**a**) *Sketch of a spherical droplet (with* $\chi = -\Lambda$*) interacting with the considered two-beam chiral optical field. A single ray impinging on a surface element* dS *of the droplet is depicted.* (**b**) *Distance* ρ *between the surface element and the beam axis* z *can be easily derived using the projection on the* (x, y) *plane (*dS' *represents the projection of* dS*).*

coordinate z, since the incident beams are collimated and thus have identical intensity distribution in any plane perpendicular to the z axis. Panel (a) in Fig. 3.7 illustrates the interaction of a spherical droplet with a single incident ray in three dimensions. The projection on the (x, y) plane sketched in panel (b) helps to derive the useful distance between the beam axis z and the considered surface element dS, namely

$$\rho(x, \theta, \phi) = \sqrt{x^2 + 2xR\sin\theta\cos\phi + R^2\sin^2\theta}\,. \tag{3.1}$$

Indeed, $\rho(x, \theta, \phi)$ unambiguously defines the optical field intensity at the location of the surface element dS. In the present case of collimated coaxial Gaussian beams with equal power P and waist w_0, Eq. (1.12) gives the local optical intensity

$$I(\rho, z) = I(x, \theta, \phi) = \frac{2P}{\pi w_0^2}\exp\left[-\frac{2\rho^2}{w_0^2}\right]. \tag{3.2}$$

Then, using the listed notations and Eq. (1.26), we write the elementary optical force on the droplet as follows

$$\begin{aligned} d\mathbf{F}(x, \theta, \phi) &= -\frac{n_{\text{ext}}R^2}{2\text{c}} I(x, \theta, \phi) \\ &\times \left[f_\perp(\theta)(\cos\phi\,\mathbf{x} + \sin\phi\,\mathbf{y}) + f_\parallel(\theta)\,\mathbf{z}\right]\sin 2\theta\, d\theta d\phi\,, \end{aligned} \tag{3.3}$$

where the coefficients $f_\parallel(\theta)$ and $f_\perp(\theta)$ are given by Eqs. (1.24), (1.25).

As in section 2.4, we consider the wavevector of the Bragg-polarized ($\Lambda\chi = -1$) beam pointing along $\mathbf{z}$, whereas the anti-Bragg ($\Lambda\chi = +1$) beam propagates

towards $z < 0$, in agreement with the sketch shown in Fig. 3.3(e,f). The net optical force exerted on the droplet is thus obtained by integrating $d\mathbf{F}(x,\theta,\phi)$ over the whole irradiated surface of the droplet. Namely, over

- $\{\pi/2 \le \theta \le \pi,\ 0 \le \phi \le 2\pi\}$ for the Bragg beam;
- $\{0 \le \theta \le \pi/2,\ 0 \le \phi \le 2\pi\}$ for the anti-Bragg beam.

Since the light-matter system is characterized by the mirror symmetry relative with respect to the (x,z) plane, the net optical force acting on a radial droplet along the y axis is zero. The other components of the net optical force are

$$F_x(x) = -\frac{n_{\text{ext}} P R^2}{\pi c w_0^2} \int_0^{2\pi}\int_0^{\pi} \exp\left[-\frac{2\rho^2(x,\theta,\phi)}{w_0^2}\right] f_\perp(\theta) \sin 2\theta \cos\phi \, d\theta \, d\phi \qquad (3.4)$$

and

$$F_z(x) = -\frac{n_{\text{ext}} P R^2}{\pi c w_0^2} \int_0^{2\pi}\int_0^{\pi} \exp\left[-\frac{2\rho^2(x,\theta,\phi)}{w_0^2}\right] f_\parallel(\theta) \sin 2\theta \, d\theta \, d\phi \,. \qquad (3.5)$$

The key feature of the proposed sorting scheme is the light-induced spatial separation of the sorted chiral spheres along the beam axis z (see the principle sketch in Fig. 3.1). Noticeably,

- the contribution made by non-Bragg rays into the z-component of the net optical force exerted on a radial cholesteric droplet in the considered two-beam light field is negligible if compared with the contribution made by Bragg rays (this is supported by the results of section 2.5);
- the cross-section of the Bragg-reflecting area of the droplet surface has the radius $R_{\text{B}} = R \sin\theta_{\text{B,ext}} < R/2$ for $\theta_{\text{B,ext}} < 30°$ [3]. Using the parameters of our experiments reported in section 3.5, $R_{\text{B}} < 7.5\,\mu$m, which is about 6.5 times less than the beam waist $w_0 \approx 50\,\mu$m. Thus we neglect variations of the optical intensity within the Bragg-reflecting area of the droplet. In other words, we assume $\rho \simeq x$.

Under these two approximations, Eq. (3.5) can be simplified as follows:

$$F_z(x) \simeq \frac{2 n_{\text{ext}} P R^2 (1 - \cos^4\theta_{\text{B,ext}})}{c w_0^2} \exp\left[-\frac{2x^2}{w_0^2}\right]. \qquad (3.6)$$

[3] Note that the maximum value of θ_{B} obtained in chapter 2 via fitting of the experimental data corresponds to $\theta_{\text{B,ext}} \approx 25.4°$.

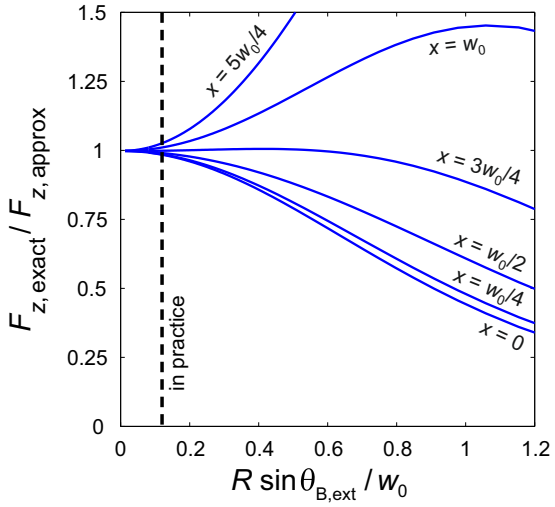

Figure 3.8: *Simulated ratio between the exact and approximate expressions for the z-component of the net optical force exerted on a Bragg cholesteric droplet in the chiral sorting scheme. Parameters:* $n = 1.6$, $n_{\mathrm{ext}} = 1.365$, $\theta_{\mathrm{B,ext}} = 25°$, $R = 15\,\mu m$, $5\,\mu\mathrm{m} \leq w_0 \leq 500\,\mu m$. *Dashed line indicates the value* $R\sin\theta_{\mathrm{B,ext}}/w_0 \approx 0.125$, *which we have in practice* ($w_0 \approx 50\ \mu m$).

The validity of such an approximation has been numerically checked by showing that with our actual experimental parameters we have

$$\frac{F_{z,\mathrm{exact}}(x)}{F_{z,\mathrm{approx}}(x)} = \frac{-\int_0^{2\pi}\int_0^{\pi} \exp\left[-\frac{2\rho^2(x,\theta,\phi)}{w_0^2}\right] f_{\parallel}(\theta)\sin 2\theta\, d\theta\, d\phi}{2\pi(1-\cos^4\theta_{\mathrm{B,ext}})\exp\left[-\frac{2x^2}{w_0^2}\right]} \simeq 1\,, \tag{3.7}$$

where $F_{z,\mathrm{exact}}(x)$ and $F_{z,\mathrm{approx}}(x)$ respectively refer to the exact (Eq. (3.5)) and approximate (Eq. (3.6)) expressions for the z-component of net optical force exerted on a Bragg cholesteric droplet. Indeed, in practice we have $R\sin\theta_{\mathrm{B,ext}}/w_0 \approx 0.125$, which corresponds to the maximum error of 2 % appearing from the above approximation, as one can see in Fig. 3.8, where the ratio $F_{z,\mathrm{exact}}(x)/F_{z,\mathrm{approx}}(x)$ has been simulated as a function of the parameter $R\sin\theta_{\mathrm{B,ext}}/w_0$ for various droplet locations x.

Therefore, we use the analytical Eq. 3.6 when deriving the trajectory, $z(x)$, and total light-induced deviation, Δz, of a Bragg cholesteric droplet (see next subsection). Unlike the z-component of the net optical force, the x-component is expected to have a minor contribution to Δz, thus we do not derive any approximate expressions for $F_x(x)$.

3.4.2 Velocities and trajectories

As discussed in subsection 1.3.4, the balance between the viscous force exerted by the surrounding fluid on the moving droplet and the driving optical force gives the light-induced droplet velocity. Its components along the x and z axes equal

$$v_j(x) = \frac{F_j(x)}{6\pi\eta R} \tag{3.8}$$

with $j = x, z$ and $F_{x,z}(x)$ given by Eqs. (3.4), (3.6). We notice that the total droplet velocity along x has also a non-optical component, V_0, and expresses as $V_x(x) = V_0 + v_x(x)$.

Once velocities of the droplet at every point are known, the droplet trajectory can be retrieved. This is done by noting that $V_x(x) = dx/dt$ and $v_z(x) = dz/dt$, which leads to $dz = [v_z(x)/(v_x(x) + V_0)]\,dx$. Integration of dz along the x axis thus gives access to the droplet trajectory $z(x)$ and total deviation Δz. Namely,

$$z(x) = \int_{-\infty}^{x} \frac{v_z(x)}{v_x(x) + V_0} dx\,, \tag{3.9}$$

$$\Delta z = \int_{-\infty}^{+\infty} \frac{v_z(x)}{v_x(x) + V_0} dx\,. \tag{3.10}$$

In particular, when Eq. (3.6) is valid and under the approximation $v_x \ll V_0$, one gets

$$\Delta z \simeq \frac{1}{V_0}\int_{-\infty}^{+\infty} v_z(x)dx \approx \frac{n_{\text{ext}} PR\,(1-\cos^4\theta_{\text{B,ext}})}{3\pi\eta c w_0^2 V_0}\int_{-\infty}^{+\infty} \exp\left[-\frac{2x^2}{w_0^2}\right]dx\,; \tag{3.11}$$

$$\Delta z \approx \frac{n_{\text{ext}} R\,(1-\cos^4\theta_{\text{B,ext}})}{3\sqrt{2\pi}\eta c w_0}\,\frac{P}{V_0}\,, \tag{3.12}$$

and thus the droplet trajectory simplifies to

$$z(x) \approx \Delta z\,\Phi\left(\frac{2x}{w_0}\right), \tag{3.13}$$

where Φ is the normal cumulative distribution function,

$$\Phi(\beta) = \frac{1}{\sqrt{2\pi}}\int_{-\infty}^{\beta} \exp\left(-\alpha^2/2\right) d\alpha$$

with α and β being real-valued variables.

By introducing the reduced coordinates $\widetilde{x} = x/w_0$ and $\widetilde{z} = (z - z_{-\infty})/\Delta z$, the droplet trajectory adopts a universal expression

$$\widetilde{z}(\widetilde{x}) = \Phi(2\widetilde{x})\,, \tag{3.14}$$

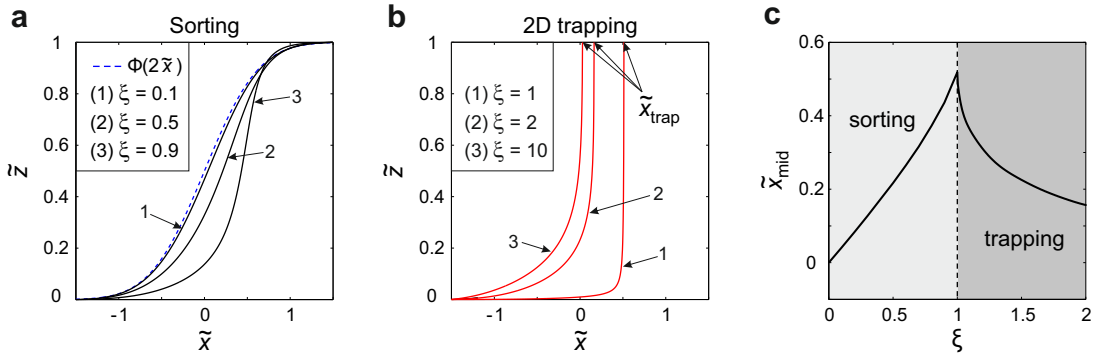

Figure 3.9: *Simulation of reduced trajectories of a Bragg cholesteric droplet moving across the chiral light field.* (**a**) *The larger is* $\xi = \delta/\delta_c < 1$ *(see text for details), the larger is the deviation of the droplet from the universal behavior (dashed curve).* (**b**) *At* $\xi \geq 1$*, the droplet is eventually trapped in 2D and guided along the beam axis.* (**c**) *Deviations from the universal behavior in the regimes of sorting and 2D trapping, where* $\widetilde{x}_{\mathrm{mid}}$ *is the reduced distance of the droplet from the beam axis at* $\widetilde{z} = 0.5$*, here plotted as a function of* ξ*.*

which is valid in our case if $v_x \ll V_0$.

This universal trajectory is shown by the dashed line in Fig. 3.9(a). The other three trajectories have been simulated using Eqs. (3.8) and (3.9) with the net optical force components given by Eqs. (3.4) and (3.5). Parameters of the light-matter system were the same as the experimental ones, except for the quantity $\delta = P/V_0$ that varies typically from 1 to 10 kN. As follows from the simulations, the larger is δ, the larger is the deviation of the droplet trajectory from the universal one.

In particular, when P/V_0 exceeds a certain critical value δ_c, the droplet is trapped in two dimensions (2D) by light at $x = x_{\mathrm{trap}}$ and is consequently guided along the z axis towards the $\pm z$ direction depending on the sign of $\Lambda\chi$, whereas the transverse location of the droplet center $\widetilde{x} = \widetilde{x}_{\mathrm{trap}}$ is constant (see Fig. 3.9(b)). Using actual experimental parameters and $R = 15$ μm (as in section 3.5, where the quantitative study is reported), we numerically find $\delta_c \approx 9.66$ kN, which typically corresponds to $P = 100$ mW and $V_0 = 10$ μm s^{-1}. The transition between sorting and 2D trapping regimes is presented in Fig. 3.9(c) that displays the reduced distance $\widetilde{x} = \widetilde{x}_{\mathrm{mid}}$ corresponding to $\widetilde{z} = 0.5$, as a function of $\xi = \delta/\delta_c$.

3.5 Quantitative experimental study

Dynamics of a typical Bragg droplet has been experimentally investigated for various laser beam power P and the driving velocity V_0. The set of data reported in this chapter comprises 48 independent experiments performed with a

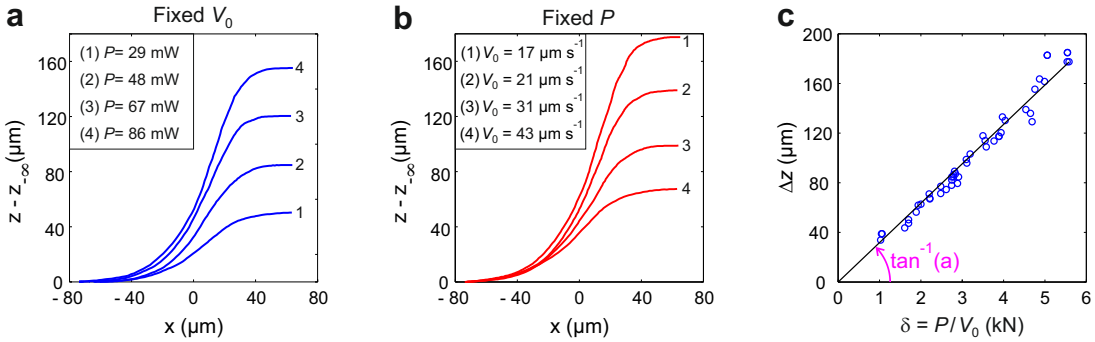

Figure 3.10: *Typical trajectories of a Bragg cholesteric droplet moving across the chiral light field, measured: (***a***) at fixed driving velocity $V_0 \approx 17$ μm s^{-1} and variable laser beam power P, (***b***) at fixed power $P \approx 95$ mW and variable velocity V_0. (***c***) Measured droplet deviation along the z axis, Δz, as a function of the parameter $\delta = P/V_0$ for 48 independent realizations. Solid line is the best linear fit passing through the origin.*

single droplet of radius $R \approx 15\,\mu$m for 19 mW $\leq P \leq$ 95 mW and 17 μm s^{-1} $\leq V_0 \leq$ 43 μm s^{-1}. Trajectories and velocities of the droplet are retrieved from videos of its motion recorded by means of the imaging system (see Fig. 3.2) and analyzed frame by frame using the MATLAB software environment. Namely, the initial droplet location in the (x, z) plane was identified in the first frame by cropping a representative piece of the droplet image. Then, using this piece as a reference, the relative droplet locations in the next frames were determined by cross-correlation.

Then, the known frame rate gives access to the time-dependent displacement of the droplet. Assuming that the velocity for two successive frames is constant (which is reasonable since our model describes light-induced forces by smooth functions), we derive the time and coordinate dependence of the droplet velocity. As for the driving velocity V_0, it was preset by calibrating the micromotor rotation rate as a function of the applied direct voltage. However, accounting for possible instability of mechanical friction or other sources of systematic errors, we also measured V_0 in situ as the droplet velocity in the parts of the trajectory where the light field intensity was close to zero (for $|\widetilde{x}| \geq 1.2$ in practice).

3.5.1 Light-induced droplet displacement

Typical measured trajectories are presented in Fig. 3.10(a,b). We have found that the total deviation of the droplet, Δz, increases with the increase of P at fixed V_0 and reduces with the increase of V_0 at fixed P. The complete set of experimental realizations is summarized in panel (c), where the total deviation is plotted as a function of the generalized parameter $\delta = P/V_0$. As one can see, the

experimental dataset exhibits a linear dependence on δ, as indicated by straight solid line $\Delta z = a\delta$, that refers to the best linear fit with $a = 31.8$ nm N^{-1}.

The observed linear dependence is actually predicted by Eq. (3.12), where we recognize the prefactor

$$a = \frac{n_{\text{ext}} R(1 - \cos^4 \theta_{\text{B,ext}})}{3\sqrt{2\pi}\eta c w_0} \,. \tag{3.15}$$

Substituting of the experimentally found value into Eq. (3.15), we obtain $\theta_{\text{B,ext}} = 25.1 \pm 1.1°$, hence $\theta_{\text{B}} = 21.3 \pm 0.9°$, which fairly agrees with our previous direct (see section 1.1.2) and indirect (see section 2.5) measurements.

3.5.2 Light-induced droplet trajectories

The reduced trajectories measured for the 48 experimental realizations introduced in subsection 3.5.1 are shown in Fig. 3.11. In agreement with the predictions of our model, the trajectories demonstrate a deviation from the universal behavior, that increases with δ (see the zoomed central parts in panels (a, b). A more quantitative assessment of this trend is presented in panel (c), where the experimental dataset of $\widetilde{x}_{\text{mid}}$ (markers) is superimposed with the results of simulations (solid curve).

We also conclude that the predictions regarding the 2D trapping regime (see Fig. 3.9(b,c)) agree with our observations since the experimental data corresponds

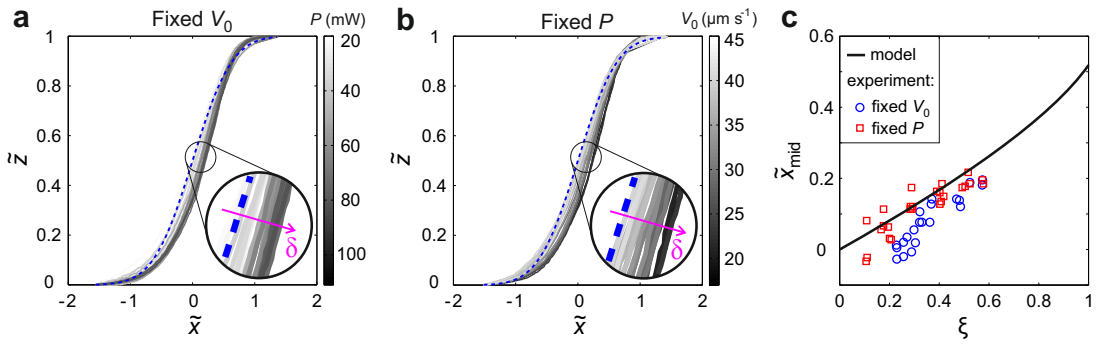

Figure 3.11: *(**a**,**b**) Reduced trajectories of the radial cholesteric droplet in the coordinate system* $(\widetilde{x}, \widetilde{z}) = (x/w_0, (z - z_{-\infty})/\Delta z)$ *when* P *is varied at fixed velocity* $V_0 \approx 17$ *μm* s^{-1} *(**a**) and when* V_0 *is varied at fixed power* $P \approx 95$ *mW (**b**). Enlargement windows point out the trend as the parameter* $\delta = P/V_0$ *increases: the larger is* δ*, the larger is the deviation from the universal trajectory given by* $\Phi(2\widetilde{x})$ *and represented here by dashed curves. (**c**) Measured reduced distance* $\widetilde{x} = \widetilde{x}_{\text{mid}}$ *at* $\widetilde{z} = 0.5$*, as a function of the reduced parameter* $\xi = \delta/\delta_c$ *with* $\delta_c \approx 9.66$ *kN. Solid line refers to simulation. Parameters: beam waist is* $w_0 \approx 50$ *μm and droplet radius is* $R \approx 15$ *μm.*

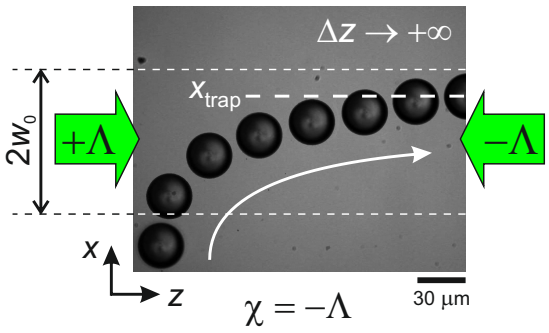

Figure 3.12: *Demonstration of the 2D trapping and ensuing continuous guiding of a Bragg cholesteric droplet (radius $R \approx 15$ μm). Transition from the sorting regime to 2D trapping occurs when the dimensionless parameter $\xi = \delta/\delta_c$ exceeds unity. With the actual geometry of the light-matter system, refractive indices and host fluid viscosity, simulation gives $\delta_c \approx 9.66$ kN. Here the experiment is realized at $\delta \approx 10.8$ kN, which corresponds to $\xi \approx 1.1$.*

to the range $0.1 < \xi < 0.6$, hence dealing with the chiral sorting regime without trapping. Even though optical trapping of chiral droplets is out of the scope of the present chapter, we have made a few qualitative experimental tests that confirm the existence of 2D trapping regime when the dimensionless parameter ξ exceeds unity. This is illustrated in Fig. 3.12 that demonstrates the motion of a Bragg cholesteric droplet of radius $R \approx 15\,\mu$m at $\delta \approx 10.8$ kN, which corresponds to $\xi \approx 1.1$.

3.5.3 Light-induced droplet velocities

The reliability of our experimental approach and its quantitative description are further emphasized by looking at the droplet dynamics in the sorting regime. Its statistical analysis is presented in panels (a) and (b) in Figs. 3.13, where the longitudinal and the transverse light-induced droplet velocity components, v_z and v_x, divided by P for the sake of universalization, are presented for the experimental dataset shown in Fig. 3.10(c). The standard deviation range was determined independently for every $\widetilde{x}$ location, then the corresponding dataset has been smoothed by a polynomial fit. On the other hand, the dashed curves display the light-induced velocities of the Bragg cholesteric droplet simulated by means of Eq. (3.8) using the actual experimental parameters, without additional fitting procedures.

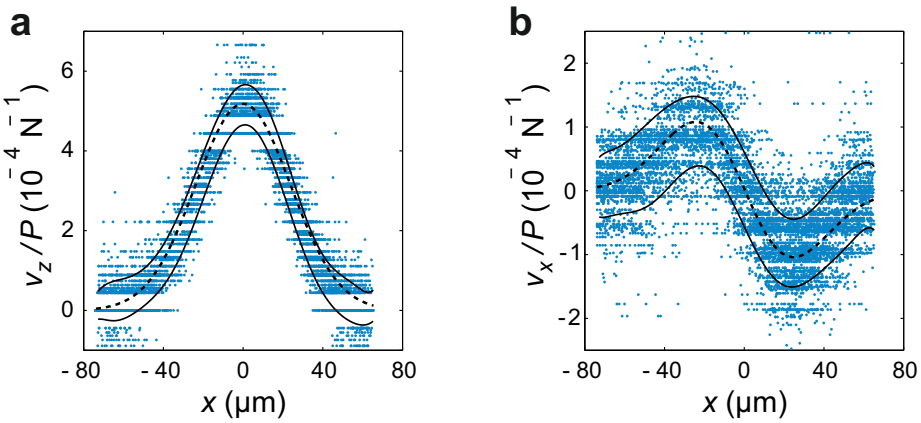

Figure 3.13: *Droplet dynamics in the sorting regime. Experimental longitudinal (***a***) and transverse (***b***) light-induced droplet velocity components (divided by P) during the optical chiral sorting dynamics for the 48 independent realizations presented in Fig. 3.10(c). Markers are experimental data, solid curves outline the experimental standard deviation range and dashed curves refer to simulations.*

3.6 Discussion and outlook

The demonstrated quantitative agreement between our observations and the predictions of our model without need for adjustable parameters eliminates the possibility that thermal effects are at the origin of the reported results. Also, this agreement proves that the proposed optical sorting scheme is immune to the influence of radial defects, which unavoidably present in radial cholesteric droplets [13, 14] and formally break their spherical symmetry. Predictable realizations of the chiral optical sorting strategy has been demonstrated with both Bragg (Fig. 3.3) and non-Bragg (Figs. 3.4) chiral droplets. This emphasizes the generality of the reported results on optofluidic sorting of chiral microspheres by chiral light.

A natural extension of the present work would consist in the spatial downscaling from the micron scale to molecular scale. Indeed, despite an obvious practical interest, there are only a few theoretical works dealing with electromagnetic field-induced mechanical separation of nanometer sized chiral entities [58, 59, 62, 63, 64, 65, 66, 67] while no experimental realization has been reported so far. To this aim, we stress that it is however not relevant to consider sub-micrometric Bragg droplets since their formation requires a droplet diameter sufficiently larger than the pitch, which scales as wavelength if one wants to ensure circular Bragg reflection and the consequent optomechanically resonant effect. Outside resonance, optomechanical effects are obviously less efficient, as experimentally reported in Fig. 3.4, and are thus expected to be more sensitive to thermal noise.

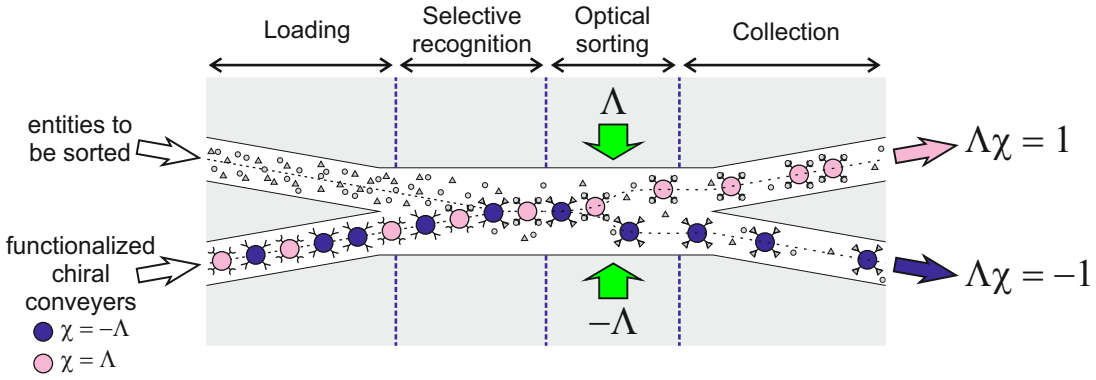

Figure 3.14: *Illustration of microfluidic optical chiral sorting concept and its application to the sorting of molecular scale entities. It relies on a random sequence of left-handed and right-handed Bragg chiral microspheres ($\chi = \pm 1$) used as "chiral conveyers" that can be separated with 100% efficiency owing to a reliable optomechanically resonant optical chiral sorting scheme. When mixed with small scale entities to be sorted, chiral conveyers with appropriate functionalization may selectively bind their (chiral or non-chiral) target in the fluidic environment, then be sorted by light and eventually collected in two different output microchannels.*

To overcome this limitation, one might consider an alternative strategy that combines robustness and efficiency of the optomechanically resonant Bragg approach with material chiral recognition applied in standard separation techniques, as sketched in Fig. 3.14. In that case, chiral microparticles act as "conveyers" whose appropriate surface functionalization allows sorting chiral or non-chiral nanometer-sized or molecular scale entities. Of course, solid Bragg chiral microparticles would be desirable for this purpose and protocols actually exist to fabricate them [71]. In addition, large-scale accurate fabrication of microscopic photopolymerized Bragg chiral conveyers can be considered by exploiting already developed microfluidic preparation protocols [72].

To conclude, the reported results represent the first-time experimental demonstration of passive optical sorting of material chirality. Since chiral sorting strategies have a huge application potential, we anticipate that this study will promote further developments of the existing optofluidic toolbox [1, 73]. This work may also contribute to the emergence of other kinds of field-induced chiral sorting strategies more generally based on the use of angular momentum of light, be it of spin or orbital nature.

CHAPTER 4

Helicity-dependent 3D optical trapping of chiral microspheres

Four decades after the first steps in optical trapping and manipulation, optomechanical effects are nowadays widely used for contact-free handling of inert or living entities from nanometric to submillimetric scale. Three-dimensional (3D) optical trapping of an object implies the use of either bell-shaped (i.e. Gaussian) or doughnut-shaped (i.e. Laguerre-Gaussian) light beams depending on (i) the relationship between the refractive indices of the object and its environment, (ii) the relationship between the object size and the beam waist, and (iii) the spatial structure of the light field itself, see the review papers [74, 75, 76, 77]. Noteworthy, neither the spin angular momentum carried by circularly polarized beams nor the orbital angular momentum carried by Laguerre-Gaussian beams are usually considered as basic ingredients for optical trapping. Indeed, the angular momentum of light has been merely used so far as a tool for addressing the rotational degrees of freedom of optically trapped transparent or absorbing objects, which may either be set into spinning and/or orbiting motions [78, 79, 80, 81, 82, 83].

In this chapter we show that chirality of light-matter interaction can act as an optomechanical trigger for the optical trapping of microparticles. More precisely we demonstrate the capability of the photon helicity Λ as a tool for selective optical trapping of transparent spherical microparticles depending on their chirality.

4.1 Concept

The proposed concept is illustrated in Fig. 1, where a transparent object of chirality $\chi = \pm 1$ interacts with an axisymmetric light field. When the given object is located at the point O, the net optical force exerted on it is zero, which refers to an equilibrium position. Helicity-dependent optical trapping implies that the light field exerts, depending on its helicity, either a non-restoring or restoring force on the chiral object displaced from the trapping location O, which in these cases corresponds to either unstable of stable equilibrium, as respectively shown in Fig. 4.1(a,b). In addition, symmetry considerations imply that the phenomenon is invariant under the simultaneous flipping of both the photon helicity and the material chirality, see Fig. 4.1(c,d).

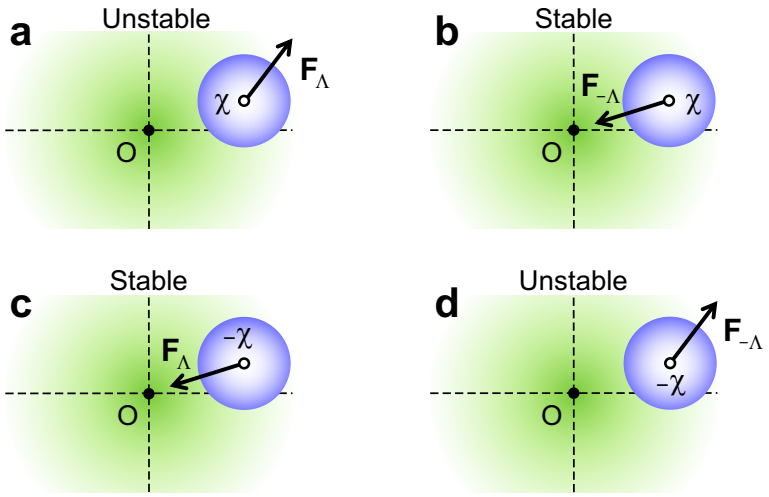

Figure 4.1: *Principle of helicity-dependent 3D optical trapping. A chiral object with chirality* $\chi = \pm 1$ *is trapped, or not, at the location O, by a light field with helicity* $\Lambda = \pm 1$*. The non-restoring (***a**, **d***) or restoring (***b**, **c***) nature of the optical force* $\mathbf{F}_{\pm\Lambda}$*, hence the stability of the optical trap, depends on the sign of the product of the helicity of light and the chirality of matter.*

Towards a practical implementation of this helicity-driven optomechanical behavior, we use chiral liquid crystal spherical droplets (see sections 1.1, 1.1.2 for details), and our choice is not incidental. Indeed, such prototypical chiral systems have stimulated a significant interest in the context of optical manipulation during the last decade [84, 85, 86] and, recently, the idea that the polarization state of light can be used as a control parameter for mechanical actions has emerged. Namely, polarization-controlled attractive-repulsive dynamics [71, 29] and polarization-controlled optical radiation pressure (see chapter 2 and [87]) have been experimentally demonstrated. Then, latter studies have respectively led to polarization-dependent angular manipulation in optical tweezers [88] and to the realization of an optofluidic sorter of material chirality driven by chiral light (see chapter 3 and [89]). Although the chirality-sensitive optical trapping remains in its infancy, yet we notice that (i) 2D trapping has been predicted (see Fig. 3.9(b,c)) and demonstrated (see Fig.3.12) in a two-beam configuration associated with a light field having mixed helicities and (ii) polarization-dependent 3D trapping in single-beam tweezers has been mentioned in [88].

In this chapter, we report on a quantitative experimental and theoretical study of 3D optical trapping of Bragg cholesteric droplets by circularly polarized Gaussian or Laguerre-Gaussian-like laser beams using a two-beam technique. In particular, this allows to consider on-demand selective trapping of chiral particles that satisfy $\Lambda\chi = +1$, $\Lambda\chi = -1$ or $\Lambda\chi = \pm 1$ whatever the particle size, thereby overcoming the stringent limitations associated with the use of single-beam opti-

cal tweezers [88]. Indeed, in [88], chiral particles that satisfy $\Lambda\chi = +1$ are always trapped, whereas particles satisfying $\Lambda\chi = -1$ can be trapped only when their radii are small enough. Namely, chiral microspheres exhibiting circular Bragg reflection escape from the beam if the radius R is a few times larger than the pitch p that characterizes the intrinsic helical structure of the material. In contrast, our results show that all types of chiral particles can be selectively 3D-trapped using an appropriate light field whatever their sizes.

4.2 Experimental approach

Our proposal for helicity-driven selective 3D optical trapping of transparent chiral particles exploits a two-beam technique allowing optical trapping at much longer working distances than those accessible to optical tweezers [74, 75, 76, 77, 78, 79, 80, 81, 82, 83]. This technique has been introduced in 1970 in order to capture transparent solid glass microspheres by a pair of counterpropagating moderately focused Gaussian beams [90, 27].

Counterpropagating schemes with high-order optical modes such as Laguerre-Gaussian beams (also known as "vortex" beams) have been proposed for trapping and manipulation of absorbing particles [91, 92]. Here we consider both options by using circularly polarized Laguerre-Gaussian beams having identical helicity Λ and either bell-shaped (fundamental mode) or doughnut-shaped (higher-order modes) transverse intensity profile. This is illustrated in Fig. 4.2(a), where the set-up is sketched and the upper and lower parts in (a) represent simulated spatial intensity distributions. Two continuous-wave laser beams with wavelength $\lambda_0 = 532$ nm are focused by means of two identical microscope objectives Thorlabs LMH-20X-532 (magnification $\times 20$, numerical aperture NA = 0.4) used in underfilling conditions. This gives the divergence angle measured as $\theta_0 \approx 5^\circ$ for both beams (see Appendix A for details), hence a beam waist radius $w_0 = \lambda/(\pi\theta_0) \approx 2$ μm in the focal plane with $D \approx 500$ μm the distance between the two focal planes.

By construction, the light-matter system possesses point symmetry when the particle is located on the beam axis at half the distance between the two focal planes, which defines the origin of the Cartesian coordinate system (x, y, z). In practice, we investigate the 3D optical trapping of transparent spherical chiral liquid crystal droplets of radius R located at the origin, where the beam waist radii are $w_1 = \theta_0 D/2 \approx 20$ μm (see Fig. 4.2(a)). The non-vortex beams correspond to the output of a single-mode optical fiber (P1-460A-FC-2 with a pair of collimation lenses F220FC-A, Thorlabs, Inc.) used as a spatial filter for the laser light, whereas the vortex beams are obtained by inserting an appropriate optical element in the path of the beam (see Appendix B for the description of the used vortex beam generator). Experimental bell-shaped and doughnut-shaped trans-

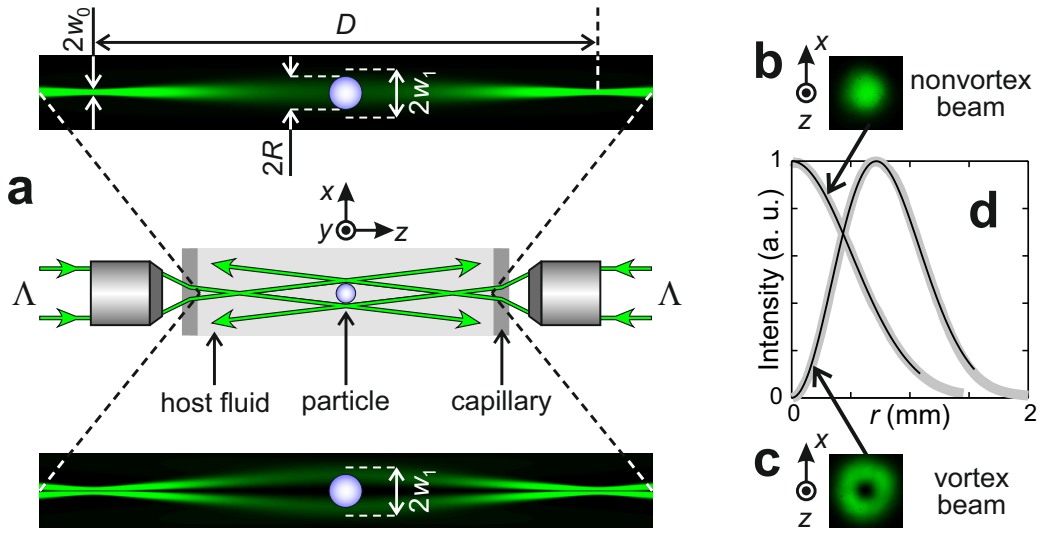

Figure 4.2: *The set-up consists of two counterpropagating moderately focused non-vortex (bell-shaped) or vortex (doughnut-shaped) beams with identical divergence angle, wavelength, helicity and power. D is the distance between the two focal planes where beam waist radius is* w_0*. (***a***) Optical trapping of a transparent spherical chiral liquid crystal droplet of radius R at the origin* $(x, y, z) = (0, 0, 0)$ *is considered in all cases. (***b**–**d***) Experimental bell- and doughnut-shaped transverse intensity distributions are shown in panels (***b**,**c***), whereas their azimuth-averaged radial profiles (thick gray lines in (***d***)) are described by the fundamental and the first-order Laguerre-Gaussian profiles (thin solid lines in (***d***)).*

verse intensity profiles are respectively displayed in Fig. 4.2(b,c). In practice, these beams can be considered as members of the family of Laguerre-Gaussian modes $\mathrm{LG}_{0\ell}$ with ℓ the topological charge of the on-axis optical phase singularity carried by the beam (see section 1.2). As shown in Fig. 4.2(d), the azimuth-averaged radial intensity profiles of the non-vortex and vortex beams measured at the entrance of the microscope objectives are well described by Eq. (1.12) with $\ell = 0$ and $|\ell| = 1$, respectively. Consequently, we will use these analytical expressions when modeling optical fields in the considered trapping scheme.

For the purpose of demonstration, the spherical microparticles used in this work are obtained by dispersing the cholesteric liquid crystal MDA-02-3211 in an isodense 27 wt% [1] aqueous glycerol solution with refractive index $n_{\mathrm{ext}} = 1.367$. Based on the characterization reported in section 1.1.2, we consider the half-apex angle of the Bragg cone $\theta_{\mathrm{B}} \approx 25°$.

[1]The previously used concentration of 25% was corrected in order to reduce the slight density mismatch, which is hard to avoid experimentally. In contrast to the studies reported in chapters 2 and 3, this mismatch is quite important in the trapping framework

4.3 Model

Following the experimental framework discussed above, the description of optical 3D trapping of a radial cholesteric droplet with chirality χ is handled by considering the interaction between two paraxial counterpropagating Laguerre-Gaussian beams $\mathrm{LG}_{0\ell}$ and a non-deformable transparent sphere of radius R endowed with helicity-dependent light scattering properties and immersed in a lossless viscous fluid with refractive index n_{ext} and dynamical viscosity η. Basic features of our theoretical approach are presented in section 1.3.

Unlike the optical sorting framework (see Fig. 3.7), the study of 3D trapping implies the analysis of optical radiation forces exerted on the droplet at an arbitrary point of the (x, y, z) coordinate system. Since the spatial intensity distribution is axisymmetric, we introduce the coordinate system $(\mathbf{u}_r, \mathbf{u}_\varphi, \mathbf{u}_z)$ that refers to the orthonormal Cartesian coordinates basis $(\mathbf{u}_x, \mathbf{u}_y, \mathbf{u}_z)$ rotated by an angle φ around the z axis, as shown in Fig. 4.3. Following these notations, the elementary optical radiation force exerted on the droplet by light impinging the surface element dS is expressed as

$$\mathbf{F}(r,\varphi,z,\theta,\phi) = -\frac{n_{\mathrm{ext}} I(\rho,\xi)\cos\theta}{\mathrm{c}} \times \left[f_\perp(\theta)\left(\cos(\phi-\varphi)\,\mathbf{u}_r + \sin(\phi-\varphi)\,\mathbf{u}_\varphi\right) + f_\parallel(\theta)\,\mathbf{z}\right] dS(\theta,\phi)\,, \quad (4.1)$$

where θ and ϕ are the polar and azimuthal angles in the spherical coordinate system originating at the droplet center,

$$I(\rho,\xi) = \frac{2^{|\ell|+1}P}{\pi|\ell|!\,w(\xi)^2}\left(\frac{\rho}{w(\xi)}\right)^{2|\ell|}\exp\left[-\frac{2\rho^2}{w(\xi)^2}\right], \quad (4.2)$$

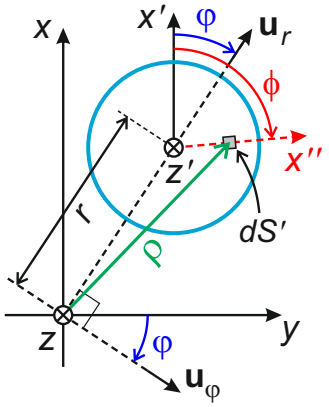

Figure 4.3: *Coordinate systems introduced in order to evaluate the helicity-dependent net optical force exerted on a droplet in the two-beam optical trapping scheme depicted in Fig. 4.2(a).*

is the spatial intensity distribution of a $LG_{0\ell}$ beam (see Eq. (1.12)), with ξ the distance from its focal plane and ρ the distance from its axis, P its total power, $w(\xi) = w_0\sqrt{1+(\xi/z_0)^2}$, w_0 the beam waist and $z_0 = \pi w_0^2/\lambda_0$ the Rayleigh range. In addition, we have

$$\rho = \left[r^2 + 2rR\sin\theta\cos(\phi-\varphi) + R^2\sin^2\theta\right]^{1/2}, \tag{4.3}$$

$$\xi = D/2 - R\cos\theta - \mathrm{sgn}(\cos\theta)z, \tag{4.4}$$

with sgn the sign function.

The net optical force $\mathbf{F} = F_r\mathbf{u}_r + F_\varphi\mathbf{u}_\varphi + F_z\mathbf{z}$ exerted on the droplet is obtained by integrating Eq. (4.1) over the spherical surface:

$$F_r(r,\varphi,z) = -\frac{n_{\mathrm{ext}}R^2}{2c}\int_0^{2\pi}\int_0^{\pi} I(\rho,\xi) f_\perp(\theta)\,\sin 2\theta\,\cos(\phi-\varphi)\,d\theta d\phi, \tag{4.5}$$

$$F_\varphi(r,\varphi,z) = 0, \tag{4.6}$$

$$F_z(r,\varphi,z) = -\frac{n_{\mathrm{ext}}R^2}{2c}\int_0^{2\pi}\int_0^{\pi} I(\rho,\xi) f_\parallel(\theta)\,\sin 2\theta\,d\theta d\phi. \tag{4.7}$$

Noticeably, the above equations lead to $\partial F_r/\partial\varphi = 0$ and $\partial F_z/\partial\varphi = 0$, as expected for an axisymmetric intensity distribution, and thus we are left with

$$\mathbf{F} = F_r(r,z)\mathbf{u}_r + F_z(r,z)\mathbf{z}. \tag{4.8}$$

4.4 Simulations

Owing to the symmetry of the light-matter system, the optical force exerted on the droplet vanishes at the origin ($r = 0, z = 0$) whatever are the parameters values. In weightless conditions, which is roughly the case in our experiments, the origin thus corresponds to the point where the droplet may be optically trapped in 3D. This occurs if both conditions $\partial F_z/\partial z < 0$ and $\partial F_r/\partial r < 0$ are fulfilled. These conditions are numerically investigated from Eqs. (4.5), (4.7) as a function of the beam divergence angle θ_0 and of the ratio w_1/R between the beam waist radius at origin and the droplet radius, for $\Lambda\chi = \pm 1$ and non-vortex ($\ell = 0$) or vortex ($\ell \neq 0$) beams. The results for $|\ell| = 0, 1, 2, 3$ are summarized in Figs. 4.4(a–d), where the existence criterion of 3D trapping in the plane of parameters $(w_1/R, \theta_0)$ is identified as colored/hatched areas. In addition, the role played by the photon helicity is emphasized by the distinction made between 3D trapping for $\Lambda\chi = +1$ alone, $\Lambda\chi = -1$ alone, and $\Lambda\chi = \pm 1$ simultaneously.

It appears from simulations that 3D trapping under both $\Lambda\chi = -1$ (that is, for chiral Bragg particles) and $\Lambda\chi = +1$ (that is, for chiral particles considered as non-chiral dielectric spheres) may be allowed whatever is ℓ depending on the used parameters. The trapping existence region, however, tends to reduce as $|\ell|$ increases as shown in Figs. 4.4(a–d). Moreover, when 3D trapping is expected to

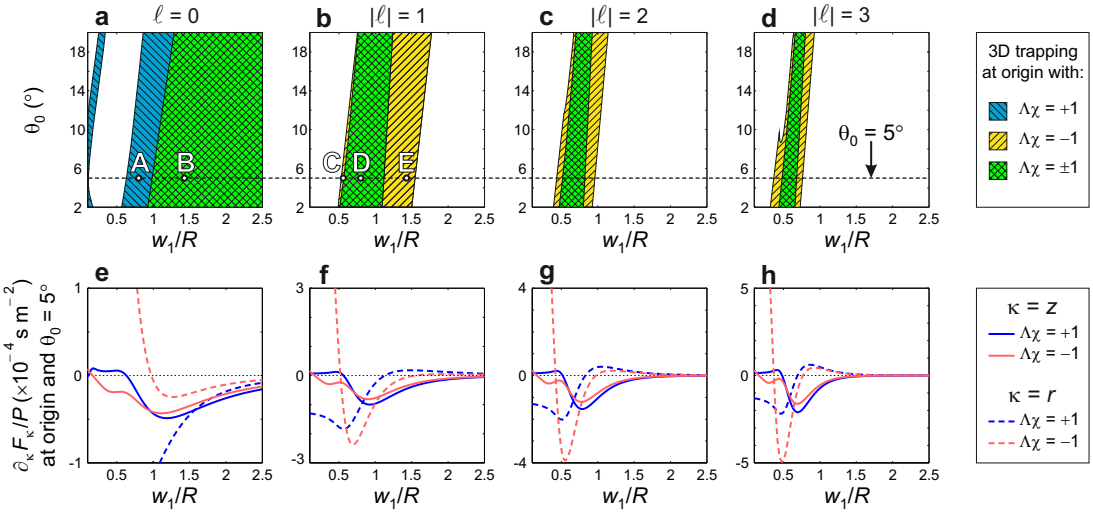

Figure 4.4: *Simulations for the helicity-dependent 3D optical trapping.* (**a**–**d**) *Existence of 3D trapping in the plane of parameters* $(w_1/R, \theta_0)$ *depending on the photon helicity for* $w_1 = 20$ *μm and* $|\ell| = 0$, *1, 2 and 3, where the material parameters values are those of our experiments. Three different colored/hatched regions refer to trapping existence for the cases* $\Lambda\chi = +1$ *alone,* $\Lambda\chi = -1$ *alone, and* $\Lambda\chi = \pm 1$ *simultaneously. Letters A, B, C, D and E correspond to the values* $w_1/R \approx 0.8$, *1.43, 0.59, 0.74 and 1.43.* (**e**–**h**) *Partial derivatives of the optical force components at origin per unit power for a beam divergence angle* $\theta_0 = 5°$.

occur simultaneously for $\Lambda\chi = \pm 1$, we note that there is a significant dependence of the trap features on the photon helicity. Indeed, the longitudinal (along z) and transverse (perpendicular to z) stiffness of the optical trap both depend on $\Lambda\chi$. This is illustrated in Figs. 4.4(e–h), where the partial derivatives of the optical force components per unit power, $\partial_\kappa F_\kappa/P$ with $\partial_\kappa(\cdot) \equiv \partial(\cdot)/\partial\kappa$ and $\kappa = (r, z)$, are shown for $\theta_0 = 5°$, which corresponds to the beam divergence used in the experiments.

4.5 Experimental validation of the model

In practice, the demonstration of helicity dependent 3D optical trapping is achieved by studying the behavior of radial cholesteric liquid crystal droplets exhibiting circular Bragg reflection at 532 nm wavelength within the introduced two-beam configuration. The demonstration consists in testing whether the optical field can trap a droplet of radius R at the origin and, if the trapping is achieved, in observing the droplet behavior after the helicity is flipped from Λ to $-\Lambda$. Two identical electrically-addressed liquid crystal variable retarders (Meadowlark Optics, Inc.) placed in the path of each of the two beams allowed us to perform the

required fast remote manipulation of the circular polarization states.

Qualitative comparison between experiments and simulations is summarized in Fig. 4.5 where the upper row displays initial trapping situations for cases A, B, C, D and E, see Fig. 4.4(a, b), which are representative of all possible predicted situations for non-vortex and vortex beams. Then, flipping the helicity of the beams from Λ to $-\Lambda$, we observe that the droplet is no longer trapped in cases A, C and E whereas it remains trapped at origin in cases B and D. All these observations agree with theoretical expectations inferred from Fig. 4.4(a, b), thereby validating the main features of the optical force field at the origin.

Since our model has been derived in a general framework, the net optical force exerted on the droplet can be evaluated for any location (r, z). This is illustrated in Fig. 4.6, where panels (a–j) correspond to the experimental situations reported in Fig. 4.5(a–j). For each situation we have calculated the net optical force which would be exerted on the droplet if it was located at a point around the origin with $-3R < r < 3R$ and $-3R < z < 3R$. As one can see, the theoretical vector plots in Fig. 4.6 confirm the practically observed behavior of the tested droplets.

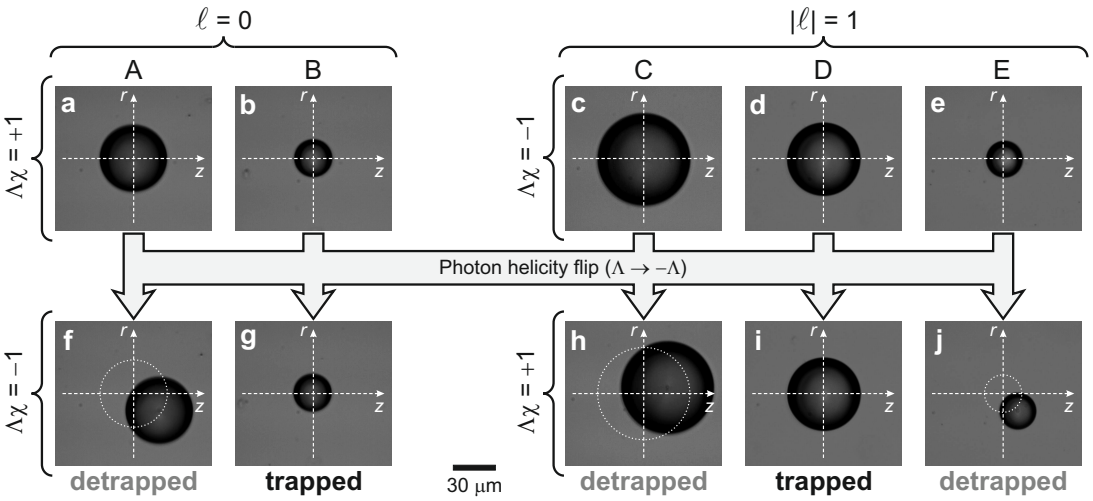

Figure 4.5: *Observations of the helicity-dependent 3D optical trapping. (***a**–**e***) Snapshots of radial cholesteric droplets optically trapped at origin under power $P \approx 50$ mW in situations tagged by the letters A, B, C, D and E in Fig. 4.4(a,b), which respectively correspond to $w_1/R \approx 0.8$, 1.43, 0.59, 0.74 and 1.43. Situations A and B correspond to Gaussian beams with $\Lambda\chi = +1$ (***a**,**b***) whereas C, D and E refer to first-order Laguerre-Gaussian beams with $\Lambda\chi = -1$ (***c**–**e***). For $\ell = 0$, helicity flip leads to detrapping of the larger droplet (***f***), whereas the smaller one is kept trapped at the origin (***g***). For $|\ell| = 1$, helicity flip leads to detrapping for both the larger and the smaller droplets (***h**,**j***) whereas the droplet with intermediate size remains trapped at the origin (***i***).*

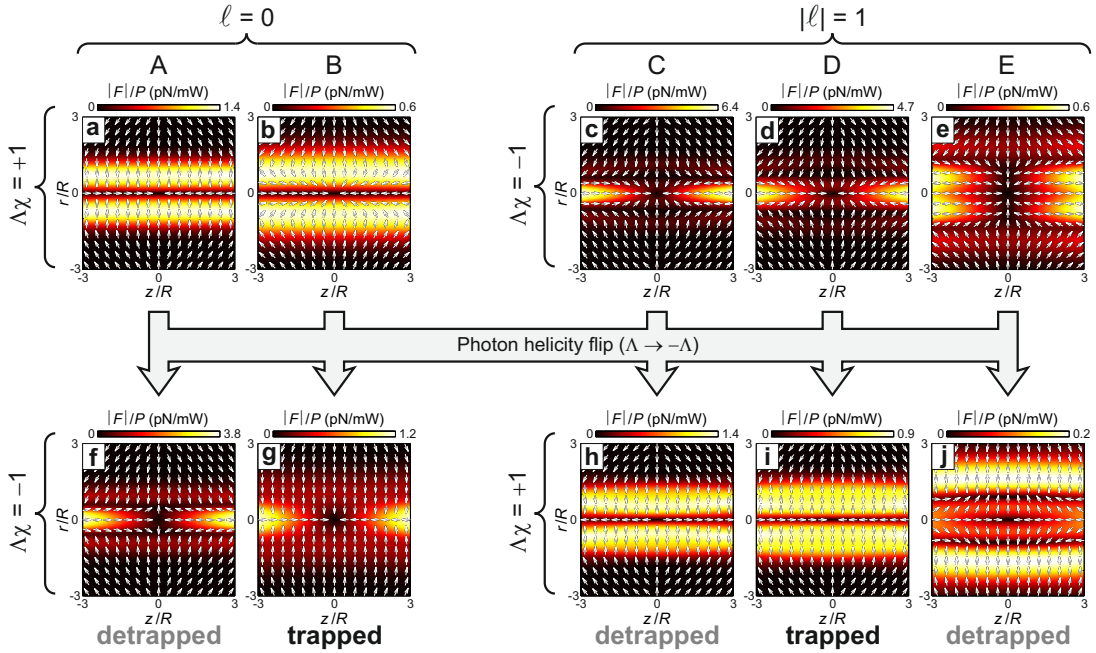

Figure 4.6: *(**a**–**j**) Theoretical plots corresponding to the experimental situations presented in Fig. 4.5(a–j). Absolute values of the net optical force (divided by optical power P) at every point is expressed by the surface plots with colorbars. Each arrow indicates the direction of the optical force which would be exerted on the droplet if it was located at that point.*

4.6 3D optical force field quantitative analysis

Quantitative analysis is done for two representative cases – one for non-vortex and one for vortex beams – that lead to stable 3D trapping at the origin, namely:

- $\{\ell = 0, \Lambda\chi = +1, w_1/R = 2/3\}$ and
- $\{|\ell| = 1, \Lambda\chi = -1, w_1/R = 1\}$,

with $\theta_0 = 5°$ and $w_1 = 20$ μm. These situations actually correspond to cases A and D in Fig. 4.4. The results of simulations are presented in Fig. 4.7(a,b), where arrows indicate the direction of the optical force, while color maps refer to the force magnitude.

That said, we note that the setting up of a quantitative assessment may benefit from the symmetries of the light-matter system, which imply $F_r(0, z) = 0$ and $F_z(r, 0) = 0$. Indeed, this allows the independent study of (i) the axial force F_z along the z axis and (ii) the radial force F_r in a direction perpendicular to z passing through the origin.

In practice, the force field is retrieved by recording the motion of the droplet. In the limit of small Reynolds number, as is the case in our experiments, the

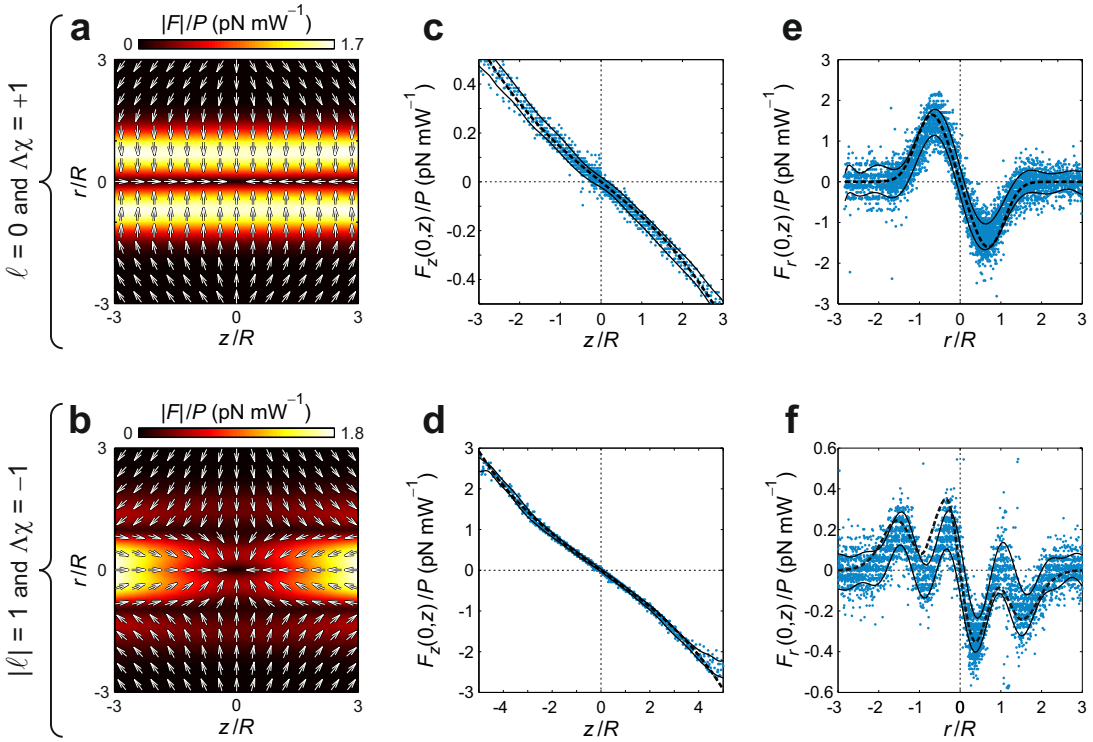

Figure 4.7: *Quantitative analysis of 3D optical force fields.* (**a**,**b**) *Spatial distribution of the magnitude (colormap) and orientation (vector plot) of the calculated optical force exerted on a droplet located around the origin, namely* $-3R < z < 3R$ *and* $-3R < r < 3R$, *for* $\{\ell = 0, \Lambda\chi = +1, w_1/R = 2/3\}$ *and* $\{|\ell| = 1, \Lambda\chi = -1, w_1/R = 1\}$, *with* $\theta_0 = 5°$ *and* $w_1 = 20$ μm. (**c**,**d**) *Experimental data for the longitudinal component of the force along the* z *axis,* $F_z(0,z)$. **e**,**f** *Experimental data for the transverse component of the force along the axis* r *that passes through the origin,* $F_r(r,0)$. *Experimental conditions: the experimental data set (dot markers) corresponds to 40 independent realizations, whose standard deviation range is indicated by solid curves whereas dashed curves are the results of simulations without adjustable parameters. Upper panels correspond to* $P \approx 20$ mW *and* $R = 29$ μm *whereas bottom panels refer to* $P \approx 70$ mW *and* $R = 20$ μm. *The constant drag velocity for radial force measurements is* $V_0 = 36$ $\mu m\ s^{-1}$, *see text for details.*

expression for the light-induced droplet velocity is obtained from the balance between the viscous force exerted by the surrounding fluid on the moving droplet and the driving optical force. Namely $F_\kappa(r,z) = 6\pi\eta R v_\kappa(r,z)$ with $\eta = 2$ mPa s. In addition, we apply different strategies for the measurements of F_z and F_r.

On one hand, concerning F_z, a droplet initially trapped at the origin is optically displaced along z by turning off one of the two beams. When being restored, the optical field guides the droplet back to the origin where it is trapped again.

The recorded droplet motion gives access to the velocity v_z along the z axis, hence to the force $F_z(0,z)$. The reverse procedure then completes the analysis.

On the other hand, motivated by the fact that there is no all-optical way to displace at will the droplet in a direction perpendicular to z with the two trapping beams, we use an alternative approach to measure $F_r(r,0)$. It consists in using a droplet as an optomechanical probe in order to map the force field. Namely, the capillary is dragged at a constant velocity V_0 along r at $z = 0$ so that the immersed droplet moves in a direction perpendicular to z passing through the origin. The recorded motion of the droplet thus gives the net velocity $V_r(r,0) = V_0 + v_r(r,0)$, from which we extract $F_r(r,0) = 6\pi\eta R v_r(r,0)$.

Following the above protocols, data have been collected for 40 independent realizations. The results for $F_z(0,z)$ are shown in Figs. 4.7(c,d) for $\ell = 0$ and $|\ell| = 1$ whereas those for $F_r(r,0)$ are shown in Figs. 4.7(e,f) for $\ell = 0$ and $|\ell| = 1$, see dot markers. Recalling that there is no adjustable parameters in our model, the comparison with simulations (dashed curves) gives a satisfying agreement with the data, whose standard deviation range is indicated by solid curves.

4.7 Discussion and outlook

As shown above, our weightless model provides an appropriate description of the experimental data. However, we stress that the isodense framework has been merely chosen in order to ease the practical implementation rather than being a necessary condition to observe helicity-dependent 3D optical trapping. To prove it, we have calculated the equilibrium position of the droplet for the two situations presented in Fig. 4.7 but accounting for a mismatch between the density of the particle, ρ_{part} and that of the external fluid, ρ_{ext}. The gravitational acceleration is taken along x as is the case in practice. The results are presented in Fig. 4.8, where the dependence of the magnitude of the x coordinate of the equilibrium positions $(x_{\mathrm{eq}},0)$ is shown as a function of the density mismatch $|\Delta\rho| = |\rho_{\mathrm{part}} - \rho_{\mathrm{ext}}|$ per unit power. Solid curves refer to 3D optical trapping whereas dotted ones correspond to 2D trapping, the equilibrium position being unstable in the z direction.

The above analysis emphasizes that chiral Bragg particle can be easily trapped in 3D by contra-propagating vortex beams over a wide range of $|\Delta\rho|$. For instance, a pair of LG_{01} beams with $P = 1$ W should trap a Bragg-reflecting sphere with density up to 1.3 g cm^{-3} in the air. This might be explored by using solidified radial cholesteric microspheres [71] instead of liquid ones. In contrast, the Gaussian beam trapping of usual non-Bragg particles is characterized with more stringent density mismatch restrictions. Indeed, for $\ell = 0$ and present beam parameters, a non-Bragg particle could be 3D trapped if $|\Delta\rho|/P < 0.04$ g cm^{-3} W^{-1}. Such a condition is easily fulfilled in practice since the host fluid density can be tuned

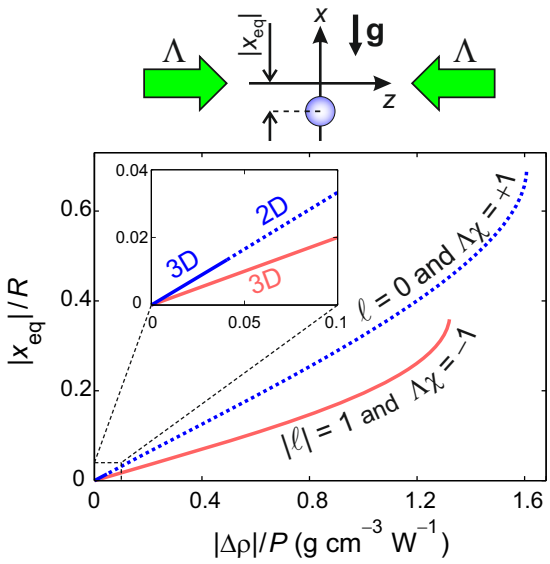

Figure 4.8: *Simulated equilibrium position of a chiral microparticle irradiated by two counterpropagating beams as a function of density mismatch between the particle and the host medium. Optical and material parameters (except for the actual droplet density) are those used in the experiments. Solid curves correspond to 3D optical trapping whereas dotted ones refer to 2D trapping of the particle in the $z = 0$ plane and unstable trapping along z.*

with 10^{-3} g cm^{-3} accuracy by adjusting the glycerol concentration.

To conclude, in this chapter we demonstrated both experimentally and theoretically that the photon helicity can be used as a trigger to optically trap, in three dimensions and in a selective manner, chiral particles with non-chiral morphology. The driving mechanism consists in actuation of the material translational degrees of freedom by the intrinsic rotational ones of light. Present concept, whose demonstration addresses the case of spherical chiral particles, might be extended to non-chiral material objects endowed with chiral morphology by using orbital angular momentum instead of spin angular momentum of light as a control parameter. To this aim, the orbital counterpart of the circular Bragg reflection phenomenon might be worth considering, see [93] and references therein.

Moreover, although present results concern a given chiral material system explored at the $1 - 100\,\mu$m scale, combination of our experimental results with several recent theoretical studies on helicity-dependent optomechanics at the submicrometer scale [66, 67, 94, 95] should motivate the development of optomechanical strategies for selective optical trapping and manipulation of chiral objects whose application potential is multidisciplinary by nature.

Conclusions and perspectives

The rule of thumb of tailored optical forces consists in the control of linear momentum exchange between light and matter. This may be done by appropriate selection of the interaction geometry, optical modes or environmental characteristics. In this thesis we have revealed that the interplay of the helicity of light and the chirality of matter turns the photon spin angular momentum into an efficient tool for controllable trapping and manipulation of chiral material objects by light.

We have successively demonstrated the helicity-controlled displacement, spatial separation and selective three-dimensional trapping of transparent chiral microspheres by chiral light. These results have led to the publication of three articles, namely [87, 89] and [96](in press). In the reported experimental schemes we have used the circular Bragg phenomenon in order to enhance the chiral light-matter interaction benefiting from the optomechanical resonance. However, as we have shown experimentally in the context of optical chiral sorting, the proposed concepts are not restricted to optomechanically resonant chiral interaction. In fact, we believe that the principle of helicity-controlled optical manipulation is applicable to any kind of chiral objects. For instance, to circularly birefringent or circularly dichroic solids or fluids, as well as material systems with morphological chirality.

Our findings, though providing comprehensive resolution of the assigned tasks, are quite fruitful in terms of new ideas for future research projects. One of them concerns the photon's orbital angular momentum, which is also a manifestation of the chirality of light and may be used as a control parameter for realization of chiral sorting and trapping strategies.

Another interesting issue not addressed in this thesis is related to the possible actuation of the rotational degree of freedom of a chiral microparticle interacting with chiral light. Indeed, the circular Bragg phenomenon widely applied in our studies is famous for flipping the spin angular momentum of the photons experiencing the resonant reflection from a helically-structured anisotropic object. According to the law of conservation of angular momentum, the object acquires a light-induced torque. Therefore, if the object is free to rotate, it will be set into a spinning motion, similar to the already realized situations when an object is optically spun due to transformation of the photon spin angular momentum as a result of absorption [79] or transmission through a birefringent medium [97, 78]. Light induced rotation of a chiral object exhibiting the circular

Bragg phenomenon thus completes the picture by using the spin transformation by reflection of light.

In order to realize this idea, one could suggest to trap a radial cholesteric droplet using a doughnut-shaped optical field as discussed in chapter 4. However, the experiments presented there deal with counterpropagating beams with identical geometrical parameters, helicity and power. This prevents from a non-zero net deposition of spin angular momentum since any contribution of one beam is balanced by the contribution of the second beam, although each beam independently deposits spin angular momentum when circular Bragg reflection takes place. Regarding the transfer of orbital angular momentum from light to matter, it vanishes when the droplet lies on the beam axes by virtue of axisymmetry. Consistently, we found no experimental indication of neither spinning nor orbiting motion for all studied trapping events. Instead, we think that a single-beam scheme, where a Bragg-reflecting droplet is levitated by a divergent vortex beam, is a good option for realization of the idea of a tangible object optically spun by reflection of light. Actually, preliminary experimental studies, not reported in this manuscript, have already been made in that direction.

Moreover, in the work reported in this manuscript, radial cholesteric droplets have been used as a convenient tool for experimental demonstrations of the proposed optomechanical strategies, whereas the physical properties of such a natural helically-structured supramolecular system are expected to offer a playground for the demonstration of novel optical phenomena. In particular, the presence of a characteristic radial defect in radial cholesteric droplets may cause some unexpected optomechanical effects or singular beam transformations.

To sum up, the results presented in this thesis not only bring a new twist to the existing optomechanical toolbox, but also suggest prospective research directions in the field of optical manipulation of chiral matter.

APPENDIX A

Beam divergence estimation

The parameters of the Gaussian and Laguerre-Gaussian beams used in this study were measured via numerical analysis of the beam spots captured by a CCD Camera Beam Profiler BC106-VIS from Thorlabs, Inc. The obtained images were analyzed using the MATLAB software environment, which allows to measure the relative optical intensity, ranging from 0 to 255 units, for every pixel. Then azimuthally averaged radial intensity distribution of was fitted using Eq. (1.12) with the corresponding geometrical parameters and the topological charge.

Fig. A.1 demonstrates the result of measurements of the beam divergence θ_0 for one of the vortex beams used in the trapping set-up (see Fig. 4.2(a)). The z coordinate was determined by the translational stage on which the beam profiler was fixed, whereas the beam radius $w(z)$ was obtained from the fit of the intensity profile by means of Eq. (1.12) with $|\ell| = 1$.

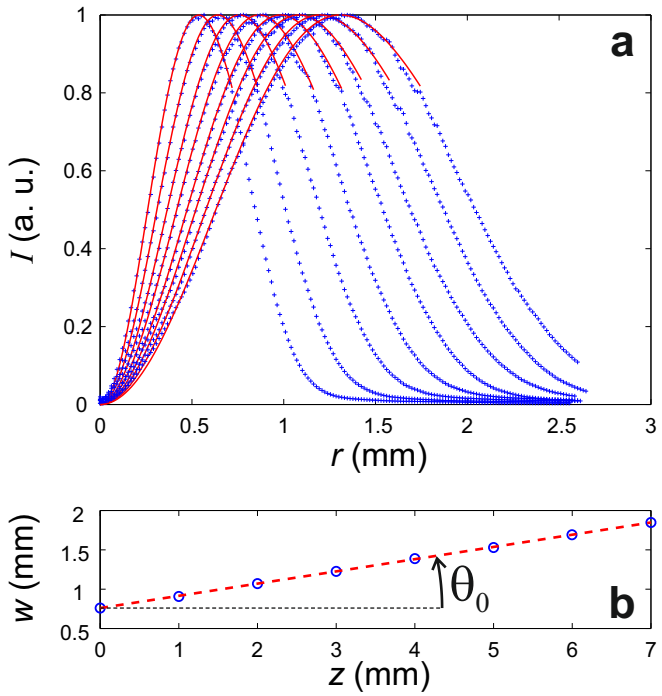

Figure A.1: *Estimation of the divergence angle θ_0 of a vortex beam used in the set-up desctibed in chapter 4.* (**a**) *Measured (markers) and fitted (solid lines) azimuthally average intensity distributions for various relative z coordinate.* (**b**) *The fitted beam radii versus the relative z coordinate, plotted at an equal scale so that one could see the actual divergence angle.*

APPENDIX B

Generation of vortex beams

Optical vortex beams used in chapter 4 are obtained from Gaussian beams by using space-variant birefringent elements that consist of transparent planar slabs having a homogeneous birefringent phase retardation of π (half-wave) and azimuthally varying orientation of the optical axis lying in the slab plane. This orientation is characterized by the angle

$$\alpha(r,\varphi) = m\varphi\,, \tag{B.1}$$

where r,φ are polar coordinates in the plane of the slab and m is half-integer. Let us consider the effect of such an optical element on a circularly polarized plane wave. The input electric field can be described by the Jones vector [98]

$$\mathbf{E}_{\text{in}} = E_0 \begin{pmatrix} 1 \\ \sigma i \end{pmatrix}, \tag{B.2}$$

where E_0 is the field amplitude, $\sigma = \pm 1$ corresponds to left/right-handed circular polarization state. The output light is then obtained by considering the Jones matrix $\mathbf{M}$ that characterizes the propagation through the plate. Up to an unimportant overall phase factor, the latter matrix expresses as

$$\mathbf{M} = \begin{pmatrix} \cos 2\alpha & \sin 2\alpha \\ \cos 2\alpha & -\sin 2\alpha \end{pmatrix}. \tag{B.3}$$

This gives an output light field of the form (up to an unimportant overall phase factor):

$$\mathbf{E}_{\text{out}} = \mathbf{M}\mathbf{E}_{\text{in}} = E_0 \mathrm{e}^{i2\alpha} \begin{pmatrix} 1 \\ -\sigma i \end{pmatrix} = E_0 \mathrm{e}^{i2\sigma m\varphi} \begin{pmatrix} 1 \\ -\sigma i \end{pmatrix}. \tag{B.4}$$

Consequently, the output wave carries the phase singularity of the topological charge $\ell = 2\sigma m$ and has opposite helicity with respect to the input one.

In practice, we used space-variant birefringent optical vortex generators from Altechna R & D that are represented by nanostructured glass plates fabricated by direct femtosecond laser writing of the form birefringence. Fig. B.1 demonstrates the anisotropy distribution (panels (a–c), local orientation of the optical axis is indicated by line bars) and XPOL images (panels (d–f), where orientation of linear polarizers at the input and output of the plate are shown by the crossed

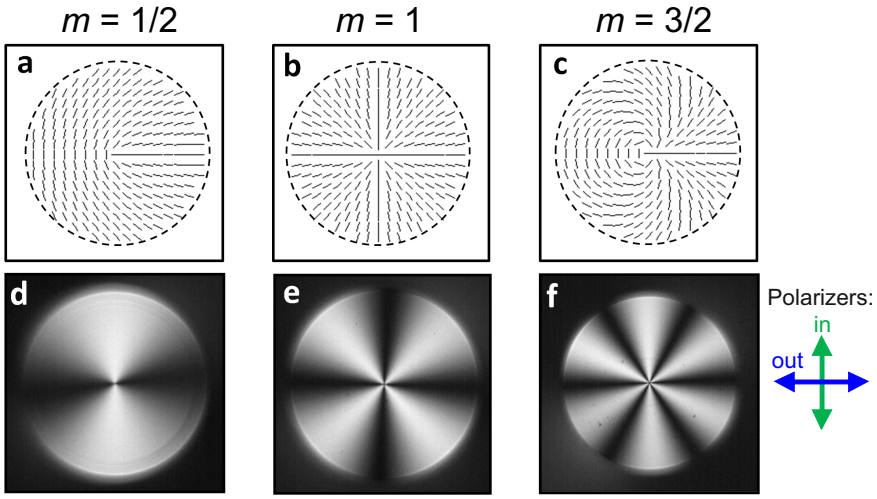

Figure B.1: *(**a**–**c**) Anisotropy of q-plates from Altechna R & D. (**d**–**f**) Transmission images between crossed polarizers ("in" and "out") demonstrate characteristic 4m-fold patterns.*

arrows) of the plates having $m = 1/2, 1, 3/2$. In our experiments the plate with $m = 1/2$ was centered on the axis of a normally incident circularly polarized collimated Gaussian beam, which led to generation of a vortex beam with topological charge $\ell = \pm 1$.

Bibliography

[1] A. Jonas and P. Zemanek, "Light at work: The use of optical forces for particle manipulation, sorting, and analysis", *Electrophoresis* **29**, 4813 (2008).

[2] P. Lebedew, "Untersuchungen über die Druckkräfte des Lichtes", *Ann. Phys.* **6**, 433 (1901).

[3] E. F. Nichols and G. F. Hull, "A preliminary communication on the pressure of heat and light radiation", *Phys. Rev.* **13**, 307 (1901).

[4] A. Ashkin and J. M. Dziedzic, "Radiation pressure on a free liquid surface", *Phys. Rev. Lett.* **30**, 139 (1973).

[5] J. D. Jackson, *Classical electrodynamics* (Wiley: New York, 1998).

[6] D. Griffiths, *Introduction to elementary particles* (Wiley: New York, 1987).

[7] M. Faryad and A. Lakhtakia, "The circular Bragg phenomenon", *Advances in Optics and Photonics* 225 (2014).

[8] P. Oswald and P. Pieransky, *Nematic and Cholesteric Liquid Crystals: Concepts and Physical Properties Illustrated by Experiments* (Taylor & Francis, CRC, Boca Raton, FL, 2005).

[9] M. Born and E. Wolf, *Principles of Optics* (Pergamon, 2005).

[10] J. Li, C.-H. Wen, S. Gauza, R. Lu, , and S.-T. Wu, "Refractive Indices of Liquid Crystals for Display Applications", *IEEE/OSA Journal of display technology* 51 (2005).

[11] E. Hecht, *Optics* (Addison-Wesley, 2001).

[12] F. Xu and P. P. Crooker, "Chiral nematic droplets with parallel surface anchoring", *Phys. Rev. E* **56**, 6853 (1997).

[13] J. Bezic and S. Zumer, "Structures of the cholesteric liquid crystal droplets with parallel surface anchoring", *Liq. Cryst.* **11**, 593 (1992).

[14] D. Sec, T. Porenta, M. Ravnik, and S. Zumer, "Geometrical frustration of chiral ordering in cholesteric droplets", *Soft Matter* **8**, 11982 (2012).

[15] M. Eisenberg and R. Guy, "A Proof of the Hairy Ball Theorem", *The American Mathematical Monthly* 571 (1979).

[16] A. E. Siegman, *Lasers* (University Science Books, 1986).

[17] L. Allen, S. M. Barnett, and M. J. Padgett, *Optical angular momentum* (Institute of Physics Publishing, 2003).

[18] K. T. Gahagan and J. G. A. Swartzlander, "Optical vortex trapping of particles", *Opt. Lett.* 827 (1996).

[19] V. A. Belyakov, V. E. Dmitrienko, and V. P. Orlov, "Optics of cholesteric liquid crystals", *Sov. Phys. Usp.* **22**, 64 (1979).

[20] Q. Hong, T. X. Wu, and S. T. Wu, "Optical wave propagation in a cholesteric liquid crystal using the finite element method", *Liq. Cryst.* **30**, 367 (2003).

[21] D. V. Guzatov and V. V. Klimov, "Chiral particles in a circularly polarised light field: new effects and applications", *Quantum Electron.* **41**, 526 (2011).

[22] Z.-S. Wu, Q.-C. Shang, and Z.-J. Li, "Calculation of electromagnetic scattering by a large chiral sphere", *Appl. Opt.* **51**, 6661 (2012).

[23] J. Z. Zhang and R. K. Chang, "Shape distortion of a single water droplet by laser-induced electrostriction", *Opt. Lett.* **13**, 916 (1988).

[24] R. V. Jones and J. C. S. Richards, "The pressure of radiation in a refracting medium", *Proc. R. Soc. Lond. A* **221**, 480 (1954).

[25] R. V. Jones and B. Leslie, "The measurement of optical radiation pressure in dispersive media", *Proc. R. Soc. Lond. A* **360**, 347 (1978).

[26] B. A. Kemp and T. M. Grzegorczyk, "The observable pressure of light in dielectric fluids", *Opt. Lett.* **36**, 493 (2011).

[27] G. Roosen and C. Imbert, "Optical levitation by means of two horizontal laser beams: a theoretical and experimental study", *Phys. Lett.* **59A**, 6 (1976).

[28] A. Ashkin, "Forces of a single-beam gradient laser trap on a dielectric sphere in the ray optics regime", *Biophys. J.* **61**, 569 (1992).

[29] R. J. Hernandez, A. Mazzulla, A. Pane, K. Volke-Sepulveda, and G. Cipparrone, "Attractive-repulsive dynamics on light-responsive chiral microparticles induced by polarized tweezers", *Lab. Chip* **13**, 459 (2013).

[30] S.-T. Wu and K.-C. Lim, "Absorption and scattering measurements of nematic liquid crystals", *Appl. Opt.* **26**, 1722 (1987).

[31] G. P. Association, Physical Properties of Glycerine and Its Solutions, 1963.

[32] R. Wunenburger, B. Issenmann, E. Brasselet, C. Loussert, V. Hourtane, and J.-P. Delville, "Fluid flows driven by light scattering", *J. Fluid Mech.* **666**, 273 (2011).

[33] G. M. Hale and M. R. Querry, "Optical constants of water in the 200-nm to 200-μm wavelength region", *Appl. Opt.* **12**, 555 (1973).

[34] E. J. G. Peterman, F. Gittes, and C. F. Schmidt, "Laser-Induced Heating in Optical Traps", *Biophysical Journal* 1308 (2003).

[35] G. K. Batchelor, *An introduction to fluid mechanics* (Cambridge University Press, 2000).

[36] C. G. Kartha and R. K. L. P. Agrawal, "Viscous behaviour of cholesteric liquid crystals", *Journal of the physical society of Japan* 470 (1970).

[37] Y.-X. Huang and M. Tu, "Dependence of viscoelastic parameters of nematic liquid crystals on pretilt angle and temperature", *Current Applied Physics* 561 (2010).

[38] Q. Liu, T. Asavei, T. Lee, H. Rubinsztein-Dunlop, S. He, and I. I. Smalyukh, "Measurement of viscosity of lyotropic liquid crystals by means of rotating laser-trapped microparticles", *Optics Express* 25134 (2011).

[39] N. S. Cheng, "Formula for viscosity of glycerol-water mixture", *Ind. Eng. Chem. Res.* **47**, 3285 (2008).

[40] Z.-G. Feng, E. E. Michaelides, and S. Mao, "On the drag force of a viscous sphere with interfacial slip at small but finite Reynolds numbers", *Fluid Dyn. Res.* **44**, 025502 (2012).

[41] B. M. Ross and A. Lakhtakia, "Light pressure on chiral sculptured thin films and the circular Bragg phenomenon", *Optik* **119**, 7 (2008).

[42] T. Imasaka, Y. Kawabata, T. Kaneta, and Y. lshidru, "Optical chromatography", *Anal. Chem.* **67**, 1763 (1995).

[43] V. Petrov, J. Hahn, J. Petter, M. Petrov, and T. Tschudi, "Precise subnanometer control of the position of a macro object by light pressure", *Opt. Lett.* **30**, 3138 (2005).

[44] G. A. Swartzlander, T. J. Peterson, A. B. Artusio-Glimpse, and A. D. Raisanen, "Stable optical lift", *Nature Photon.* **5**, 48 (2010).

[45] G. Gübitz and M. G. Schmid, "Chiral Separation Principles in Chromatographic and Electromigration Techniques", *Molecular Biotechnology* **32**, 159 (2006).

[46] T. J. Ward and B. A. Baker, "Chiral separations", *Anal. Chem.* **80**, 4363 (2008).

[47] Y. Pomeau, "Phénomènes de transport pour des molécules optiquement actives", *Phy. Lett.* **34A**, 143 (1971).

[48] Y.-J. Kim and W. Rae, "Separation of screw-sensed particles in a homogeneous shear field", *Int. J. Multiphase Flow* **17**, 717 (1991).

[49] M. Makino and M. Doi, "Migration of twisted ribbon-like particles in simple shear flow", *Phys. Fluids* **17**, 103605 (2005).

[50] M. Kostur, M. Schindler, P. Talkner, and P. Hanggi, "Chiral Separation in Microflows", *Phys. Rev. Lett.* **96**, 014502 (2006).

[51] R. Eichhorn, "Microfluidic sorting of stereoisomers", *Phys. Rev. Lett.* **105**, 034502 (2010).

[52] R. Eichhorn, "Enantioseparation in microfluidic channels", *Chem. Phys.* **375**, 568 (2010).

[53] S. Meinhardt, J. Smiatek, R. Eichhorn, and F. Schmid, "Separation of Chiral Particles in Micro- or Nanofluidic Channels", *Phys. Rev. Lett.* **108**, 214504 (2012).

[54] D. Speer, R. Eichhorn, and P. Reimann, "Exploiting Lattice Potentials for Sorting Chiral Particles", *Phys. Rev. Lett.* **105**, 090602 (2010).

[55] Marcos, H. C. Fu, T. R. Powers, and R. Stocker, "Separation of Microscale Chiral Objects by Shear Flow", *Phys. Rev. Lett.* **102**, 158103 (2009).

[56] L. Bogunovic, M. Fliedner, R. Eichhorn, S. Wegener, J. Regtmeier, D. Anselmetti, and P. Reimann, "Chiral Particle Separation by a Nonchiral Microlattice", *Phys. Rev. Lett.* **109**, 100603 (2009).

[57] M. Aristov, R. Eichhornb, and C. Bechinger, "Separation of chiral colloidal particles in a helical flow field", *Soft Matter* **9**, 2525 (2013).

[58] N. B. Baranova and B. Y. Zel'dovich, "Separation of mirror isomeric molecules by radio-frequency electric field of rotating polarization", *Chem. Phys. Lett.* **57**, 435 (1978).

[59] Y. Pomeau, "Séparation physique de molécules chirales", *C. R. Physique* **3**, 1269 (2002).

[60] D. Schamel, M. Pfeifer, J. G. Gibbs, B. Miksch, A. G. Mark, and P. Fischer, "Chiral Colloidal Molecules And Observation of The Propeller Effect", *J. Am. Chem. Soc.* **135**, 12353 (2013).

[61] Editorial, "Fluidic vision", *Nature Photon.* **5**, 567 (2011).

[62] Y. Li, C. Bruder, and C. Sun, "Generalized Stern-Gerlach effect for chiral molecules", *Phys. Rev. Lett.* **99**, 130403 (2007).

[63] B. Spivak and A. Andreev, "Photoinduced Separation of Chiral Isomers in a Classical Buffer Gas", *Phys. Rev. Lett.* **102**, 063004 (2009).

[64] X. Li and M. Shapiro, "Spatial separation of enantiomers by coherent optical means", *J. Chem. Phys.* **132**, 041101 (2010).

[65] X. Li and M. Shapiro, "Theory of the spatial separation of racemic mixtures of chiral molecules", *J. Chem. Phys.* **132**, 194315 (2010).

[66] A. Canaguier-Durand, J. A. Hutchison, C. Genet, and T. W. Ebbesen, "Mechanical separation of chiral dipoles by chiral light", *New J. Phys.* **15**, 123037 (2013).

[67] R. P. Cameron, S. M. Barnett, and A. M. Yao, "Discriminatory optical force for chiral molecules Robert P", *New J. Phys.* **16**, 013020 (2014).

[68] A. Lakhtakia, V. V. Varadan, and V. K. Varadan, "Reflection of plane waves at planar achiral-chiral interfaces: independence of the reflected polarization state from the incident polarization state", *Opt. Express* **7**, 1654 (1990).

[69] Q.-C. Shang, Z.-S. Wu, T. Qu, Z.-J. Li, L. Bai, and L. Gong, "Analysis of the radiation force and torque exerted on a chiral sphere by a Gaussian beam", *Opt. Express* **21**, 8677 (2013).

[70] J. Peláez and M. Wilson, "Molecular orientational and dipolar correlation in the liquid crystal mixture E7: a molecular dynamics simulation study at a fully atomistic level", *Phys. Chem. Chem. Phys.* 2968 (2007).

[71] G. Cipparrone, A. Mazzulla, A. Pane, R. J. Hernandez, and R. Bartolino, "Chiral Self-Assembled Solid Microspheres: A Novel Multifunctional Microphotonic Device", *Adv. Mater.* **23**, 5773 (2011).

[72] A. Fernandez-Nieves, G. Cristobal, V. Garces-Chavez, G. C. Spalding, K. Dholakia, and D. Weitz, "Optically anisotropic colloids of controllable shape", *Adv. Mater.* **17**, 680 (2005).

[73] L. Pang, H. M. Chen, L. M. Freeman, and Y. Fainman, "Optofluidic devices and applications in photonics, sensing and imaging", *Lab. Chip* **12**, 3543 (2012).

[74] D. G. Grier, "A revolution in optical manipulation", *Nature* **424**, 810 (2003).

[75] M. Padgett and R. Bowman, "Tweezers with a twist", *Nature Photon.* **5**, 343 (2011).

[76] R. W. Bowman and M. J. Padgett, "Optical trapping and binding", *Rep. Prog. Phys.* **76**, 026401 (2013).

[77] M. Woerdemann, C. Alpmann, M. Esseling, and C. Denz, "Advanced optical trapping by complex beam shaping", *Laser Photonics Rev.* **7**, 839 (2013).

[78] M. E. J. Friese, T. A. Nieminen, N. R. Heckenberg, and H. Rubinsztein-Dunlop, "Optical alignment and spinning of laser-trapped microscopic particles", *Nature* **394**, 348 (1998).

[79] M. E. J. Friese, J. Enger, H. Rubinsztein-Dunlop, and N. R. Heckenberg, "Optical angular-momentum transfer to trapped absorbing particles", *Phys. Rev. A* **54**, 1593 (1996).

[80] M. E. J. Friese, T. A. Nieminen, N. R. Heckenberg, and H. Rubinsztein-Dunlop, "Optical torque controlled by elliptical polarization", *Opt. Lett.* **23**, 1 (1998).

[81] H. He, M. E. J. Friese, N. R. Heckenberg, and H. Rubinsztein-Dunlop, "Direct observation of transfer of angular momentum to absorptive particles from a laser beam with a phase singularity", *Phys. Rev. Lett.* **75**, 826 (1995).

[82] N. B. Simpson, K. Dholakia, L. Allen, and M. J. Padgett, "Mechanical equivalence of spin and orbital angular momentum of light: an optical spanner", *Opt. Lett.* **22**, 52 (1997).

[83] Y. Arita, M. Mazilu, and K. Dholakia, "Laser-induced rotation and cooling of a trapped microgyroscope in vacuum", *Nat. Commun.* **4**, 2374 (2014).

[84] H. F. Gleeson, T. A. Wood, and M. Dickinson, "Laser manipulation in liquid crystals: an approach to microfluidics and micromachines", *Phil. Trans. R. Soc. A* **364**, 2789 (2006).

[85] Y. Yang, P. D. Brimicombe, N. W. Roberts, M. R. Dickinson, M. Osipov, and H. F. Gleeson, "Continuously rotating chiral liquid crystal droplets in a linearly polarized laser trap", *Opt. Express* **16**, 6877 (2008).

[86] M. Mosallaeipour, Y. Hatwalne, N. V. Madhusudana, and S. Ananthamurthy, "Laser induced rotation of trapped chiral and achiral nematic droplets", *Journal of Modern Optics* 395 (2010).

[87] G. Tkachenko and E. Brasselet, "Spin controlled optical radiation pressure", *Phys. Rev. Lett.* **111**, 033605 (2013).

[88] M. Donato *et al.*, "Polarization-dependent optomechanics mediated by chiral microresonators", *Nat. Commun.* **5**, 3656 (2014).

[89] G. Tkachenko and E. Brasselet, "Optofluidic chiral sorting of material chirality by chiral light", *Nat. Commun.* **5**, 3577 (2014).

[90] A. Ashkin, "Acceleration and Trapping of Particles by Radiation Pressure", *Phys. Rev. Lett.* **24**, 156 (1970).

[91] V. G. Shvedov, A. S. Desyatnikov, A. V. Rode, W. Krolikowski, and Y. S. Kivshar, "Optical guiding of absorbing nanoclusters in air", *Opt. Express* **17**, 5743 (2009).

[92] A. S. Desyatnikov, V. G. Shvedov, A. V. Rode, W. Krolikowski, and Y. S. Kivshar, "Photophoretic manipulation of absorbing aerosol particles with vortex beams: theory versus experiment", *Opt. Express* **17**, 8201 (2009).

[93] C. N. Alexeyev, "Narrowband reflective generation of higher-order optical vortices in Bragg spun optical fibers", *Appl. Opt.* 433 (2013).

[94] D. Smith, C. Woods, A. Seddon, and H. Hoerber, "Photophoretic separation of single-walled carbon nanotubes: a novel approach to selective chiral sorting", *Phys. Chem. Chem. Phys.* 5221 (2014).

[95] S. B. Wang and C. T. Chan, "Lateral optical force on chiral particles near a surface", *Nat. Commun.* **5**, 3307 (2014).

[96] G. Tkachenko and E. Brasselet, "Helicity-dependent three-dimensional optical trapping of chiral microparticles", *Nat. Commun.* **5**, 4491 (2014).

[97] R. Beth, "Mechanical Detection and Measurement of the Angular Momentum of Light", *Phys. Rev.* **50**, 115 (1936).

[98] J. C. Jones, "A New Calculus for the Treatment of Optical Systems", *JOSA* 488 (1941).

Titre : Le piégeage et la manipulation optique de microsphères chiraux contrôlées par l'hélicité du photon

Résumé : Exploiter le degré de liberté angulaire de la lumière pour contrôler les forces optiques ouvre une nouvelle voie pour la manipulation optique de systèmes matériels. Dans ce contexte, notre travail porte sur l'interaction lumière-matière en présence de chiralité, qu'elle soit matérielle ou ondulatoire. Expérimentalement, nous avons utilisé des gouttes de cristaux liquides cholestériques interagissant avec un ou plusieurs champs lumineux polarisés circulairement et nous avons apporté une description quantitative de nos observations. Notre principal résultat correspond à la démonstration que la pression de radiation optique peut être contrôlée par l'hélicité du photon. Ce phénomène est ensuite utilisé, d'une part pour faire une démonstration de principe du tri de la chiralité matérielle via une approche optofluidique et d'autre part pour réaliser un piège optique tridimensionnel sensible à la chiralité de l'objet piégé.

Mots clés : Optomécanique – Optofluidique – Chiralité – Moment angulaire de la lumière – Cristaux liquides – Piégeage et manipulation optique

---

Title : Optical trapping and manipulation of chiral microspheres controlled by the photon helicity

Abstract : Exploiting the angular momentum degree of freedom of light to control the mechanical effects that result from light-matter exchanges of linear momentum is an intriguing challenge that may open new routes towards enhanced optical manipulation of material systems. In this context, our work addresses the interplay between the chirality of matter and the chirality of optical fields. Experimentally, this is done by using cholesteric liquid crystal droplets interacting with circularly polarized light and we provide with theoretical developments to quantitatively support our observations. Our main result is the demonstration of optical radiation force controlled by the photon helicity. This phenomenon is then used to demonstrate the optofluidic sorting of material chirality and the helicity-dependent three-dimensional optical trapping of chiral liquid crystal microspheres.

Keywords : Optomechanics – Optofluidics – Chirality – Optical angular momentum – Liquid crystals – Optical trapping and manipulation

---

Unité de recherche

Laboratoire Ondes et Matière d'Aquitaine (UMR 5798)

Université de Bordeaux, PAC Talence / Bât A4, 351 Cours de la Libération,
33405 Talence cédex, France